RC J0105+0501: A Radio Galaxy with Redshift $z \approx 3.5$

N. S. Soboleva[1], W. M. Goss[2], O. V. Verkhodanov[3]*, O. P. Zhelenkova[3],
A. V. Temirova[1], A. I. Kopylov[3], and Yu. N. Pariĭskiĭ[3]

[1] *St. Petersburg Branch, Special Astrophysical Observatory, Russian Academy of Sciences,*
Pulkovo, St. Petersburg, 196140 Russia
[2] *National Radio Astronomy Observatory, P. O. Box 0, Socorro, NM 87801, USA*
[3] *Special Astrophysical Observatory, Russian Academy of Sciences,*
Nizhniĭ Arkhyz, Stavropol kraĭ, 357147 Russia
Received March 13, 2000

Abstract—We study the radio galaxy RC J0105+0501 by using observations with RATAN-600, VLA, and 6-m Special Astrophysical Observatory telescope. The radio source has a structure resembling the FRII type and the spectral index $\alpha = 1.23$; it is identified with a faint galaxy of $22\overset{m}{.}8$ in R_c. The optical object is $1\overset{m}{.}5$ brighter in V than it is in B and has an extended structure, which we interpret as intense Lyα line emission with redshift $z \approx 3.5$ and a continuum depression in the adjacent short-wavelength region. Based on BVR_cI_c photometry, we also estimated the age of the stellar population of the radio galaxy. © *2000 MAIK "Nauka/Interperiodica".*

Key words: *distant radio galaxies*

INTRODUCTION

In recent years, the method of multicolor photometry has become the main one in selecting candidates for distant galaxies and, at very large redshifts, the only one. Selection by the spectral index is also used for radio galaxies. More than 300 galaxies with $z > 3$ have been detected to date; however, according to publications by early 2000, only 17 objects with intense radio emission (radio galaxies) were known among them. The first radio galaxy with $z > 3$ was discovered by Lilly (1988). The radio galaxy with a record redshift has $z = 5.19$ (Van Breugel *et al.* 1999). The interest in radio galaxies at large redshifts stems from the fact that they allow one to trace the evolution of a special population of giant stellar systems with massive black holes the hypotheses of whose formation are just being discussed.

By early 1999, we had implemented a technique for selecting candidates for distant galaxies by means of multicolor (BVR_cI_c) photometry by applying it to a sample of 50 radio galaxies with steep spectra from the RC catalog. We used the photometric data obtained with the 6-m Special Astrophysical Observatory telescope to estimate the "color" redshifts and ages of the parent galaxies. In this paper, we present the results of our observations and their interpretation for one of the most likely candidates for radio galaxies with $z > 3$, the radio source RC J0105+0501. Table 1 lists basic parameters for RC J0105+0501 and 105 objects with steep spectra

from our complete search list selected from the COLD catalog (Pariĭskiĭ *et al.* 1996, 2000). As we see from Table 1, by its basic parameters, RC J0105+0501 satisfies fairly well the criteria optimizing the detection of extremely distant radio galaxies.

RADIO DATA

The radio source RC J0105+0501, which was detected in the COLD survey (Pariĭskiĭ *et al.* 1991, 1992), belongs to a subsample of objects with ultrasteep radio spectra. Figure 1 shows the radio continuum spectrum of this object constructed by using the CATS database (Verkhodanov *et al.* 1997). Table 2 gives the flux densities and frequencies of the catalogs used to construct the spectrum, as well as the corresponding coordinates of the radio source. In this table, the "catalog" column lists the following surveys: Texas (TXS: Douglas *et al.* 1996), Northern VLA Sky Survey

Table 1. Parameters of radio sources with steep spectra from the RC catalog

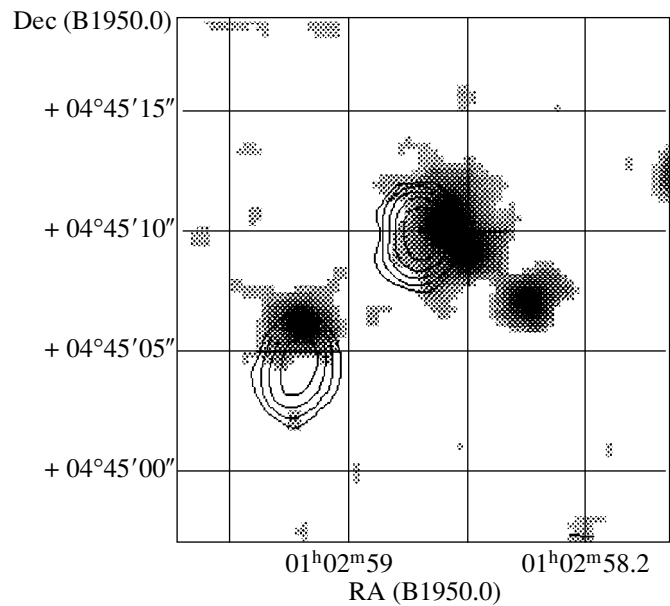| Parameter	0105+0501	Other objects of list
Flux density (3.9 GHz)	23 mJy	15–350 mJy
Maximum angular size	$7\overset{''}{.}6$	$\leq 0\overset{''}{.}7$–$120''$
Spectral index	1.23	0.9–1.5
R_c magnitude	$22\overset{''}{.}8$	18^m–$\geq 25^m$

* E-mail address for contacts: vo@sao.ru.
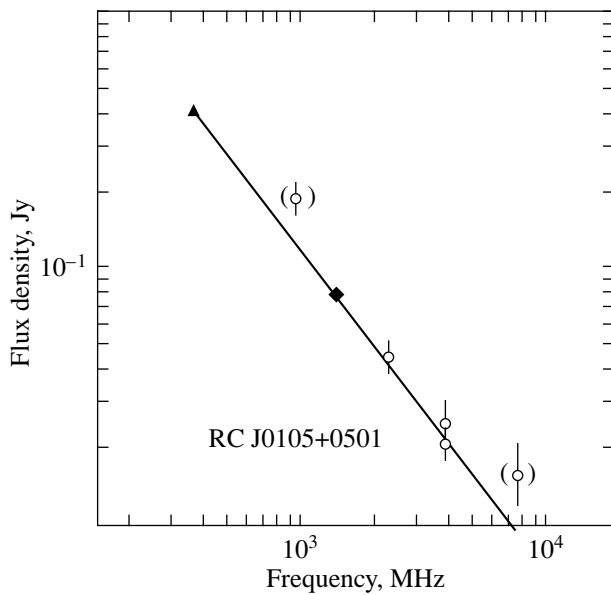
Fig. 1. The radio spectrum of RC J0105+0501 constructed from Texas, NVSS, and COLD survey data.

Fig. 2. The radio structure of RC J0105+0501 as inferred from VLA data at 1425 MHz. The isophotes were constructed from levels proportional to a factor of 2, starting from 1 mJy, and are superimposed on the optical *V*-band image obtained with the 6-m telescope.

(NVSS: Condon *et al.* 1998), and COLD (COLD: Pariĭskiĭ *et al.* 1992; COLD B: Bursov 1996).

To determine the spectral index, we used the least-squares method when fitting the radio spectrum. Each point of the spectrum was weighed proportionally to the relative measurement error $1/(\Delta S/S)^2$; for some points, we "roughened" the errors: if the relative error in the flux density was smaller than 10%, we assigned the weight to it as that for the 10% error. The weight of two points, at 7700 MHz and 960 MHz, which widely deviated from the straight line, was decreased by a factor of 10. Thus,

we obtained a linear fit to the radio spectrum and determined the spectral index, $= 1.23 (S_\nu \propto \nu^{-\alpha})$.

The radio structure of the source was studied with the VLA (Pariiskii *et al.* 1996). The object's isophotes at 1425 MHz (see Fig. 2) show a structure similar to the FRII type (Fanaroff and Riley 1974). The lobe angular separation (LAS) is $7.''6$. Table 3 gives the coordinates and flux densities of the components at 1425 MHz as inferred from VLA observations with a $1.''51 \times 1.''43$ beam.

Table 2. Data of various radio surveys for RC J0105+0501

RA(2000.0)	Dec(2000.0)	ν, MHz	*S*, mJy	Δ*S*, mJy	Catalog
$01^h\ 05^m\ 34.^s122\ 0.095$	$+05°\ 01''\ 10.22\ 0.61$	365	414	23	TXS
01 05 34.09	+05 01 09.2	960	187	30	ColdB
01 05 34.239 0.033	+05 01 10.94 0.59	1400	79.4	2.9	NVSS
01 05 34.09	+05 01 09.2	2300	45	7	ColdB
01 05 34.62	+05 01 19	3900	25	5.5	Cold
01 05 34.09	+05 01 09.2	3900	21	3	ColdB
01 05 34.09	+05 01 09.2	7700	16	5	ColdB

Table 3. Parameters of the components of the radio source RC J0105+0501 at 1425 MHz

RA(1950.0)	Dec(1950.0)	RA(2000.0)	Dec(2000.0)	Size	*S*, mJy
$01^h\ 02^m\ 58.^s786$	$+04°45''10.16$	$01^h05^m34.^s13$	$+05°01''13.2$	$1.''0$	50
01 02 59.13	+04 45 04.6	01 05 34.47	+05 01 07.6	1.3	29
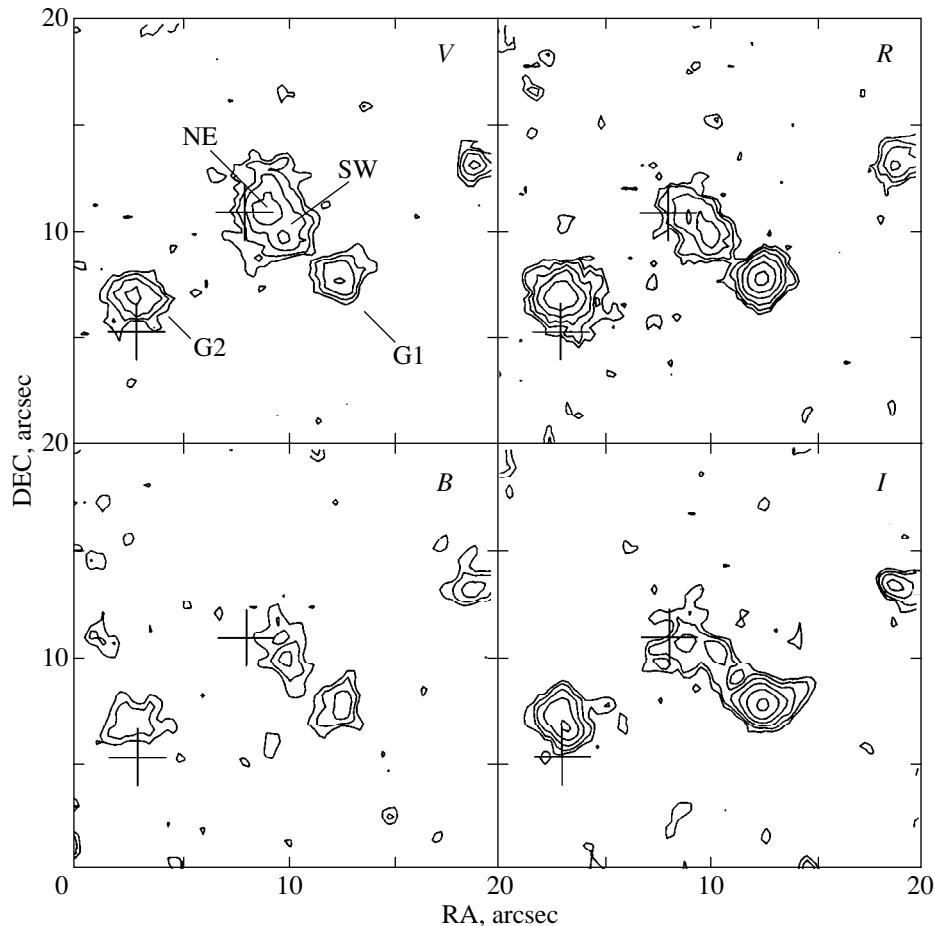
Fig. 3. Optical images of the radio galaxy RC J0105+0501 in four bands. On the *V*-band image, the southwestern (SW) and northeastern (NE) components of the optical source are marked; the nearby galaxies are denoted by G1 and G2 (see Table 4). The positions of the radio source's components are marked by crosses.

In principle, the spectrum of the object can be decomposed into components rather than fitted by a straight line. For example, the case is possible where one of the source's components (NE, Fig. 3) has a steep spectrum ($\alpha \simeq 1.5$) and the other (SW) has a flat spectrum ($\alpha \simeq 0.5$). In this case, the flux density at 7700 MHz is mainly determined by the flat component. However, by comparing the positions of the centroids derived with allowance for the measured flux densities of the two components at 1425 MHz and the expected flux densities at 365 MHz, we cannot confidently accept or reject the hypothesis of such a spectrum decomposition, because of the relatively large (~2″) position errors in the Texas survey. This situation can be clarified by measuring the components' flux densities, for example, at 4850 MHz.

OPTICAL DATA

The primary identification of the radio source was made by using two images obtained in December 1994 with a 400-s exposure in the R_c band (Kron–Cousins system) at a moderate seeing of 2″2 (FWHM). Two or even three galaxies detected near the components of the radio source could be considered as candidates for identification. To clarify the situation, we took *B, V,* and I_c images in December 1997 at FWHM = 2″0 (exposure times 500, 300+400, and 400 s), and, finally, we managed to obtain best quality images (FWHM = 1″4) in August 1998 (600, 400, 400 and 2 × 400 s in *B, V, R_c,* and I_c, respectively). The images were processed in the ESO-MIDAS system. For astrometric referencing of the optical images, we used stars nos. 188, 272, 277, and 403 from the USNO A2.0 catalog. The identification results are presented in Fig. 3, which shows a 20″ × 20″ area around the radio source position in each of the four bands (1998 images). The positions of the two components of the radio source are marked by crosses.

One of the candidates (central) exhibits the color properties and the complex structure changing from band to band that are typical of powerful distant radio galaxies. In the *V* band, this galaxy has the largest extent and is $1^m.5$ brighter than in the *B* band; for the objects of this class, this is virtually unambiguously interpreted as intense Lyα line emission and continuum

Table 4. Photometry for the radio galaxy RC J0105+0501 and neighboring objects

	Aperture	B	$B–V$	V	$V–R$	R	$R–I$	I
RCJ 0105+0501(SW+NE)	4″	24.1	1.6	22.5	–0.3	22.8	0.4	22.4
SW component	1.7	25.0	1.0	24.0	0.3	23.7	0.3	23.4
NE component	1.7	25.9	2.3	23.6	–0.3	23.9	0.5	23.4
Western galaxy (G1)	4	23.8	0.4	23.4	0.9	22.5	0.8	21.7
Eastern galaxy (G2)	4	24.1	0.9	23.2	0.8	22.4	0.7	21.7

depression in the neighboring short-wavelength region (see Figs. 3 and 4). The negative color index $V–R_c = -0.3$ and the small color index $R_c–I_c = 0.4$ are consistent with this interpretation of the data. The estimated redshift and its probable error are determined by the position of the sensitivity maximum and by the V half-width, respectively: $z = 3.5 \pm 0.3$.
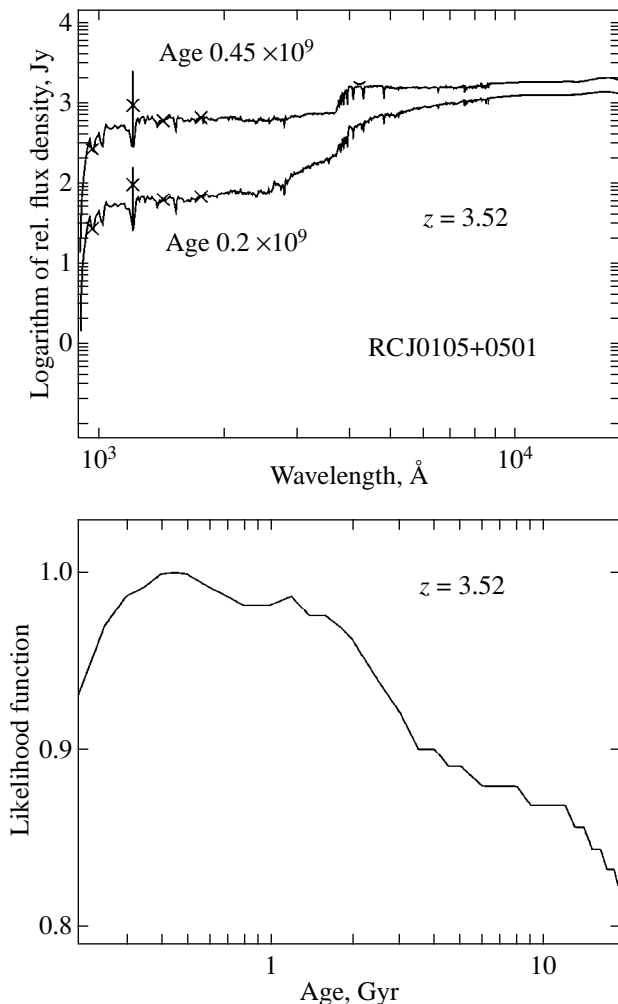
Fig. 4. In the upper panel, the photometric data are fitted by the spectral energy distributions of an elliptical galaxy with stellar-population ages of 0.45 and 1.2 Gyr in the presence of Lyα emission for the redshift $z = 3.52$. In the lower panel, a normalized univariate likelihood function is plotted versus age for the redshift $z = 3.52$.

We see that, assuming the identification to be correct, the radio galaxy is resolved into two components which are 1″.7 apart. Table 4 lists the measured magnitudes and colors of the objects (through a 1″.7 aperture for the components of the radio galaxy using the 1998 data alone, and through a 4″ aperture for the radio galaxy as a whole and for the other two galaxies using all data). The measurement errors are $\approx 0\overset{m}{.}1–0\overset{m}{.}2$.

The two neighboring galaxies (G1 and G2 in Fig. 3), which are brighter in R_c, are probably not associated with the radio galaxy, because the estimated color redshifts for them lie in the range from $z = 0.6$ to $z = 1.2$.

ESTIMATING THE AGE OF THE STELLAR POPULATION

Using the PEGASE library of evolutionary models for the spectral energy distributions of elliptical galaxies (Fioc and Rocca-Volmerange 1997), we estimated the age and redshift for the radio galaxy RC J0105+0501 on the basis of four-color photometry by the method described by Verkhodanov *et al.* (1999). In our calculations, we assumed the galaxy to be surrounded by gas, adding a δ-function corresponding to the Lyα emission line (1216 Å) to the model distribution; we also performed calculations without this line. The age of the parent galaxy in the presence of the emission line, which, in our case, allows an unambiguous estimation of the redshift ($z \approx 3.5$), is estimated to be 0.45 Gyr. In addition, the likelihood function has a local maximum corresponding to an age of 1.2 Gyr (Fig. 4). In the absence of Lyα emission, the redshift near the maximum of the likelihood function is estimated to be $z = 3.27$ for an age of 1.8 Gyr. It should be noted that, whereas the redshift estimate is fairly reliable, because the line falls within the observed band, the age estimate for the radio galaxy at $z > 3$ is rather rough, since, after all, the model calculations were made for elliptical galaxies, which had not yet formed by the observed time.

Whereas the redshift is determined reliably enough (Lyα falls within the V band), the age is less reliable. In any case, however, it is consistent even with the simple CDM model, for which the age of the Universe at $z = 3.5$ is ~1 Gyr. This confirms the conclusion by Pariĭskiĭ (1999) that the phenomenon of distant objects with the formal age in the simple CDM model exceeding the age of the Universe is observed only in a certain range of redshifts.

DISCUSSION

If we introduce parameter m_{lim} (Kopylov *et al.* 1995), which characterizes the limiting magnitude of the parent galaxy responsible for the emergence of a radio source with a given flux density, then its value for our radio source will be 23^m (Pariĭskiĭ 1996, 1998), consistent with our data. Curiously enough, the radio luminosity of this object is close to the optical luminosity at $z = 3.5$ (see the optical data above), suggesting that this relationship is universal for powerful radio galaxies and that there is no strong dust absorption for this object. This is also suggested by the absence of a steep slope in the short-wavelength part of the spectrum, as implied by four-color photometry (see Fig. 4).

As regards an optical identification of the radio galaxy, it should be noted that the double radio source can in principle be a projection effect (if one radio source is identified with a galaxy at $z \simeq 1$ and the other with a galaxy at $z \simeq 3.5$, as shown by the photometric estimates of their z). However, we consider this possibility to be unlikely, because the integrated radio spectrum is very steep and is most likely fitted by a single curve (see Fig. 1).

If at least one component of the radio source is closely identified with an adjacent galaxy in the image, then it is no longer correct to speak about an FRII-type structure for this object. However, we cannot rule out the possibility that the source core, which can be located between the two radio components, simply has not yet been detected either in the optical or in the radio band, and the radio source actually has an FRII structure, resembling the radio galaxy TN J1338–1942 with $z = 4.11$ (De Breuck *et al.* 1999).

Since only one (southwestern) component of the central optical object in Fig. 3 is clearly detected on the *B* image, we can also consider the possibility that it is an active nucleus of the radio galaxy. The second (northeastern) component can then be either a region of jet-triggered star formation or a gas cloud ionized by radiation from the active nucleus, or a combination of both. This possibility is indirectly supported by the conclusions of Van Breugel *et al.* (1998), who studied radio galaxies with $z > 3$ in the near infrared and found two scales with typical structures in them: formations with sizes of ~10 kpc surrounded by large-scale (~50–100 kpc) weak diffuse emission.

Without going into a detailed analysis, we note that alternative interpretations of the available data can be proposed to explain the nature of RC J0105+0501. The key question is where the active nucleus of the radio source is located. There is an obvious need for a more detailed study of this interesting object both at optical wavelengths (spectroscopically) and in the infrared and radio ranges to test various hypotheses about the physics of the processes in this stellar system, which is probably at an early stage of its formation and may belong to the first generation of massive elliptical galaxies.

REFERENCES

1. N. N. Bursov, Astron. Zh. **73**, 1 (1996)

2. J. J. Condon, W. D. Cotton, E. W. Greisen, *et al.*, Astron. J. **115**, 1693 (1998).

3. C. De Breuck, W. van Breugel, D. Minniti, *et al.*, Astron. Astrophys. (1999) (in press); astro-ph/9909178.

4. J. N. Douglas, F. N. Bash, F. A. Bozyan, *et al.*, Astron. J. **111**, 1945 (1996).

5. B. L. Fanaroff and J. M. Riley, Mon. Not. R. Astron. Soc. **167**, 31 (1974).

6. M. Fioc and B. Rocca-Volmerange, Astron. Astrophys. **326**, 950 (1997).

7. A. I. Kopylov, W. M. Goss, Yu. N. Pariĭskiĭ, *et al.*, Astron. Zh. **72**, 613 (1995) [Astron. Rep. **39**, 543 (1995)].

8. S. J. Lilly, Astrophys. J. **333**, 161 (1988).

9. Yu. N. Parijskij, N. N. Bursov, N. M. Lipovka, *et al.*, Astron. Astrophys., Suppl. Ser. **87**, 1 (1991).

10. Yu. N. Parijskij, N. N. Bursov, N. M. Lipovka, *et al.*, Astron. Astrophys., Suppl. Ser. **96**, 583 (1992).

11. Yu. N. Parijskij, W. M. Goss, A. I. Kopylov, *et al.*, Bull. SAO, No. 40, 5 (1996).

12. Yu. N. Pariĭskiĭ, W. M. Goss, A. I. Kopylov, *et al.*, Astron. Zh. **75**, 483 (1998) [Astron. Rep. **42**, 425 (1998)].

13. Yu. N. Parijskij, W. M. Goss, A. I. Kopylov, *et al.*, Astron. Astrophys. Trans. (2000) (in press); astro-ph/005240.

14. Yu. N. Parijskij, *The High-Redshift Radio Universe* (Kluwer Acad., Dordrecht, 1999).

15. W. van Breugel, S. A. Stanford, H. Spinrad, *et al.*, Astrophys. J. **502**, 614 (1998).

16. W. van Breugel, C. De Breuck, S. A. Stanford, *et al.*, Am. Astron. Soc. Meeting **194**, No. 110.07 (1999); astro-ph/9904272.

17. O. V. Verkhodanov, S. A. Trushkin, H. Andernach, and V. N. Chernenkov, *Astronomical Data Analysis Software and Systems VI*, Ed. by G. Hunt and H. E. Payne, Astron. Soc. Pac. Conf. Ser. **125**, 322 (1997).

18. O. V. Verkhodanov, A. I. Kopylov, Yu. N. Parijskij, *et al.*, Bull. SAO, No. 48, 41 (1999).

Translated by G. Rudnitskiĭ

Effects of Microlensing on Parameters of the Images Seen near the Critical Curves of Gravitational Lens Galaxies

A. A. Minakov[1]* and V. G. Vakulik[2]

[1] *Institute of Radioastronomy, National Academy of Sciences of Ukraine,*
Krasnoznamennaya ul. 4, Kharkov, 310002 Ukraine
[2] *Astronomical Observatory, Kharkov State University, Kharkov, Ukraine*

Abstract—We investigate the effect of microlensing on parameters of the images of distant sources seen near the critical curves of complex gravitational lenses, which are represented as a sum of compact structures—microlenses (stars, star-like or planet-like bodies) and diffusely distributed matter (dust and gas clouds etc.). The observation of merging, cross-shaped, annular, or arc-shaped source images is an indication that the images are close to the critical curves of gravitational lenses. Our analysis and numerical solution have allowed us to determine the structures of the critical curves and caustics formed by macro- and microlenses, as well as to estimate the characteristic perturbations introduced by microlenses at their various positions relative to the critical curve of a regular gravitational lens. We show that, the closer are the microlenses to the critical curve, the larger is the discrepancy between our results and those obtained previously with standard (linearized) allowance for the effect of a regular gravitational lens. © *2000 MAIK "Nauka/Interperiodica".*

INTRODUCTION

Uncorrelated light variations of the images of a distant source that are split in the gravitational field of a galaxy are a characteristic feature of microlensing. This effect clearly shows up, for example, in long-term observations of the gravitational lens (GL) Q2237+0305, in which four quasar images are detected near the galactic center within a circle of ≈1″ radius. The uncorrelated light variations of these images indicate that the effect of microlenses (stars, star-like or planet-like bodies) rather than intrinsic variations in the source of quasar radiation are observed here. Considering the difficulties of a theoretical analysis, microlensing is mainly investigated by numerical methods. The standard procedure of numerical simulations is as follows. The effect of all microlenses randomly located inside the galaxy is described in two ways. The microlenses closest to the line of sight (close to the observed source image) are taken into account by specifying their true refraction angles. The number of such microlenses generally does not exceed several hundred (Paczynski 1986; Seitz and Schneider 1994; Blandford and Narayan 1992). The remaining microlenses far from the line of sight and the matter diffusely distributed in the galaxy are specified by introducing a refraction angle averaged over interstellar space. The problem can

be further simplified by linearizing the average refraction angle of the macrolens galaxy near the selected source image (Seitz and Schneider 1994; Blandford and Narayan 1992; Schneider *et al.* 1992; Zakharov and Sazhin 1998). Unfortunately, a numerical analysis does not allow the dependence of observable characteristics on particular parameters of the problem to be traced. It is therefore desirable to obtain analytic estimates for the effect under consideration. Of particular interest is the case where the source macroimages and the perturbing microlenses lie near the critical curves of GL galaxies, when the effect of microlenses on the focusing increases significantly. The observation of merging, cross-shaped, annular, or arc-shaped source images is an indication that the macroimages are close to the GL critical curves.

This work aims at analyzing the structures of the critical curves and caustics for a complex GL when the microlenses are located near its critical curve. In our study, we use a model for GL Q2237+0305 as an example.

A GRAVITATIONAL LENS MODEL

A complex lens galaxy can be represented as a sum of the following two components: one is associated with the masses concentrated in compact structures (stars, star-like or planet-like bodies), and the other is associated with the diffusely distributed matter (dust and gas clouds etc.). We specify the compact structures, which are below called microlenses, as point masses

---

*E-mail address for contacts: minakov@ira.kharkov.ua

M_i. The total number of microlenses N in the galaxy is fairly large. For example, $N \sim 10^{11}$–10^{12} for a spiral galaxy similar to GL Q2237+0305. We first analyze microlensing by using a single microlens as an example and then generalize the results to many microlenses. Let us introduce a Cartesian system of XYZ coordinates whose origin coincides with the galactic center of mass and whose Z axis passes through the point of observation (see Fig. 1). Denote the distances from observer P and point source S to the GL by Z_p and Z_s, respectively. Since Z_p and Z_s are much larger than the sizes of the region where the rays of light are refracted, the GL can be approximated by an infinitely thin phase screen (Bliokh and Minakov 1989) that coincides with the $Z = 0$ plane. Choosing a single microlens located in the lens plane at point $\mathbf{p} = \mathbf{p}_m$ from the entire set of N microlenses, we write the formula for the ray deflection angle in the lens plane ($Z = 0$):

$$\mathbf{\Theta}(\mathbf{p}) = -2r_{gm}\frac{\mathbf{p} - \mathbf{p}_m}{(\mathbf{p} - \mathbf{p}_m)^2}$$

$$-\sum_{i=1}^{N-1} 2r_{gi}\frac{\mathbf{p} - \mathbf{p}_i}{(\mathbf{p} - \mathbf{p}_i)^2} + \mathbf{\Theta}_{\text{dif}}(\mathbf{p}). \quad (1)$$

Here, $\mathbf{p} = (x, y)$ is the ray impact parameter measured in the GL plane; $\mathbf{p}_i$ and $r_{gi} = 2GM_i/c^2$ are, respectively, the coordinate and gravitational radius of the ith microlens (G is the gravitational constant, c is the speed of light); $\mathbf{\Theta}_{\text{dif}}(\mathbf{p})$ is the component of the refraction angle associated with the diffusely distributed matter. Assuming the multivariate distribution function of the random variables r_{gi} and $\mathbf{p}_i$ to be known, we can derive the average refraction angle $\langle\mathbf{\Theta}(\mathbf{p})\rangle$ and its rms deviation $\langle(\delta\mathbf{\Theta})^2\rangle$ (see, e.g., Bliokh and Minakov 1989; Schneider *et al.* 1992). A gravitational lens with the average deflection angle $\langle\mathbf{\Theta}(\mathbf{p})\rangle$ is below called a regular GL or a macrolens. This approximation corresponds to a GL in which the mass density of stars and diffuse matter is "spread" over fairly large (interstellar) regions. Let us consider a small region near microlens m whose size, on the one hand, is small compared to the characteristic interstellar distance a in this region and, on the other, are larger than (or comparable to) the characteristic size of the Einstein ring $l_m = \sqrt{2r_{gm}Z_pZ_s/(Z_p + Z_s)}$ for the microlens in question ($l_m < |\mathbf{p} - \mathbf{p}_m| < a$). Given that the rms deviation of the angle is small (Bliokh and Minakov 1989; Schneider *et al.* 1992), it can be readily shown that the second and third terms in formula (1) essentially match the average deflection angle $\langle\mathbf{\Theta}(\mathbf{p})\rangle$ within the region under consideration. There are several ways of specifying a model for the mass distribution in GL Q2237+0305 (see, e.g., Kent and Falco 1988; Minakov and Shalyapin 1991; Wambsganss and Paczynski 1994; Schmidt *et al.* 1998). Based on observational data, we choose a model that is simple enough, but in such a way that it could form an observable cross-shaped image structure. We represent the regular
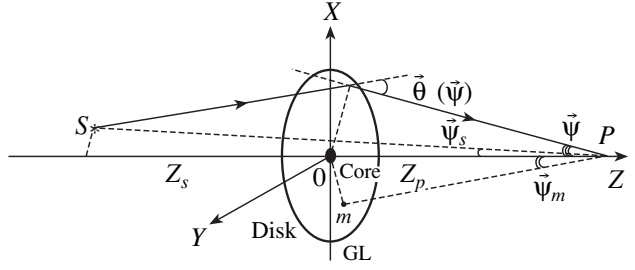
Fig. 1. The relative positions of radiation source S, macrolens galaxy GL, microlens m, and observer P.

component of the macrolens refraction angle $\langle\mathbf{\Theta}(\mathbf{p})\rangle$ as a sum of two components, one associated with the massive disk $\mathbf{\Theta}_d(\mathbf{p})$ and the other associated with the compact core $\mathbf{\Theta}_c(\mathbf{p})$: $\langle\mathbf{\Theta}(\mathbf{p})\rangle = \mathbf{\Theta}_d(\mathbf{p}) + \mathbf{\Theta}_c(\mathbf{p})$. In order to simplify the analysis, we assume the core and the extended disk to have spherical and elliptical symmetries, respectively, whose centers coincide. The OX and OY axes are directed along the principal symmetry axes of the disk component. The effect of gravitational focusing is described by a lens equation, which in angular variables $\mathbf{\psi} = \mathbf{p}/Z_p$ takes the form

$$\mathbf{\psi}_s = \mathbf{\psi} + \frac{\tilde{Z}}{Z_p}[\mathbf{\Theta}_c(\mathbf{\psi}) + \mathbf{\Theta}_d(\mathbf{\psi})] - \Psi_m^2\frac{\mathbf{\psi} - \mathbf{\psi}_m}{(\mathbf{\psi} - \mathbf{\psi}_m)^2}. \quad (2)$$

Here, $\mathbf{\psi}_s$ is the true angular position of the point source of radiation; $\mathbf{\psi}_m = \mathbf{p}_m/Z_p$ is the angular coordinate, and $\Psi_m = l_m/Z_p$ is the angular radius of the microlens Einstein ring; and $\tilde{Z} = Z_pZ_s/(Z_p + Z_s)$ is the reduced distance. Since the scale lengths of variations in the surface mass density of the disk component of GL Q2237+0305 considerably exceed the sizes of the region ($\approx 2''$) where the four quasar images are observed, the following approximate representation of $\mathbf{\Theta}_d(\mathbf{p})$ near the galactic center can be used: $\mathbf{\Theta}_d(\mathbf{\psi}) \approx \mathbf{\Theta}_d(0) + (\mathbf{\psi}\nabla)\mathbf{\Theta}_d(0)$. Assuming the characteristic sizes of the galactic compact core to be smaller than the sizes of the region where the four images are observed, we approximate the spherical component by a point mass equal to the galactic-core mass M_c. Given the above simplifications and assumptions and that $\mathbf{\Theta}_d(0) = 0$ for the disk model chosen, the lens equation (2) can be transformed to the following form (Minakov and Shalyapin 1991):

$$\mathbf{\psi}_s = \mathbf{\psi}\left(1 - \frac{\tilde{Z}}{Z_F^d} - \frac{\Psi_c^2}{\psi^2}\right) + \alpha_d\psi_x\mathbf{e}_x - \alpha_d\psi_y\mathbf{e}_y$$

$$- \Psi_m^2\frac{\mathbf{\psi} - \mathbf{\psi}_m}{(\mathbf{\psi} - \mathbf{\psi}_m)^2}. \quad (3)$$

Here, $\mathbf{e}_x$ and $\mathbf{e}_y$ are the unit vectors of the rectangular coordinate system, and

$$\frac{1}{Z_F^d} = -\frac{1}{2Z_p}\left[\frac{\partial\Theta_{dx}(0)}{\partial\psi_x} + \frac{\partial\Theta_{dy}(0)}{\partial\psi_y}\right],$$

$$\alpha_d = \frac{\tilde{Z}}{2Z_p}\left[\frac{\partial\Theta_{dx}(0)}{\partial\psi_x} - \frac{\partial\Theta_{dy}(0)}{\partial\psi_y}\right]. \qquad (4)$$

It is easy to show that Z_F^d with the dimensions of length is related to the observed surface mass density at the disk center $\sigma_d(0)$ by $Z_F^d = c^2/4\pi G\sigma_d(0)$ and that the dimensionless parameter α_d determines the asymmetry introduced by the disk component near the galactic center. The quantity $\Psi_c = \sqrt{2R_c\tilde{Z}}/Z_p$, where $R_c = 2GM_c/c^2$ is the gravitational radius of the galactic core, corresponds to the angular radius of the Einstein ring of the core. It follows from Eq. (3) that, in the absence of a microlens ($\Psi_m = 0$) and asymmetry introduced by the disk ($\alpha_d = 0$), the central source of radiation ($\boldsymbol{\psi}_s = 0$) would be observed near the galactic center as a luminous ring of radius $\Psi_l = \Psi_c/\sqrt{1 - \tilde{Z}/Z_F^d} > \Psi_c$. Given this circumstance, the lens equation (3) can be simplified by introducing angles $\mathbf{v} = \boldsymbol{\psi}/\Psi_l$ and $\mathbf{v}_m = \boldsymbol{\psi}_m/\Psi_l$ normalized to Ψ_l, as well as the effective dimensionless displacement $\mathbf{v}_s = \boldsymbol{\psi}_s/\Psi_l(1 - \tilde{Z}/Z_F^d)$ of the source and the effective asymmetry coefficient $\alpha = \alpha_d/(1 - \tilde{Z}/Z_F^d)$. In the new normalized variables, we have

$$\mathbf{v}_s = \mathbf{v}\left(1 - \frac{1}{v^2}\right) + \alpha v_x\mathbf{e}_x - \alpha v_y\mathbf{e}_y - \Gamma\frac{\mathbf{v} - \mathbf{v}_m}{(\mathbf{v} - \mathbf{v}_m)^2}, \quad (5)$$

where $\Gamma = \Psi_m^2/\Psi_c^2 = r_{gm}/R_c \ll 1$ is a small parameter, the ratio of the stellar mass to the galactic-core mass. For the subsequent analysis and numerical estimates, we assume that the inequality $\Gamma \ll \alpha \ll 1$ holds. For example, Γ for Q2237+0305 can be chosen to be $\Gamma \approx 10^{-9}$–10^{-10}. The ring angular size Ψ_l and α and $\tilde{Z}/Z_F^d$ can be roughly estimated from models (Minakov and Shalyapin 1991) as $\Psi_l \approx 0''.9$; $\alpha \approx 0.16$, and $\tilde{Z}/Z_F^d \approx 0.3$.

The equation for the GL critical curve $\mathbf{v} = \mathbf{v}_{cr}$ is derived from the condition of the Jacobian of transformation from the variables v_s to the variables v being equal to zero (Bliokh and Minakov 1989):

$$q^{-1} = \left|\frac{\partial(v_{sx}, v_{sy})}{\partial(v_x, v_y)}\right| = 0. \qquad (6)$$

In polar coordinates $\mathbf{v} = (v, \varphi)$ and $\mathbf{v}_m = (v_m, \varphi_m)$, where the azimuthal angles φ and φ_m are measured from the OX axis, this equation can be reduced using (5) to

$$q^{-1}v^4 f_{m1}^2 = F_M f_{m1}^2 - 2\Gamma v^2(f_{m2} + \alpha v^2 f_{m3})$$
$$- \Gamma^2 v^4 = 0. \qquad (7)$$

Here, we introduce the following notation:

$$F_M(v, \varphi) = (1 - \alpha^2)v^4 - 2\alpha v^2\cos 2\varphi - 1,$$
$$f_{m1} = v^2 + v_m^2 - 2vv_m\cos(\varphi - \varphi_m),$$
$$f_{m2} = v^2 + v_m^2\cos(2\varphi - 2\varphi_m) - 2vv_m\cos(\varphi - \varphi_m),$$
$$f_{m3} = v^2\cos 2\varphi + v_m^2\cos 2\varphi_m - 2vv_m\cos(\varphi + \varphi_m). \qquad (8)$$

Substituting the solution $\mathbf{v} = \mathbf{v}_{cr}(\varphi)$ found from Eq. (7) in (5) yields the equation for the caustic shape in the source position plane

$$\mathbf{v}_{cs} = \mathbf{v}_{cr}\left(1 - \frac{1}{v_{cr}^2}\right) + \alpha v_{crx}\mathbf{e}_x - \alpha v_{cry}\mathbf{e}_y$$
$$- \Gamma\frac{\mathbf{v}_{cr} - \mathbf{v}_m}{(\mathbf{v}_{cr} - \mathbf{v}_m)^2}. \qquad (9)$$

We begin to analyze the set of equations (7) and (9) with the case where there is no microlens and subsequently determine how the characteristics of a regular GL are deformed by introducing a single microlens.

FOCUSING PROPERTIES OF A REGULAR GL

Setting $\Gamma = 0$ in (7), we arrive at the equation $F_M(v, \varphi) = (1 - \alpha^2)v^4 - 2\alpha v^2\cos 2\varphi - 1 = 0$, whose real solution is

$$v_{cr}^M(\varphi) = \left\{\frac{\alpha\cos 2\varphi + \sqrt{1 - \alpha^2\sin^2 2\varphi}}{1 - \alpha^2}\right\}^{1/2} \qquad (10)$$

and determines the critical curve of a regular GL. In the linear (in small parameter α) approximation, we have
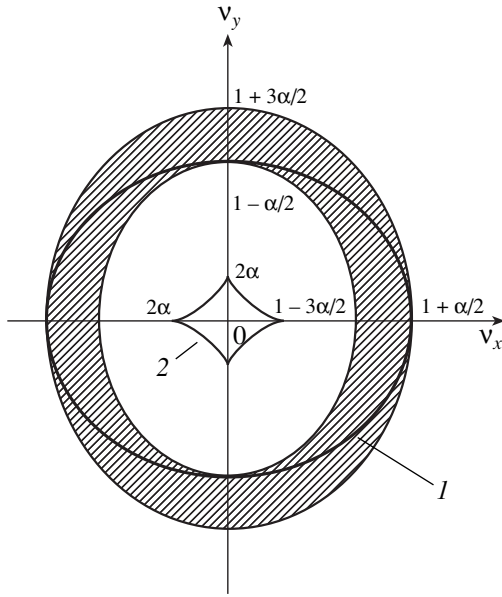
$$v_{cr}^M(\varphi) \approx 1 + \frac{\alpha}{2}\cos 2\varphi. \qquad (11)$$

Substituting (11) in (9) yields an approximate equation for the caustic of a regular GL in the source position plane:

$$v_{csx}^M(\varphi) = 2\alpha\cos^3\varphi, \quad v_{csy}^M(\varphi) = -2\alpha\sin^3\varphi. \quad (12)$$

We see that the model of a regular GL under consideration forms a critical curve in the lens plane in the shape of an oval with a mean radius approximately equal to unity ($v_{cr}^M \approx 1$), while the corre-

Fig. 2. The structure of critical curve *1* and caustic *2* for the model of a regular GL consisting of a compact core and an extended disk. The region of impact parameters for the microlenses whose caustics fall within the curvilinear diamond of the macrocaustic is hatched.

sponding caustic in the source position plane has the shape of a curvilinear diamond (astroid) with a characteristic size $\left| v_{cs}^{M} \right| \approx 2\alpha$ (see Fig. 2). It is easy to show that, when projecting point source *S* into the curvilinear diamond (12), we will observe its four (cross-shaped) images, two of which lie outside and the other two inside the critical curve (10) in the lens plane (see, e.g., Minakov and Shalyapin 1991). Since α is small, the images are located in the immediate vicinity of the critical curve (10).

ALLOWANCE FOR THE EFFECT OF MICROLENSES

For the specified α and Γ and the microlens angular position v_m, we numerically solved Eq. (7) by using a fairly simple method. The problem of finding the real roots of (7) can be replaced by a different, simpler problem. Thus, for example, denoting $\Phi(v, \varphi) = F_M f_{m1}^2 - 2\Gamma v^2 (f_{m2} + \alpha v^2 f_{m3}) - \Gamma^2 v^4$, the domains of positive ($\Phi > 0$) and negative ($\Phi < 0$) definiteness of $\Phi(v, \varphi)$ can be easily determined numerically. Assuming $\Phi(v, \varphi)$ to have no discontinuities in the range of v and φ under consideration, the problem of finding the roots of the equation $\Phi(v, \varphi) = 0$ reduces to determining the boundary between the domains of positive and negative definiteness of $\Phi(v, \varphi)$. Our numerical simulations show that the behavior of the critical curves and the corresponding caustics for a complex GL depends not only on the microlens distance to the critical curve of a regular GL but also on the sector in which the microlens moves. As an example, Fig. 3 shows the critical curves and the caustics for various microlens positions (outside, inside, and exactly on the critical curve of a regular GL). We considered two cases where the microlens moved along the *OX* and *OY* axes. To present the overall pattern of behavior of the macro- and microcurves in the same figure, Γ was chosen to be large enough, $\Gamma = 0.001$. Below, we also provide the curves for $\Gamma = 10^{-9}$.

When the microlens lies outside the critical curve of a regular GL (Fig. 3a), the solution of Eq. (7) can be represented as two closed lines: one is a slightly deformed macrolens critical curve, and the other is formed around the microlens. A similar breakup of the critical curve of a complex GL into a set of macro- and microcurves is also observed when the microlens lies inside the critical curve of a regular GL (Fig. 3b). However, by contrast to the case of Fig. 3a, the critical curve near the microlens has the shape of not one deformed
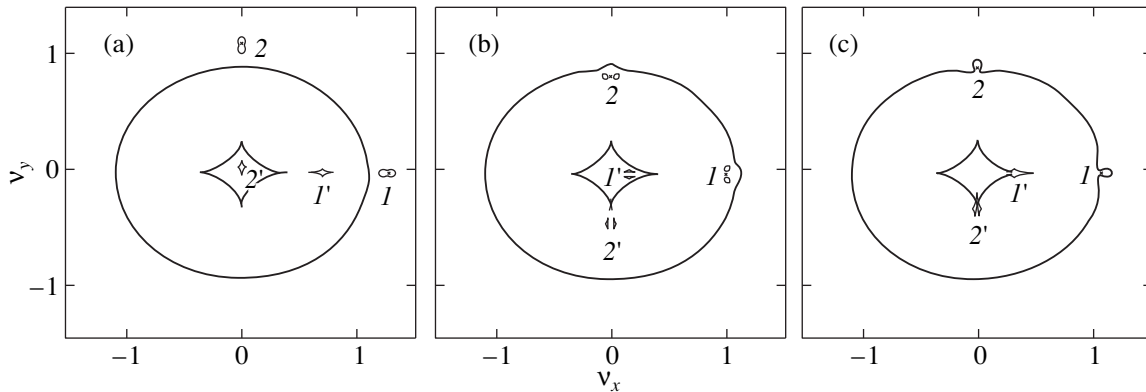
Fig. 3. The critical curves and caustics formed by a complex gravitational lens when the microlens lies (a) outside, (b) inside, and (c) exactly on the critical curve of a macrolens galaxy. The designations *1–1'* and *2–2'* correspond to the critical curve and caustic of the microlens on the OX and *OY* axes, respectively. The microlens position is marked by a cross; the calculations were performed for $\Gamma = 10^{-3}$.
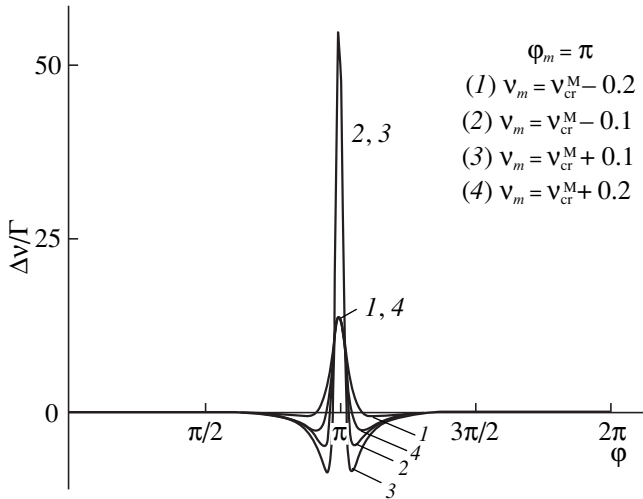
Fig. 4. The deformation of the macrolens critical curve produced by the microlens at its various distances from the critical curve of a regular GL.

oval (Einstein ring) but two ovals on both sides of the microlens. The most interesting case where the microlens falls directly on the macrolens critical curve is shown in Fig. 3c. For this situation, the macro- and microlens critical curves merge into a single complex continuous line.

Figure 3 also shows the shapes of the caustics emerging in the source position plane. When the microlens moves along the *OX* axis outside the critical curve (10), the caustic of a complex lens breaks up into two: one corresponds to a slightly deformed macrolens caustic, and the other, in the shape of a curvilinear diamond, corresponds to the microcaustic (Fig. 3a). As the microlens recedes from the critical curve of a regular GL, the microcaustic breaks away from the macrocaustic "beak," and, while moving outside the macrocaustic, gradually approaches the point where the microlens is located. A different pattern is observed when the microlens moves along the *OY* axis. In this case, as the microlens recedes from the critical curve of a regular GL, the microcaustic breaks away from the opposite beak of the macrocaustic, moves for some time inside it toward the nearest beak, goes outside the macrocaustic, and gradually catches up with the microlens. A set of caustics is also observed when projecting the microlens into the critical curve of a regular GL (Fig. 3b). One of them corresponds to the slightly deformed caustic curve of a regular GL, and the second corresponds to the microcaustic, which, by contrast to Fig. 3a, breaks up into two corresponding to the double structure of the critical curve. When the microlens moves along the *OX* axis and recedes from the critical curve of a regular GL, the double microcaustic breaks away from the nearest macrocaustic beak and moves for some time inside the

caustic of a regular GL toward the opposite beak. If, alternatively, the microlens moves along the *OY* axis, then the double microcaustic goes from the opposite beak of the macrocaustic outside it. When the microlens falls exactly on the critical curve of a regular GL (Fig. 3c), the macro- and microcaustics form a single, continuous polygonal line.

A numerical analysis clearly reveals a complex deformation of the critical and caustic curves. However, in order to quantitatively estimate the expected effects, it is desirable to have some analytic results as well, which will make it possible to keep track of the dependence of the emerging effects on particular model parameters. The main problem of an analytic study is to find the real roots of Eq. (7) for given α and Γ and microlens position ν_m. Since Γ is very small, the sought-for roots of Eq. (7) for the specified microlens displacement ν_m lie near the ν values for which the functions F_M and f_{mi} ($i = 1, 2, 3$) are approximately equal to zero. As was shown in the preceding section, the condition $F_M(\nu, \varphi) \approx 0$ can be satisfied at ν lying not far from the critical curve of a regular GL. On the other hand, according to (8), all functions f_{mi} ($i = 1, 2, 3$) simultaneously become zero at point $\nu = \nu_m$. Therefore, the condition $f_{mi}(\nu, \varphi) \approx 0$ can be satisfied if we consider displacements ν lying in the immediate vicinity of the point $\nu = \nu_m$.

If the microlens is located at some distance from ν_{cr}^M ($\nu_m \neq \nu_{cr}^M$), the problem of finding the roots of Eq. (7) breaks down into two simpler problems.

(i) The first solution is related to ν near ν_{cr}^M. Representing $\nu_{cr}(\varphi) = \nu_{cr}^M(\varphi) + \Delta\nu(\varphi)$, where $|\Delta\nu| \ll \nu_{cr}^M$, we obtain in the linear (in $\Delta\nu \sim \Gamma$) approximation

$$\Delta\nu(\varphi) \approx \Gamma \frac{f_{m2}[\nu_{cr}^M(\varphi), \varphi]}{2f_{m1}^2[\nu_{cr}^M(\varphi), \varphi]} \nu_{cr}^M(\varphi). \qquad (13)$$

Figure 4 shows normalized dependences of $\Delta\nu/\Gamma$ for various microlens distances from the critical curve of a regular GL. We see that the macrolens critical curve is deformed mainly in a small region toward the microlens. These deformations are proportional to Γ; they are the larger, the closer the microlens approaches the critical curve of a regular GL.

(ii) The second solution is related to the ν region close to the point where the microlens itself is located ($\nu = \nu_m$). In this case, the structure of the critical curve can be analyzed by setting $\nu_{cr} = \nu_m + \Delta\nu$ and $\varphi = \varphi_m +$
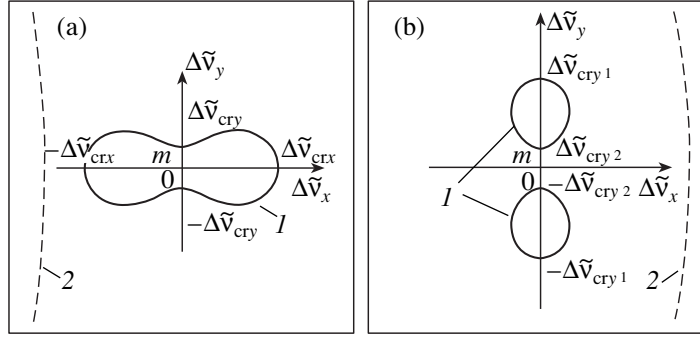
Fig. 5. The characteristic structures of critical curves *1* formed near microlens *m* when it is located (a) outside and (b) inside critical curve *2* of a regular GL.

$\Delta\varphi$, where $|\Delta\nu| \ll \nu_m$ and $|\Delta\varphi| \ll 1$, and by replacing the functions in Eq. (7) by their approximate values:

$$F_M(\nu, \varphi) \approx F_M(\nu_m, \varphi_m),$$

$$f_{m1}(\nu, \varphi) \approx \Delta\nu^2 + \nu_m^2 \Delta\varphi^2,$$

$$f_{m2}(\nu, \varphi) \approx \Delta\nu^2 - \nu_m^2 \Delta\varphi^2, \tag{14}$$

$$f_{m3}(\nu, \varphi) \approx (\Delta\nu^2 - \nu_m^2 \Delta\varphi^2)\cos 2\varphi_m$$
$$- 2\nu_m \Delta\nu \Delta\varphi \sin 2\varphi_m.$$

Introducing normalized local Cartesian coordinates $\Delta\tilde{\nu}_x = \Delta\nu/\sqrt{\Gamma}$ and $\Delta\tilde{\nu}_y = \nu_m \Delta\varphi/\sqrt{\Gamma}$. We derived the following simplified equation instead of (7):

$$F_M(\nu_m, \varphi_m)(\Delta\tilde{\nu}_y^2 + \Delta\tilde{\nu}_x^2)^2 - 2\nu_m^2(\Delta\tilde{\nu}_x^2 - \Delta\tilde{\nu}_y^2)$$
$$- 2\alpha\nu_m^4[(\Delta\tilde{\nu}_x^2 - \Delta\tilde{\nu}_y^2)\cos 2\varphi_m - 2\Delta\tilde{\nu}_y\Delta\tilde{\nu}_x \sin 2\varphi_m]$$
$$- \nu_m^4 = 0. \tag{15}$$

This equation describes the fine structure of the critical curve near the microlens. In addition, the numerical solution of (15) is in good agreement with that previously obtained for the strict equation (7); it also allows an exact analytic solution to be obtained. For example, (15) can be reduced by straightforward transformations to a simple biquadratic equation. However, we will not write out the solution of the latter but give only qualitative reasoning and estimate the characteristic sizes of the critical curve for $\varphi_m = 0$ and $\varphi_m = \pi/2$.

When the microlens moves along the *OX* axis ($\varphi_m = 0$) outside the critical curve of a regular GL ($\nu_m > \nu_{cr}^M = 1/\sqrt{1-\alpha}$), a single closed line is observed near the microlens. It has the shape of a deformed oval (see Fig. 5a) whose center roughly coincides with the microlens position ($\Delta\tilde{\nu}_y = 0$, $\Delta\tilde{\nu}_x = 0$). The coordi-

nates of the points of intersection of the critical curve with the ($\Delta\tilde{\nu}_y$, $\Delta\tilde{\nu}_x$) symmetry axes are, respectively,

$$\Delta\tilde{\nu}_{crx} = \pm\frac{\nu_m}{\sqrt{\nu_m^2(1-\alpha)-1}},$$

$$\Delta\tilde{\nu}_{cry} = \pm\frac{\nu_m}{\sqrt{\nu_m^2(1+\alpha)+1}}. \tag{16}$$

When the microlens moves inside the critical curve of a regular GL ($\nu_m < \nu_{cr}^M = 1/\sqrt{1-\alpha}$), the solution obtained from (15) differs from that described above. In this case, the critical curve has the shape of two closed ovals whose centers lie on both sides of the coordinate origin ($\Delta\tilde{\nu}_y = 0$, $\Delta\tilde{\nu}_x = 0$) along the $\Delta\tilde{\nu}_y$ axis (see Fig. 5b). The coordinates of the points of intersection of the critical curve with the $\Delta\tilde{\nu}_y$ axis are

$$\Delta\tilde{\nu}_{cry1} = \pm\frac{\nu_m}{\sqrt{1-\nu_m^2(1-\alpha)}},$$

$$\Delta\tilde{\nu}_{cry2} = \pm\frac{\nu_m}{\sqrt{1+\nu_m^2(1+\alpha)}}. \tag{17}$$

When the microlens is far from ν_{cr}^M, formulas (16) and (17) can be simplified significantly. For example, we obtain $\Delta\tilde{\nu}_{cry} \approx \pm1$ and $\Delta\tilde{\nu}_{crx} \approx \pm1$ for displacements $\nu_m \gg \nu_{cr}^M$, which corresponds to the values for an isolated microlens. At $\nu_m \ll \nu_{cr}^M$, the mean diameter of the two ovals is approximately equal to $|\Delta\nu_{cry1}| - |\Delta\nu_{cry2}| \approx \nu_m^3$, while their centers lie along the $\Delta\tilde{\nu}_y$ axis at points $\Delta\tilde{\nu}_{cry} \approx \pm\nu_m$. We see that, as the microlens approaches the center of the galactic core, the two critical curves come closer together, with their linear sizes simultaneously decreasing.

Let us now investigate the structure of the caustics emerging in the source position plane under the effect of a microlens. When the microlens is located at some distance from the critical curve of a regular GL ($v_m \neq v_{cr}^M$), we break down the problem of analyzing the emerging caustic curves into two simpler problems, by analogy with the preceding section.

(i) The microlens causes the macrocaustic to be deformed, which follows from changes in the critical curve of a regular GL (13). The emerging macrocaustic deformation can be estimated by substituting (13) in Eq. (9). Given that the addition $\Delta v(\varphi)$ is small ($|\Delta v| \ll v_{cr}^M$), the sought-for solution can be represented as $v_{csx} = v_{csx}^M + \Delta v_{csx}$ and $v_{csy} = v_{csy}^M + \Delta v_{csy}$, where $v_{csx,y}^M$ correspond to the previously found values of (12), while the small additions $\Delta v_{csx,y}$ ($|\Delta v_{csx,y}| \ll |v_{csx,y}^M|$) are

$$\Delta v_{csx}(\varphi) \approx \cos\varphi \left(1 + \frac{1}{v_{cr}^{M^2}} + \alpha \right) \Delta v$$

$$- \Gamma \frac{v_{cr}^M \cos\varphi - v_m \cos\varphi_m}{[v_{cr}^{M^2} + v_m^2 - 2v_{cr}^M v_m \cos(\varphi - \varphi_m)]},$$

$$\Delta v_{csy}(\varphi) \approx \sin\varphi \left(1 + \frac{1}{v_{cr}^{M^2}} - \alpha \right) \Delta v$$

$$\tag{18}$$

$$- \Gamma \frac{v_{cr}^M \sin\varphi - v_m \sin\varphi_m}{[v_{cr}^{M^2} + v_m^2 - 2v_{cr}^M v_m \cos(\varphi - \varphi_m)]}.$$

(ii) The second, more complex problem involves determining the structure of the caustics that correspond to the critical curves formed near the microlenses (see Figs. 5a and 5b). When the microlens moves along the *OX* axis ($\varphi_m = 0$) outside the critical curve of a regular GL ($v_m > 1/\sqrt{1 - \alpha}$), the microcaustic is grouped near the *OX* axis. Its shape and position can be roughly determined by linearizing Eq. (9). Thus, given the representation $v_{cr} = v_m + \Delta v$ and $\varphi = \varphi_m + \Delta\varphi$, we obtain for $\varphi_m = 0$

$$v_{csx} \approx \cos\Delta\varphi \left(v_m - \frac{1}{v_m} + \alpha v_m \right)$$

$$+ \cos\Delta\varphi \left(1 + \frac{1}{v_m^2} + \alpha \right) \Delta v$$

$$- \Gamma \frac{v_m(\cos\Delta\varphi - 1) + \Delta v \cos\Delta\varphi}{2v_m(v_m + \Delta v)(1 - \cos\Delta\varphi) + \Delta v^2},$$

$$\tag{19}$$

$$v_{csy} \approx \sin\Delta\varphi \left(v_m - \frac{1}{v_m} - \alpha v_m \right)$$

$$+ \sin\Delta\varphi \left(1 + \frac{1}{v_m^2} - \alpha \right) \Delta v$$

$$- \Gamma \frac{(v_m + \Delta v) \sin\Delta\varphi}{2v_m(v_m + \Delta v)(1 - \cos\Delta\varphi) + \Delta v^2}.$$

We estimate the characteristic sizes of the microcaustic only for the azimuthal angle $\Delta\varphi = 0$. In this case, it follows from Eqs. (19) that $v_{csy} = 0$, and that the points of intersection of the caustic with the *OX* axis are given by the equality

$$v_{csx1,2} \approx v_m - \frac{1}{v_m} + \alpha v_m \pm \left(1 + \frac{1}{v_m^2} + \alpha \right) |\Delta v| \mp \frac{\Gamma}{|\Delta v|},$$

$$\tag{20}$$

$$|\Delta v| = \sqrt{\Gamma} \frac{v_m}{\sqrt{v_m^2(1 - \alpha) - 1}}.$$

Let us calculate the position of the center $\bar{v}_{csx} = \frac{1}{2}(v_{csx1} + v_{csx2})$ and half-width $\Delta v_{csx} = \frac{1}{2}(v_{csx1} - v_{csx2})$ of the microcaustic:

$$\bar{v}_{csx} \approx v_m - \frac{1}{v_m} + \alpha v_m,$$

$$\tag{21}$$

$$\Delta v_{csx} \approx \frac{2\sqrt{\Gamma}}{v_m} \frac{1 + \alpha v_m^2}{\sqrt{v_m^2(1 - \alpha) - 1}},$$

We see that, for the critical displacement $v_m = v_{cr}^M$, the position of the microcaustic center coincides with the position of the nearest macrocaustic beak (see Fig. 3a). As v_m increases ($v_m > v_{cr}^M$), $\bar{v}_{csx}$ increases and approaches the point where the microlens is located: $\bar{v}_{csx} \approx (1 + \alpha)v_m \approx v_m$. The characteristic size of the microcaustic is at a maximum near the critical curve of a regular GL and rapidly decreases to $\Delta v_{csx} \approx 2\alpha\sqrt{\Gamma}$ at $v_m \gg v_{cr}^M$.

When the microlens falls within the critical curve of a regular GL ($v_m < 1/\sqrt{1 - \alpha}$), the pattern differs from that considered above. The microcaustic breaks up into two located on both sides of the *OX* axis. We analyze the microcaustic structure in a single section corresponding to $\mathbf{v}$ on a circumference of radius $v = v_m$. Setting $\Delta v = 0$ in formula (19), we obtain in the linear (in $|\Delta\varphi| \ll 1$) approximation

$$v_{csx} \approx v_m - \frac{1}{v_m} + \alpha v_m + \frac{\Gamma}{2v_m} \approx v_m(1 + \alpha) - \frac{1}{v_m},$$

$$\tag{22}$$

$$\frac{v_{csy}}{\sqrt{\Gamma}} \approx \left(1 - \frac{1}{v_m^2} - \alpha \right) \Delta\tilde{v}_{cry} - \frac{1}{\Delta\tilde{v}_{cry}},$$

where $\Delta\tilde{v}_{\mathrm{cry}}$ are given by (17). The characteristic size of the microcaustic is estimated from (22) and (17) to be

$$|\Delta v_{csy}| \approx \frac{\sqrt{\Gamma}}{v_m} \left[\frac{1 + \alpha v_m^2}{\sqrt{1 + (1+\alpha)v_m^2}} - \sqrt{1 - (1-\alpha)v_m^2} \right]. \quad (23)$$

We see from the derived expressions that, when the microlens lies inside the critical curve of a regular GL, the caustic produced by it breaks up into two, which are roughly located in the $v = v_{csx}$ section symmetric on both sides of the *OX* axis (see Fig. 3b). When the microlens falls exactly on the critical curve $v_m = v_{\mathrm{cr}}^M$, the corresponding microcaustic lies at the point of the nearest macrocaustic beak ($v_{csx}^M \approx 2\alpha$). As the microlens moves into the regular curve, its microcaustic breaks up into two, which displace into the macrocaustic of a regular GL. From the condition $-2\alpha < v_{csx} < 2\alpha$, we determine the range of microlens displacements v_m for which the microcaustics are located within the curvilinear diamond of a regular GL: $1 - \frac{3}{2}\alpha < v_m < 1 + \frac{\alpha}{2}$.

Deriving formulas that are also valid for the other limiting case where the microlens moves along the *OY* axis ($\varphi_m = \pi/2$) involves no difficulty. To this end, $-\alpha$ must be formally substituted for α in all formulas. This substitution leads to the following differences in the behavior of the curves. When the microlens falls exactly on the critical curve of a regular GL ($v_m = v_{\mathrm{cr}}^M \approx 1 - \alpha/2$), the corresponding microcaustic falls at the point of the opposite macrocaustic beak ($v_{csy} = -2\alpha$). When the microlens is displaced outside the macrolens critical curve, the microlens critical curve has the shape of a single closed curve around the microlens. The single microcaustic corresponding to this case is displaced from point $v_{csy} = -2\alpha$ into the macrocaustic. At a distance $v_m \approx 1 + \alpha/2$, the microcaustic falls in the vicinity of the nearest macrocaustic beak and, as v_m increases further ($v_m > 1 + \alpha/2$), goes outside the macrocaustic while approaching the microlens position. When the microlens is displaced into the critical curve ($v_m < v_{\mathrm{cr}}^M$), the two forming microcaustics go from the point of the opposite beak $v_{csy} = -2\alpha$ outside the macrocaustic. We determine the range of impact parameters for the microlenses whose caustics fall within the macrocaustic from the condition $-2\alpha < v_{csy} < 2\alpha$: $1 - \frac{1}{2}\alpha < v_m < 1 + \frac{3}{2}\alpha$. Our qualitative analysis confirmed by numerical simulations allows us to roughly formulate the condition for the microcaustics falling within the caustic of

a regular GL at arbitrary microlens displacement angles φ_m:

$$1 - \alpha - \frac{\alpha}{2}\cos 2\varphi_m < v_m < 1 + \alpha - \frac{\alpha}{2}\cos 2\varphi_m. \quad (24)$$

In Fig. 2, the region of microlens impact parameters v_m satisfying the inequality (24) is hatched. When the microlens moves within the hatched region, the forming microcaustics (one or two, depending on whether the microlens is located outside or inside the critical curve of a regular GL) move along complex trajectories inside the caustic of a regular GL.

Let us now consider the most interesting case where the microlens lies in the immediate vicinity of the critical curve for a regular GL and can even fall on it. A numerical analysis of the curves emerging in this case (see Fig. 3c) shows that the macro- and microlines merge into a single complex continuous structure; differences in the shapes of the critical curves for the combined and regular GL are observed in the immediate vicinity of the microlens. We estimate the characteristic size of the deformed region for the case where the microlens lies exactly on the critical curve of a regular GL ($v_m = v_{\mathrm{cr}}^M$) in the $\varphi_m = 0$ direction. Given the above representations of the functions (14), Eq. (7) in the $\varphi = 0$ section can be written in the following approximate form:

$$4\Delta v^5 - 2\Gamma v_{\mathrm{cr}}^M [1 + \alpha(v_{\mathrm{cr}}^M)^2]\Delta v^2 - \Gamma^2(v_{\mathrm{cr}}^M)^3 = 0. \quad (25)$$

If we discard the last term proportional to Γ^2 in this expression, then the characteristic size of the perturbation introduced by the microlens can be estimated as $\Delta v \approx (\Gamma/2)^{1/3}$. For an in-depth analysis of the critical-curve shape, it is more convenient to bring the coordinate origin into coincidence with the microlens center rather than with the macrolens center, as previously. In the new system of $X'O'Y'$ coordinates, the equation of a complex GL can be readily derived from (5) by the formal substitution $\mathbf{v}' = \mathbf{v} - \mathbf{v}_m$. Given that the position of the macrolens center in the primed coordinate system $\mathbf{v}_m'$ is related to the microlens displacement vector in the old coordinate system v_m by $\mathbf{v}_m' = -\mathbf{v}_m$, we have

$$\mathbf{v}_s' = \mathbf{v}'\left(1 - \Gamma\frac{1}{v'^2}\right) + \alpha(v_x' - v_{mx}')\mathbf{e}_x$$
$$- \alpha(v_y' - v_{my}')\mathbf{e}_y - \frac{\mathbf{v}' - \mathbf{v}_m'}{(\mathbf{v}' - \mathbf{v}_m')^2}. \quad (26)$$

Below, to save space, we write all quantities by omitting primes while remembering that all designations refer to the new coordinate system. Given that $v_m \approx 1$ in the immediate vicinity of the microlens for the case under consideration ($v \ll v_m \approx 1$), we expand the last
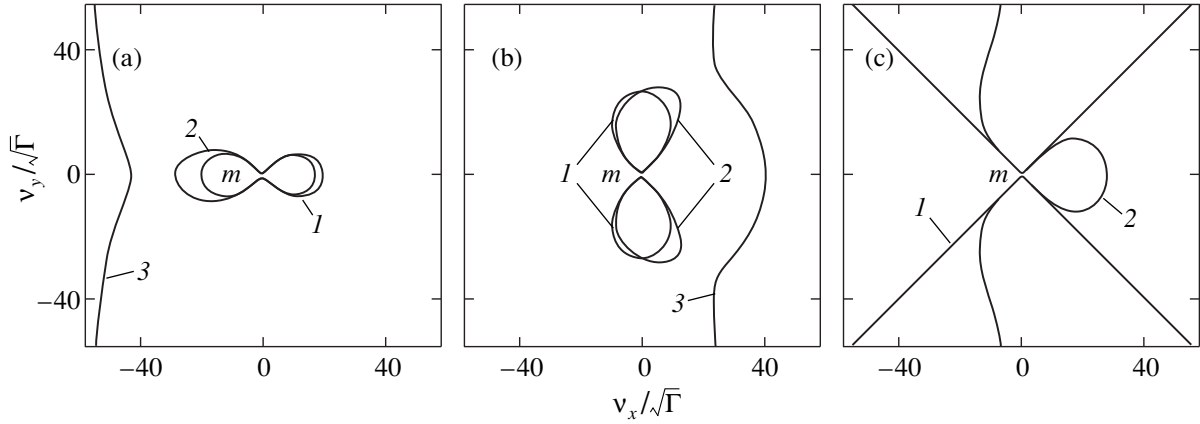
Fig. 6. Comparison of the critical curves obtained for $\Gamma = 10^{-9}$ in the linear (*1*) and quadratic (*2*) approximations when microlens *m* is located (a) outside, (b) inside, and (c) exactly on macrolens critical curve *3*.

term in (26) in a Taylor series up to quadratic terms inclusive. As a result, we obtain the following simplified lens equation:

$$
\tilde{\mathbf{v}}_s = \mathbf{v}\left(1 - \Gamma\frac{1}{\mathbf{v}^2}\right) + \alpha v_x \mathbf{e}_x - \alpha v_y \mathbf{e}_y - \left[\frac{\mathbf{v}}{\mathbf{v}_m^2} - \frac{2(\mathbf{v}\mathbf{v}_m)}{\mathbf{v}_m^4}\mathbf{v}_m\right]
$$
$$
- \left[\frac{\mathbf{v}_m}{\mathbf{v}_m^4}\mathbf{v}^2 + \frac{2}{\mathbf{v}_m^4}(\mathbf{v}\mathbf{v}_m)\mathbf{v} - \frac{4\mathbf{v}_m}{\mathbf{v}_m^6}(\mathbf{v}\mathbf{v}_m)^2\right]. \tag{27}
$$

Here, $\tilde{\mathbf{v}}_s = \mathbf{v}_s + \dfrac{\mathbf{v}_m}{\mathbf{v}_m^2} + \alpha v_{mx}\mathbf{e}_x - \alpha v_{my}\mathbf{e}_y$ is some effective source displacement. According to formula (6), we derive the equation for the GL critical curve in the new coordinate system
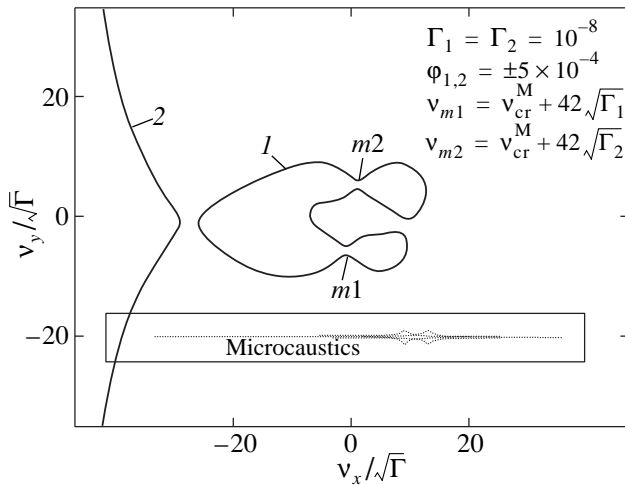
$$
q^{-1}\mathbf{v}^4 = \left[\left(1 - \alpha^2 - 2\frac{\alpha}{\mathbf{v}_m^2}\cos 2\varphi_m - \frac{1}{\mathbf{v}_m^4}\right)\mathbf{v}^4\right.
$$
$$
\left. - 4\left(\frac{\alpha}{\mathbf{v}_m^3}\cos(3\varphi_m - \varphi) + \frac{1}{\mathbf{v}_m^5}\cos(\varphi - \varphi_m)\right)\mathbf{v}^5 - 4\frac{\mathbf{v}^6}{\mathbf{v}_m^6}\right]
$$
$$
- 2\Gamma\left[\alpha\mathbf{v}^2\cos 2\varphi + \frac{\mathbf{v}^2}{\mathbf{v}_m^2}\cos(2\varphi - 2\varphi_m)\right.
$$
$$
\left. + 2\frac{\mathbf{v}^3}{\mathbf{v}_m^3}\cos(3\varphi - 3\varphi_m)\right] - \Gamma^2 = 0. \tag{28}
$$

Note that, in the standard approach widely used in the literature, only the linear expansion term is retained in the lens equation (27), while the last quadratic term is discarded. In this case, Eq. (28) would appear as follows:

$$
q^{-1}\mathbf{v}^4 = \left(1 - \alpha^2 - 2\frac{\alpha}{\mathbf{v}_m^2}\cos 2\varphi_m - \frac{1}{\mathbf{v}_m^4}\right)\mathbf{v}^4
$$
$$
\tag{29}
$$
$$
- 2\Gamma\frac{\mathbf{v}^2}{\mathbf{v}_m^2}\cos(2\varphi - 2\varphi_m) - 2\alpha\Gamma\mathbf{v}^2\cos 2\varphi - \Gamma^2 = 0.
$$

In the absence of a microlens ($\Gamma = 0$), Eq. (28) describes a small part of the critical curve for a regular GL near the origin of the coordinate system chosen. The condition for the microlens falling exactly on the critical curve of a regular GL can be formulated as follows. For $\Gamma = 0$ and $\nu = 0$ (the macrolens critical curve must pass through the origin of the coordinate system chosen), we must find ν_m and φ_m so as to satisfy Eq. (28). This is possible only for the displacements when $F_m(\nu_m, \varphi_m) = 1 - \alpha^2 - 2\dfrac{\alpha}{\nu_m^2}\cos 2\varphi_m - \dfrac{1}{\nu_m^4} = 0$. Hence, we obtain ν_m closely matching the previously inferred (10). Note that Eq. (29) for $\Gamma = 0$ has no reasonable solution at all; i.e., we cannot derive the equation for the macrolens critical curve from the linear approximation.

Just as in the old coordinate system, the form of the solution to Eq. (28) depends on the sign of $F_m(\nu_m, \varphi_m)$. When the microlens lies outside the critical curve of a regular GL, $F_m(\nu_m, \varphi_m) > 0$, and the critical curve has the shape of a single closed line enclosing the microlens position. If, alternatively, the microlens falls within the critical curve of a regular GL, then $F_m(\nu_m, \varphi_m) < 0$, and the solution can be represented as two closed lines on both sides of the microlens. Figure 6 shows the critical curves emerging near the microlenses in the immediate vicinity of the critical curve for a regular GL. The curves were constructed for $\Gamma = 10^{-9}$. For comparison, the same figure shows the critical curves obtained from the linear approximation (29).

$$\Gamma_1 = \Gamma_2 = 10^{-8}$$
$$\varphi_{1,2} = \pm 5 \times 10^{-4}$$
$$v_{m1} = v_{cr}^M + 42\sqrt{\Gamma_1}$$
$$v_{m2} = v_{cr}^M + 42\sqrt{\Gamma_2}$$

Fig. 7. Critical curve *1* and the caustic formed by two microlenses *m1* and *m2* when they are located near macrolens critical curve *2*.

The above analysis allowed us to keep track of the behavior of the critical and caustic curves for a complex GL composed of a regular macrolens and a single microlens at its arbitrary position relative to the critical curve of a regular GL. Under actual conditions, however, the number of microlenses near the critical curve can be large. If the spatial density of such microlenses is low (the microlenses are far apart), then we can assume that they do not interact with one another. In this case, the combined effect of stars, star-like or planet-like bodies close to the macrolens critical curve can be estimated as a sum of the effects from individual microlenses. If, alternatively, the density of microlenses is such that some of them are spaced at distances comparable to the sizes of their critical curves, then the interaction between microlenses must be taken into account. For such a situation, we can choose a finite number of terms in the immediate vicinity of a group of close microlenses from the total number N and write an equation similar to (1), where a finite number of close microlenses are added to the regular component of the refraction angle. In this case, the constraint ($l_m < |\mathbf{p} - \mathbf{p}_m| < a$) is removed. In order to estimate the characteristic separations between microlenses when their interaction must be taken into account, we carried out numerical simulations by using a GL model consisting of a regular macrolens and two close microlenses with different masses as an example. For this model, similar to (5), we can write the following lens equation:

$$\mathbf{v}_s = \mathbf{v}\left(1 - \frac{1}{v^2}\right) + \alpha v_x \mathbf{e}_x - \alpha v_y \mathbf{e}_y$$
$$- \Gamma_1 \frac{\mathbf{v} - \mathbf{v}_{m1}}{(\mathbf{v} - \mathbf{v}_{m1})^2} - \Gamma_2 \frac{\mathbf{v} - \mathbf{v}_{m2}}{(\mathbf{v} - \mathbf{v}_{m2})^2}. \tag{30}$$

Here, $\Gamma_{1,2} = r_{g1,2}/R_c \ll 1$ are small parameters, the mass ratios of microlenses and the galactic core, and $\mathbf{v}_{m1,2}$

are the positions of the microlens centers. Calculating the Jacobian of transformations from $\mathbf{v}_s$ to $\mathbf{v}$ and setting it equal to zero, we derive an equation for the GL critical curve. An analysis of the numerical solution for this equation indicates that the structure of the critical curves emerging near the microlenses depends markedly both on the separation between them and on their positions relative to the critical curve of a regular GL. As an example, Fig. 7 shows the critical curve and the corresponding caustic for one of the possible realizations.

CONCLUSION

Our theoretical analysis has led us to the following conclusions.

(1) A microlens deforms the critical curve and caustic of a regular GL. The deformations are proportional to Γ and rapidly decrease as the microlens recedes from the macrolens critical curve. For a fixed position of the radiation source, macrocaustic deformation results in an actual change of the distance from the source to the caustic, causing the corresponding intensity changes in the macroimages. Given that a fairly large number of microlenses can simultaneously be near the macrolens critical curve, their effect causes the boundaries of the macrolens critical curve and caustic to blur.

(2) The structure and behavior of the critical curves emerging near the microlens depend not only on the distance to the critical curve of a regular GL but also on the sector of angles in which the microlens moves. The characteristic sizes of the critical curves and microcaustics are proportional to $\sqrt{\Gamma}$.

(3) The largest deformations of the critical curves and caustics, which are proportional to $\Gamma^{1/3}$, are observed when the microlenses are located in the immediate vicinity of the critical curve for a regular GL. In this case, the macro- and microlens curves merge together to form complex continuous lines.

(4) The closer the microlenses to the critical curves, the larger the difference between our results and those obtained previously with standard (linearized) allowance for the effect of a regular GL.

(5) The microlensing effect of interacting microlenses increases considerably when they approach the critical curve of a regular GL.

To summarize, we can say the following. For GLs for which the observed source macroimages are located near the critical curves, the fact that the microlenses are close to the regular curves of macrolens galaxies must be taken into account when analyzing the microlensing effect.

REFERENCES

1. R. Blandford and R. Narayan, Ann. Rev. Astron. Astrophys. **30**, 311 (1992).

2. P. V. Bliokh and A. A. Minakov, *Gravitational Lenses* (Naukova Dumka, Kiev, 1989).

3. S. Kent and E. Falko, Astron. J. **96**, 1570 (1988).

4. A. A. Minakov and V. N. Shalyapin, Pis'ma Astron. Zh. **17**, 331 (1991) [Sov. Astron. Lett. **17**, 140 (1991)].

5. B. Paczynski, Astrophys. J. **301**, 503 (1986).

6. R. Schmidt, R. Webster, and G. Lewis, Mon. Not. R. Astron. Soc. **295**, 488 (1998).

7. P. Schneider, J. Ehlers, and E. E. Falko, *Gravitational Lenses* (Springer-Verlag, Berlin, 1992).

8. C. Seitz and P. Schneider, Astron. Astrophys. **288**, 1 (1994).

9. J. Wambsganss and B. Paczynski, Astron. J. **108**, 1156 (1994).

10. A. F. Zakharov and M. V. Sazhin, Usp. Fiz. Nauk **168**, 1041 (1998) [Phys. Usp. **41**, 945 (1998)].

Translated by V. Astakhov

[†] Deceased.

Cosmic Rays, Radio and Gamma-Ray Emission from the Remnant of Supernova 1987A

E. G. Berezhko* and L. T. Ksenofontov

Institute of Cosmophysical Research and Aeronomy, Siberian Division, Russian Academy of Sciences,
pr. Lenina 31, Yakutsk, 677007 Russia
Received December 23, 1999; in final form, April 20, 2000

Abstract—The acceleration of cosmic rays (CRs) in the supernova remnant (SNR) 1987A is investigated. A self-consistent theoretical description is based on the diffusion CR transport equation together with gas-dynamical equations for the medium (gas). The model consistently allows for the actual geometry of the expanding shock and for the inverse effect of accelerated CRs on its structure and dynamics. It also assumes that a 10^{-2} fraction of the gas particles are injected into the acceleration at the shock front. Parameters of the ambient medium—the SN 1987A progenitor wind—were chosen in such a way as to reproduce the observed expansion law of SNR 1987A. A single set of physical parameters is shown to ensure reasonable agreement between the calculated radio spectrum for SNR 1987A and available experiments. The expected spectrum of gamma rays from the decay of π^0 mesons produced when the CR nucleon component collides with ambient atoms is calculated. The integrated gamma-ray spectrum at energies $\epsilon_\gamma \lesssim 1$ TeV is hard, $F_\gamma \propto \epsilon_\gamma^{-0.6}$; the expected total flux $F_\gamma(1 \text{ TeV})$ at the current epoch is 7×10^{-13} cm^{-2} s^{-1}, and its two-fold rise is expected by 2006. © *2000 MAIK "Nauka/Interperiodica".*

Keywords: *cosmic rays, supernova remnants, radio and gamma-ray emission*

Supernova (SN) explosions have long been considered as the main source of cosmic rays (CRs) in the Galaxy (see, e.g., Berezinsky *et al.* 1990). The discovery of efficient CR acceleration by shock waves (Krymsky 1977; Axford *et al.* 1977), which is capable of converting a substantial fraction of the energy released during an explosion, and the development of a theory for this process [see, e.g., the reviews by Drury (1983), Berezhko and Krymsky (1988), and Berezhko *et al.* (1988) devoted to the theory of regular CR acceleration] put an experimental confirmation of theoretical predictions on the agenda. In other words, the problem of current interest is to obtain direct evidence that intense CR generation actually takes place in supernova remnants (SNRs).

SN 1987A, exploded on February 23, 1987, in the Large Magellanic Cloud [see the review by Mc Cray (1993) devoted to SN 1987A], offers a unique opportunity for testing theoretical models, as well as in revealing peculiarities of CR acceleration by supernova shocks.

The detection of the emission produced by CR particles is direct evidence for the presence of large quantities of CRs in SNRs. The CR electron component manifests itself by synchrotron radio emission (Berezinsky *et al.* 1990), which is recorded virtually from all the known SNRs, including SNR 1987A (Mc Cray 1993).

The presence of the CR nucleon component in a SNR can be directly established by measuring high-energy gamma-ray emission from the decay of π^0 mesons produced in nuclear collisions of CR particles with ambient atoms (see, e.g., Drury *et al.* 1994).

Radio emission from SNR 1987A was first detected two days after the explosion (Turtle *et al.* 1987). Having reached a peak value on day 4, the radio flux began to monotonically decrease. This pattern is in qualitative agreement with the ideas that the relativistic electrons generating radio emission are produced (accelerated) by a shock wave, which initially propagates through the supersonic wind of a blue supergiant, the SN 1987A progenitor (Storey and Manchester 1987; Chevalier and Fransson 1987).

After a prolonged period of "silence," the rising (with time) radio flux from SNR 1987A was redetected approximately 1200 days after the explosion (Staveley-Smith *et al.* 1992). The shock is presumed to have begun to propagate through the zone of the blue-supergiant thermalized wind in this period (Chevalier 1992). The ambient density and the magnetic-field strength in this zone are constant or even increase with distance, which provides a fairly rapid rise in the radio flux.

---

* E-mail address for contacts: berezhko@sci.yakutia.ru

A peculiarity of the radio emission from SNR 1987A is its soft spectrum: the radio spectral index $\alpha \approx$ 1 is considerably larger than $\alpha = 0.5$ typical of supernova remnants. The required accelerated-electron energy spectrum is characterized by an index $\gamma \approx 3$. Such a spectrum can be produced by a strong shock wave if it is significantly modified by the inverse effect of accelerated CRs. Calculations based on a simplified hydrodynamic approach argue for this scenario (Ball and Kirk 1992; Duffy *et al.* 1995). However, the hydrodynamic approach suffers from substantial drawbacks, which show up particularly clearly under conditions of efficient CR acceleration. The main drawback is that, for this method of description, the shock soon becomes completely modified, when all the free shock energy is converted into CRs, the medium (thermal plasma) crossing the shock front remains cold, and the particle injection into the acceleration ceases. As was established by Drury *et al.* (1995) and Berezhko (1996), this behavior of the solution is reproduced, because geometric factors were not properly taken into account when describing the dynamics of accelerated CRs. A consistent allowance for the finite sizes of the expanding shock reveals that it cannot be completely modified by the accelerated CRs. Irrespective of whether the shock expands in a homogeneous (Berezhko *et al.* 1996; Berezhko and Völk 1997) or inhomogeneous (Berezhko and Völk 1999) medium, the shock transition always contains the so-called thermal subshock in its structure, whose existence ensures heating of the medium followed by injection of the fastest particles into the acceleration. The spectral shape of the accelerated CRs is directly related to the pattern and degree of shock modification. It is therefore of interest to study the expected properties of CRs in SNR 1987A and the radio and gamma-ray emission produced by them on the basis of a consistent kinetic approach, which is free from the above shortcomings.

An analysis of the dynamics of the radio image for SNR 1987A, which is presumably bounded by the blast wave, shows that the shock velocity was extremely high within the first 1200 days after the explosion, $V_s \approx 3 \times 10^4$ km s^{-1} (Gaensler *et al.* 1997); this imposes significant constraints on the mass of the matter swept up by the shock and, eventually, on the blue-supergiant wind density. During the subsequent period of 1500–3000 days, the expansion velocity of SNR 1987A dropped by an order of magnitude, to $V_s \approx 3 \times 10^3$ km s^{-1}, which is explained by the shock entering the region of a dense wind from a red giant which the SN progenitor is generally believed to have been approximately 10^4 years before the explosion (Chevalier and Dwarkadas 1995; Gaensler *et al.* 1997).

Our detailed studies of CR acceleration in Type Ia SNRs expanding into a homogeneous interstellar medium (ISM) (Berezhko *et al.* 1994, 1995, 1996; Berezhko and Völk 1997; Berezhko and Ksenofontov 1999) and in Type Ib and II SNRs expanding into a medium modified by the SN progenitor wind

(Berezhko and Völk 1999), based on the kinetic theory, show that regular acceleration ensures the formation of a CR spectrum with the properties required to explain the observed Galactic CRs at energies up to 10^{14}–10^{15} eV. An analysis of individual SNRs will allow a tenable conclusion as to whether a theoretical description is proper to be reached.

Here, we use the nonlinear kinetic theory of regular CR acceleration in a SNR to account for the observed properties of radio emission and to calculate the expected gamma-ray flux from SNR 1987A. Our calculations take into account the views about the ISM structure in SNR 1987A that follow from experiment.

THE KINETIC THEORY OF CR ACCELERATION IN A SNR

Since the kinetic theory of regular (or diffusive) shock) acceleration of CRs in a SNR was detailed in our previous papers (Berezhko *et al.* 1994, 1995, 1996; Berezhko and Völk 1997, 1999), here we restrict ourselves to outlining its basic elements.

A SN explosion gives rise to an expanding envelope (ejecta), which initially contains all the energy E_{sn} released during the explosion in the form of mechanical motion. The ejecta at time t after the explosion is distributed in space with the density (Jones *et al.* 1981; Chevalier 1982)

$$\rho_{ej} = \begin{cases} Ft^{-3}, & v < v_t \\ Ft^{-3}(v/v_t)^{-k}, & v \geq v_t, \end{cases} \tag{1}$$

where

$$F = \frac{1}{4\pi k} \frac{[3(k-3)M_{ej}]^{5/2}}{[10(k-5)E_{sn}]^{3/2}}, \quad v_t = \left[\frac{10(k-5)E_{sn}}{3(k-3)M_{ej}} \right]^{1/2},$$

$v = r/t$ is the velocity of freely expanding elements of the ejecta, and

$$M_{ej} = 4\pi \int\limits_0^\infty dr\, r^2 \rho_{ej}(v = r/t, t)$$

is the envelope mass; the possible values of k lie in the range 8–12. The envelope internal pressure is negligible.

When describing the SNR evolution and the CR acceleration, we assume the system to be spherically symmetric. Under this assumption, all physical quantities are functions of one spatial variable, radial distance r.

While interacting with the ambient medium, the outer part of the ejecta composed of matter with the largest initial velocities v decelerates. We use a simplified description of the ejecta dynamics by representing it as two parts: a thin piston expanding with some single velocity V_p and composed of the decelerated ejecta and

the remnant of a freely expanding part of the initial distribution (1). Since the piston contains matter that had a velocity $v > R_p/t$ during free expansion, its mass is

$$M_p = 4\pi t^3 \int\limits_{R_p/t}^{\infty} dv \, v^2 \rho_{ej}(v, t), \qquad (2)$$

where R_p is the piston radius. The piston dynamics in the thin-layer approximation is described by the following simple equation:

$$\frac{d(M_p V_p)}{dt} = 4\pi R_p^2 [P_c(r = R_p - 0) \\ - P_g(r = R_p + 0) - P_c(r = R_p + 0)], \qquad (3)$$

where P_g and P_c are the gas and CR pressures, respectively; the pressure $P_c(r = R_p - 0)$ is produced by the CR particles penetrated through the piston. The degree of CR penetration through the piston is determined by the level of turbulence developing at the $r = R_p$ interface (contact discontinuity) between the ejecta and the swept-up ISM matter [see Berezhko and Völk (1997, 1999) for details].

It should be noted that the interaction of the ejecta with the ambient medium is accompanied by the formation of a reverse shock wave, which propagates through the ejecta, heats and compresses it. The outer part of the envelope swept up by the reverse shock is represented in our model as a piston of negligible thickness. At an early evolutionary stage (which we consider here) when the reverse shock interacts with the power-law portion of the distribution (1), the thickness of the region swept up by it $\Delta R \approx R_p/[\sigma(k - 3)]$ (Chevalier 1982) is more than an order of magnitude smaller than its size R_p, considering that the gas compression ratio at the shock front is $\sigma \approx 4$ and $k \approx 10$. This fact serves as a justification for the above simplified representation. Drury *et al.* (1989) used the thin-piston approximation not only to describe the ejecta dynamics but also for the ISM matter swept up by the shock.

The reverse shock can also accelerate some of the ambient particles swept up by it. However, the possibilities of this process have not yet been studied adequately. The main difficulty lies in the lack of reliable estimates for the magnetic-field strength in the ejecta, which is critical for the realization of efficient CR acceleration. If the magnetic field in this region is weak, which cannot be ruled out, one may hardly expect any effective CR acceleration. Therefore, as in most similar studies, we disregard the possible production of CRs by the reverse shock. It should also be added that, for the most general reasons, the number of CRs produced by the reverse shock is small compared to the contribution of the blast wave. Indeed, if we make use of the results by Chevalier (1982), it is easy to establish that, at the initial stage of evolution, the ratio of the internal energies of the medium swept up by the blast (or forward) and reverse waves, respectively, exceeds an order of magnitude: $E_{th}^b/E_{th}^r = 2(k - 3)^2/(k - 4) \gtrsim 15$. When the CRs acceleration is nonlinear (which must necessarily take place in SNR 1987A), the CR energy content accounts for a substantial fraction of the total internal energy E_{th}. Therefore, the expected energy-content ratio of the CRs produced by the reverse and forward waves, respectively, $E_c^r/E_c^b \lesssim 0.06$, indicates that the contribution of the reverse shock is small. This conclusion is confirmed by hydrodynamic calculations (Dorfi 1991); these calculations indicate that the contribution of the reverse shock to the CR production is tangible only during the transition period of SNR evolution from free expansion to Sedov's stage. In the case of SNR 1987A, the mass of the matter swept up by the shock is small compared to the mass of the ejecta during the entire period under consideration. This implies that SNR 1987A is far from Sedov' stage, which allows the contribution of the reverse shock to the CR production to be justifiably ignored.

The piston motion at a velocity well above the speed of sound c_S in the ambient medium generates a strong shock (usually called a blast wave), whose size $R_s > R_p$ increases at velocity $V_s = dR_s/dt$.

Our description of CR acceleration by the shock is based on the diffusive transport equation for the CR distribution function $f(r, p, t)$ (Krymsky 1964; Parker 1965):

$$\frac{\partial f}{\partial t} = \nabla(\kappa \nabla f) - \mathbf{w}_c \nabla f + \frac{\nabla \mathbf{w}_c}{3} p \frac{\partial f}{\partial p} + Q, \qquad (4)$$

where κ is the CR diffusion coefficient; p is the CR particle momentum; $w_c = w$ at $r < R_s$ and $w_c = w + c_a$ at $r > R_s$; w is the gas velocity; c_a is the velocity of the Alfven waves generated by the accelerated CRs in the upstream region $r > R_s$, where the growing waves mostly propagate outward. Since the Alfven turbulence becomes largely isotropic when passing through the shock front, the velocity of the scattering centers w_c at $r < R_s$ matches the gas velocity w.

We take into account only two CR components: protons, which are the main kind of ISM ions, and electrons. Since the energy content of the electron component is approximately two order of magnitude smaller than that of the nucleon component, its dynamical role is disregarded.

The source

$$Q = \frac{u_1 N_{inj}}{4\pi p_{inj}^2} \delta(p - p_{inj}) \delta(r - R_s) \qquad (5)$$

describes the injection of gas particles into the acceleration. In this expression, $u = V_s - w$, and p_{inj} is the injected-particle momentum. In what follows, the sub-

script 1 (2) corresponds to the point immediately ahead of (behind) the shock front.

The inverse effect of CRs results in a broadening of the shock front and in the formation, apart from an ordinary gas subshock, of an extended precursor. As in many problems of this kind, we treat the subshock as a discontinuity at $r = R_s$. The gas heats up when passing through the subshock, and a small fraction of the fastest gas particles are drawn (injected) into the acceleration.

The injection rate is specified by the free parameters η and λ, which determine the fraction of gas particles drawn into the acceleration and their momentum:

$$N_{\text{inj}} = \eta N_{g1}, \quad p_{\text{inj}} = \lambda m c_{S2}. \tag{6}$$

Here, m is the proton mass, $N_g = \rho/m$ is the proton number density.

The main condition that λ must satisfy is as follows: the momentum p_{inj} must be large enough for the diffusion approximation based on Eq. (4) to be applicable in the entire range $p \geq p_{\text{inj}}$. A direct comparison with the solution based on the kinetic equation shows that $\lambda \approx 4$ satisfies this requirement (Berezhko and Ellison 1999). Below, we therefore use $\lambda = 4$.

At the specified λ, the rate of gas-particle injection into the acceleration is determined by η. If the thermal proton distribution function in the region immediately behind the shock front $f_T(p)$ is known, η can be determined from the joining condition

$$f_T(p_{\text{inj}}) = f(r = R_s - 0, p_{\text{inj}}), \tag{7}$$

which, in view of the transport equation (4), yields

$$\eta = 4\pi p_{\text{inj}}^3 f_T(p_{\text{inj}})(\sigma_s - 1)/(3\sigma_s N_{g1}), \tag{8}$$

where $\sigma_s = u_1/u_2$ is the subshock compression ratio.

Note that the roles of λ and η describing injection are different. The choice of λ is largely arbitrary, considering that the nonrelativistic part of the accelerated-CR spectrum contains a small part of their total energy content. Thus, for example, the two solutions corresponding to different λ_1 and λ_2 match if the values of the other parameter are related by $\eta_2 = \eta_1(\lambda_1/\lambda_2)^{q-3}$, where q is the index of the spectrum $f \propto p^{-q}$ in the nonrelativistic range $p \ll mc$.

At present, both interplanetary experiments (see, e.g., Lee 1982; Trattner et al. 1994) and numerical simulations of collisionless shocks (Quest 1988; Trattner and Scholer 1993) irrefutably suggest the existence of fairly effective injection corresponding to the injection parameter $\eta = 10^{-4}$–10^{-2}. At the same time, currently available models describing injection of the fastest particles of the thermal distribution behind the shock front (see, e.g., Ellison et al. 1981; Malkov and Völk 1995) give no exhaustive prediction of the expected injection rate as a function of shock-transition parameters (in our

case, injection takes place at the subshock). In other words, there is no reliable theoretical description that would reproduce the distribution $f_T(p)$. Therefore, the injection rate η in our theory is a free parameter, whose value is chosen to achieve agreement with experiment.

Accelerated CRs intensively generate the Alfven waves in the precursor region. We therefore have reason to assume the Bohm CR diffusion coefficient (Völk et al. 1988)

$$\kappa(p) = \rho_B c/3, \tag{9}$$

where $\rho_B = pc/eB$ is the gyroradius of the particles with momentum p, B is the magnetic-field strength; c is the speed of light, and e is the proton charge. In addition, we take a relationship between the diffusion coefficient and the ambient density in the form $\kappa = \kappa_s \rho_s/\rho$, where the subscript s corresponds to the unperturbed medium at the current shock position $r = R_s$. The additional factor ρ_s/ρ prevents the development of precursor instability (Drury 1984; Berezhko 1986). Accordingly, the magnetic-field strength in the perturbed region is taken in the form $B = B_s\rho/\rho_s$.

The CR diffusion coefficient directly determines the maximum accelerated-particle energy, in accordance with the relation $\kappa(p_m) = R_s V_s/A$, where p_m is the maximum CR momentum, and the constant A is determined by the shock expansion law and by the ISM structure (Berezhko 1996). If the diffusion coefficient at high energies $p \gg mc$ is of the order of the Bohm one, then the typical maximum momentum is great, $p_m \sim 10^4$–$10^5 mc$, starting from the early stages of shock evolution. This ensures a high energy content of the accelerated CRs, resulting in a substantial shock modification. In this case, the specific form of the diffusion coefficient at lower energies $p \ll p_m$ is unimportant; what matters is that $\kappa(p)$ be a monotonically increasing function of momentum p. Note also that the maximum CR energy is determined by geometric factors—the finite size and shock deceleration, as well as adiabatic CR deceleration—rather than by a temporal factor, as has been thought previously (see, e.g., Lagage and Cesarsky 1983). It is this circumstance that prevents a complete shock modification and the disappearance of the subshock (Drury et al. 1995; Berezhko 1996).

The dynamics of the medium is described by the set of gas-dynamical equations

$$\frac{\partial \rho}{\partial t} + \nabla(\rho \mathbf{w}) = 0, \tag{10}$$

$$\rho \frac{\partial \mathbf{w}}{\partial t} + \rho(\mathbf{w}\nabla)\mathbf{w} = -\nabla(P_c + P_g), \tag{11}$$

$$\frac{\partial P_g}{\partial t} + (\mathbf{w}\nabla)P_g + \gamma_g(\nabla\mathbf{w})P_g = \alpha_a(1 - \gamma_g)c_a\nabla P_c, \tag{12}$$

where $\gamma_g = 5/3$ is the adiabatic index of the gas; the CR pressure is given by

$$P_c = \frac{4\pi c}{3} \int_0^\infty dp \frac{p^4 f}{\sqrt{p^2 + m^2 c^2}}. \qquad (13)$$

Eq. (12) takes into account heating of the medium in the precursor region through Alfven-wave dissipation (McKenzie and Völk 1984), which is reflected in the parameter $\alpha_a = 1$ at $r > R_s$. CR gradients in the post-shock region are small; as a result, there is virtually no generation of Alfven waves, and, hence, $\alpha_a = 0$ at $r < R_s$, and this effect is ignored.

Eqs. (4)–(6) and (9)–(12) are solved under the initial conditions

$$f(p) = 0, \quad \rho = \rho_0(r), \quad P_g = P_{g0}(r),$$
$$w = w_0(r), \qquad (14)$$

which describe the initial distribution of CRs and gas parameters at the SN explosion time ($t = 0$).

There is no need to solve the transport equation once again to derive the electron distribution function $f_e(p_e)$. For the chosen form of diffusion coefficient $\kappa(p)$ (9), the function $f_e(p)$ differs from the proton distribution function $f(p)$ only by a constant factor:

$$f_e(p) = K_{ep} f(p). \qquad (15)$$

To determine the constant K_{ep}, it will suffice to take into account the fact that the distribution function near the injection momentum is

$$f(p) = \frac{\eta N_{g1} q_s}{4\pi p_{inj}^3} \left(\frac{p}{p_{inj}}\right)^{-q_s}, \qquad (16)$$

$$q_s = 3\sigma_s'/(\sigma_s' - 1), \qquad (17)$$

$\sigma_s' = \sigma_s - c_a/u_2$, $\sigma_s = \rho_2/\rho_1$ is the subshock compression ratio. For simplicity, we take the same energy of the injected electrons as that for protons, i.e., $p_{inj}^e = \sqrt{m_e/m} p_{inj}$, where m_e is the electron mass. In this case, we have

$$K_{ep} = \frac{\eta_e}{\eta} \left(\frac{m_e}{m}\right)^{(q_s - 3)/2}. \qquad (18)$$

The differential (in kinetic energy ϵ_k) number density is related to the distribution function by

$$N(\epsilon_k) \equiv \frac{dN}{d\epsilon_k} = \frac{dN}{dp} \frac{\epsilon}{pc^2} = 4\pi \frac{p\epsilon}{c^2} f(p), \qquad (19)$$

where $\epsilon = \sqrt{p^2 c^2 + m^2 c^4}$ is the total energy of the particle of mass m, and c is the speed of light. We thus see that, for a purely power-law distribution function $f \propto p^{-q}$, the particle energy spectrum undergoes a break at

$\epsilon_k \sim mc^2$ due to a kinematic effect: $N \propto \epsilon_k^{(1-q)/2}$ at $\epsilon_k \ll mc^2$ and $N \propto \epsilon_k^{(2-q)}$ at $\epsilon_k \gg mc^2$. Therefore, the electron and proton spectra are related by

$$N_e/N = K_{ep}(m/m_e)^{(q-3)/2} = \eta_e/\eta, \qquad (20)$$

at nonrelativistic energies $\epsilon_k \ll m_e c^2$ and by

$$N_e/N = K_{ep}. \qquad (21)$$

at relativistic energies $\epsilon_k \gg mc^2$.

In what follows, quantities with the subscript e and without subscripts refer to electrons and protons, respectively. For the same electron and proton injection rates ($\eta_e = \eta$) at relativistic energies $\epsilon_k > mc^2$, the electron number density is lower than the proton one by a factor of $(m_e/m)^{(q-3)/2}$. Since $q \approx q_s$ at $p \sim mc$, with the spectral index lying in the range $q_s = 4.5$–5 due to the shock modification by the accelerated protons, the expected number of electrons at relativistic energies $\epsilon \gg 1$ GeV is approximately a factor of 100 smaller than that of protons, as in Galactic CRs.

It is important to note that the above relationship between the accelerated-proton and electron spectra holds when the injected-particle energy $\epsilon_{inj} = p_{inj}^2/(2m)$ does not exceed $m_e c^2$. It is easy to show that, otherwise (when $m_e c^2 < \epsilon_{inj} < mc^2$), the factor K_{ep} is given by

$$K_{ep} = \frac{\eta_e}{\eta} \left(\frac{\epsilon_{inj}}{mc^2}\right)^{(q_s - 3)/2}. \qquad (22)$$

Since the shock expansion is accompanied by its deceleration, with the injected-particle energy $\epsilon_{inj} \propto V_s^2$ initially exceeding m $m_e c^2$, one might expect K_{ep} to smoothly decrease in the course of SNR evolution.

For the radio flux from a SNR to be calculated, the absolute value of the spectrum of the accelerated relativistic electrons $N_e(\epsilon_k)$ must be known, for which it will suffice to specify K_{ep}. Nevertheless, from the viewpoint of the requirements imposed on the injection mechanism, it is important to know how the electron and proton energy spectra are related at low energies $\epsilon_k = \epsilon_{inj}$. To this end, we introduce an injection parameter η_e uniquely related to K_{ep}, which directly determines the fraction of the electrons drawn into the acceleration. Some uncertainty in η_e is attributable to the assumption of $\epsilon_{inj}^e = \epsilon_{inj}$, which cannot be strictly justified. However, if electrons with energies below ϵ_{inj} are drawn into the acceleration, the above value of η_e is exact: it gives the correct number of accelerated electrons whose energy is above ϵ_{inj}. For $\epsilon_{inj}^e > \epsilon_{inj}$, the proton injection rate η can be recalculated to the energy $\epsilon_{inj}' = \epsilon_{inj}^e$. Using the above formulas, it is easy to establish that the relation $\eta_e'/\eta' = \eta_e/\eta$ holds for $\epsilon_{inj}' < m_e c^2$; i.e., the

value of η_e we use gives the correct relationship between the numbers of accelerated electrons and protons. Otherwise (when $\epsilon_{inj} > m_e c^2$), we have $\eta_e' / \eta' = (\epsilon_{inj}' / \epsilon_{inj})^{(q_s - 3)/2} \eta_e / \eta$; i.e., the η_e / η ratio is a lower limit. It can be added that the condition $\epsilon_{inj}^e = \epsilon_{inj}$ may well correspond to an actual situation, in agreement with the Bohm particle diffusion. Indeed, the main requirement imposed on ϵ_{inj} is an excess of the diffusion length $\kappa(\epsilon_{inj})/u_1$ over the subshock thickness l_g (that is why l_g is taken to be zero when the CR dynamics is considered); hence, $\epsilon_{inj}^e = \epsilon_{inj}$ at $\kappa \propto \epsilon_k$ (the mean free path before scattering $\lambda \propto p$).

It should be noted that the situation with electron injection into acceleration is considerably more complex than that for protons both experimentally and theoretically. Although the available theoretical analysis (Levinson 1992, 1994, 1996; Bykov and Uvarov 1999) points to the existence of possible mechanisms producing electron injection at the front of a strong shock, unfortunately, there is no exhaustive answer to the question of what plasma parameters determine the expected electron injection rate, in particular, its dependence on the magnetic-field structure and its relationship to the ion injection rate. As for experiment, direct evidence that electrons, just as ions, are injected and accelerated at interplanetary shock fronts is very scarce. The study by Terasawa *et al.* (1999), who presented spectral measurements of accelerated electrons and protons near an interplanetary shock front, suggesting that electrons are injected into the acceleration as effectively as protons, constitutes an exception. This serves as an additional justification for the relation $\eta_e \sim \eta$, which we use below to explain the properties of radio emission from SN 1987A. The considerably lower injection rate of electrons compared to that of protons ($\eta_e \ll \eta$) does not satisfy the experimental requirements for SN 1006 either (Berezhko *et al.* 1999).

THE ISM STRUCTURE NEAR SN 1987A

How the CR acceleration proceeds depends markedly on the structure of the ISM through which a shock propagates. In the case of SN 1987A under consideration, there is compelling evidence that the ambient ISM is significantly modified by the progenitor wind; the properties of this wind changed during the progenitor evolution (Mc Cray 1993).

Here, we restrict ourselves to analyzing the initial period of SNR 1987A evolution, which corresponds to the blast-wave propagation through the $r < R_R$ region inside a highly inhomogeneous ring-shaped clump at $R_R = 6 \times 10^{17}$ cm (Mc Cray 1993). This region consists of three zones. The first (zone I) is occupied by the

supersonic wind from a blue supergiant (which the progenitor of SN 1987A has been for the last 10^4 years) of constant velocity $w_0 = V_w$ with the density

$$\rho_0 = \frac{\dot{M}}{4\pi V_w r^2}, \tag{23}$$

where $\dot{M}$ is the mass-loss rate.

The magnetic field is twisted into an Archimedes spiral because of the stellar rotation. For simplicity, we use its value in the equatorial plane

$$B_0 = B_* \frac{R_*}{r} \sqrt{\left(\frac{R_*}{r}\right)^2 + \left(\frac{R_* \Omega}{V_w}\right)^2}. \tag{24}$$

Here, Ω is the star rotation rate, R_* is its radius, and B_* is its surface magnetic field.

At some distance $r = R_T$, the wind undergoes a shock transition through the interaction with the ambient medium at which the Rankine–Hugoniot relations hold:

$$\rho_{02} = 4\rho_{01}, \quad w_{02} = V_w/4, \quad B_{02} = 4B_{01},$$
$$P_{02} = (3/4)\rho_{01} V_w^2, \tag{25}$$

where ρ_{01} and B_{01} are given, respectively, by (23) and (24) at $r = R_T$; the subscript 1 (2) denotes quantities that refer to the upstream (downstream) region, and we take into account the fact that the shock is strong with the compression ratio $\sigma = \rho_{02}/\rho_{01} = 4$. Since the shock velocity V_s considerably exceeds w_{02}, the results are virtually insensitive to the form of the velocity field $w(r)$. We therefore assume, for simplicity, that the medium at $r > R_T$ is stationary ($w_0 = 0$) and isobaric ($P_{g0} = P_{02}$).

The shock position in the stellar wind changes with time. However, the expected shock velocity $V_T = dR_T/dt$ is low compared the supernova shock velocity V_s. We therefore consider the shock in the stellar wind as a stationary (termination) wave.

When the progenitor wind interacts with the ambient homogeneous medium, the $r > R_T$ region occupied by a thermalized wind is roughly homogeneous. However, an analysis of the dynamics of the expanding radio-emitting region presumably bounded by the supernova shock shows (Chevalier and Dwarkadas 1995) that the shock enters a region with a considerably higher ambient density at some distance $R_C > R_T$; as a result, it rapidly decelerates. This zone III consists of the denser matter of the wind from a red supergiant, which the progenitor of SN 1987A was at the next-to-last evolutionary stage, before it passed to the blue-supergiant stage (see, e.g., Chevalier and Dwarkadas

1995). It is convenient to represent the presence of two zones in the $r > R_T$ region as the density distribution

$$\rho_0 = \frac{\rho_{II} + \rho_{III}}{2} - \frac{\rho_{II} - \rho_{III}}{2} \tanh\frac{r - R_C}{l}, \qquad (26)$$

which describes a smooth transition from $\rho_{II} = \rho_{20}$ to $\rho_{III} \gg \rho_{II}$ at length $l \ll R_C$ near the contact boundary $r = R_C$. The value of $l = 0.05R_C$, which we used in our calculations, is small enough for the presence of a transition region between zones II and III to have no effect on the solution. At the same time, it allows a continuous numerical solution to be reproduced in the entire $r > R_T$ region.

Similarly, the magnetic-field distribution in the $r > R_T$ region is assumed in the form

$$B_0 = \frac{B_{II} + B_{III}}{2} - \frac{B_{II} - B_{III}}{2} \tanh\frac{r - R_C}{l}, \qquad (27)$$

which corresponds to $B_{II} = B_{02}$ in zone II and B_{III} in zone III.

It should be noted that the most important ISM parameters determining the CR acceleration and the shock dynamics are the density $\rho_0(r)$ (or the number density $N_g = \rho_0/m$) and magnetic field $B_0(r)$. The thermal pressure P_{g0}, which directly determines the speed of sound in the medium $c_{S0} = \sqrt{\gamma P_{g0}/\rho_0}$, plays no significant role. In the case under consideration, the relation $M_a \ll M_S^2$ holds between the sonic ($M_S = V_s/c_{S0}$) and Alfvén ($M_a = V_s/c_{a0}$) Mach numbers for which the shock structure and the CR-acceleration properties are entirely determined by M_a and are virtually independent of M_S. The radial profiles of number density $N_g(r)$ and magnetic field $B_0(r)$, which are used in our calculations below, are shown in Fig. 1. In this case, the $\rho_0(r)$ profile was obtained from the requirement of the best reproduction of the observed shock dynamics, i.e., the reproduction of $R_s(t)$ and $V_s(t)$ whose values are extracted from the observed dynamics of the radio image for SN 1987A (Gaensler *et al.* 1997). Our adopted profile $\rho_0(r)$ at $r > R_T$ slightly differs from that obtained by Chevalier and Dwarkadas (1995) by the parameters R_T, R_C, and ρ_{III} (see below).

Note that the crossing of the termination shock front in the stellar wind ($r = R_T$) by the supernova shock is accompanied by a complex process of the formation of a series of secondary shocks. While propagating between the shock front and the piston, these secondary shocks ensure a transition to a new quasi-steady-state corresponding to a new state of the medium, which abruptly changed at the termination shock front. For simplification, we ignore this complex, relatively short-
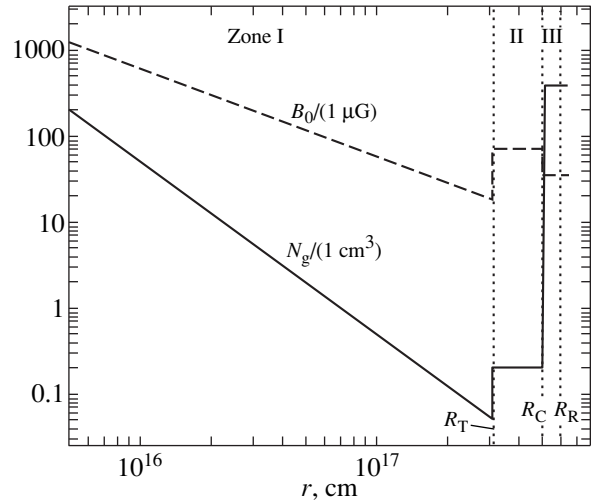
Fig. 1. The radial profiles of gas number density (solid line) and magnetic field (dashed line) around the progenitor of SN 1987A. The positions of the termination shock front in the blue-supergiant wind (R_T), the contact boundary (R_C) separating the zones occupied by the winds from the blue and red supergiants, respectively, as well as the inner edge of the ring-shaped clump (R_R) are shown.

lived relaxation process. We describe the shock propagation at $r > R_T$ for the initial conditions

$$R_{si} = R_{pi} + 0 = R_T + 0, \quad V_{pi} = V_{pT}, $$
$$f(r, p) = 0, \qquad (28)$$

where V_{pT} is the piston velocity at $r = R_T - 0$, i.e., at the exit from the supersonic-wind zone. In this case, the simplification consists in ignoring all the CRs accelerated in the $r < R_T$ zone. This is justified by the fact that the number of newly produced CRs in the $r > R_T$ zone will soon exceed considerably what was produced in the $r < R_T$ zone.

Thus, the formulated problem reduces to solving the set of gas-dynamical equations (10)–(12) together with the CR transport equation (4) and the equation of piston motion (3) with the initial conditions (14): in zone I, $P_{g0} = 0$, $w_0 = V_w$, and the ambient density ρ_0 and magnetic field B_0 are specified by formulas (23) and (24), respectively; in zones II and III, $w_0 = 0$, $P_{g0} = P_{20}$, and the density ρ_0 and magnetic field B_0 are given, respectively, by (26) and (27). In this case, our theoretical description contains η and η_e (or K_{ep}), which specify the rate of particle injection into the acceleration, as free parameters. In addition, the problem includes a number of physical parameters for the system (E_{sn}, M_{ej}, k, R_*, Ω, ρ_0, B_0) on which its solution depends: E_{sn}, M_{ej}, and k are known from observations of SN 1987A during an early period of its evolution, while the remaining parameters (η, K_{ep}, ρ_0, and B_0) are chosen by the criterion for the best reproduction of the observed properties of radio emission from SN 1987A.
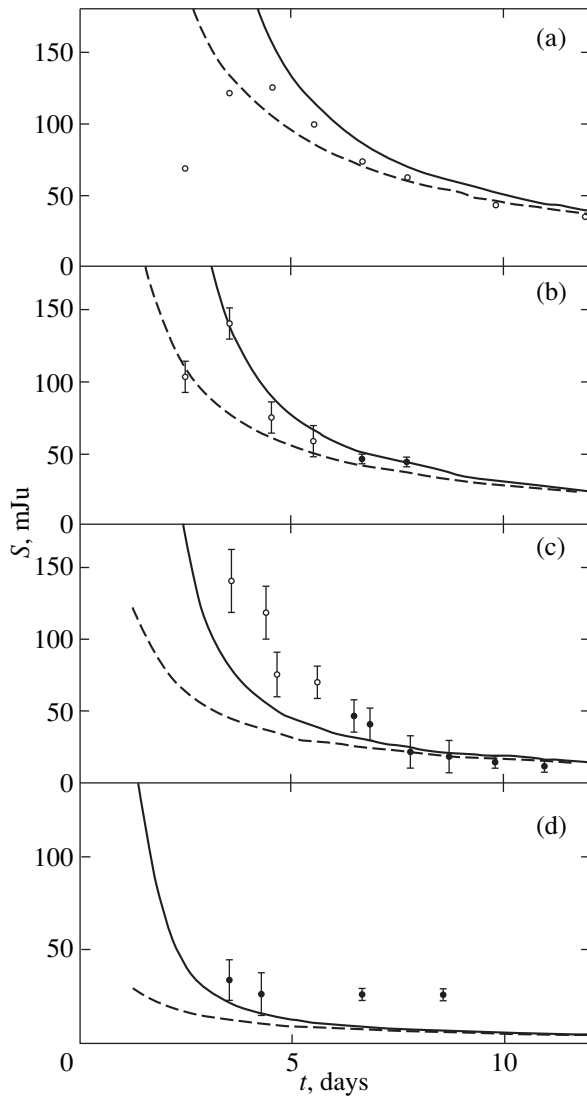
Fig. 2. The radio flux from SNR 1987A for four frequencies ν: (a) 0.84, (b) 1.4, (c) 2.3, and (d) 8.4 GHz versus time measured from the supernova explosion. The dashed and solid lines correspond to the angular velocities of the supernova progenitor $\Omega = 5 \times 10^{-7}$ c^{-1} and 4×10^{-8} c^{-1}, respectively. Experimental values were taken from Turtle *et al.* (1987).

We solved the formulated problem numerically. To this end, we used our algorithm developed for a homogeneous ISM (Berezhko *et al.* 1994, 1995, 1996; Berezhko and Völk 1997) and generalized to an arbitrary spherically symmetric distribution of parameters of the gas around the supernova progenitor (Berezhko and Völk 2000).

CALCULATIONS AND THEIR DISCUSSION

In our calculations, we used the parameters of SN 1987A inferred from observations (Mc Cray 1993): $E_{sn} = 1.5 \times 10^{51}$ erg, $M_{ej} = 10 M_\odot$, and $k = 8.6$, as well as the typical parameters of a blue supergiant: $R_* = 3 \times 10^{12}$ cm and $\Omega = 5 \times 10^{-7}$ s^{-1}. The initial piston velocity

$V_{pi} = 40000$ km s^{-1} and the mass-loss rate of the blue supergiant $\dot{M} = 7.5 \times 10^{-8} M_\odot$ yr^{-1}, where $M_\odot$ is the solar mass, were chosen in accordance with the estimates by Chevalier and Dwarkadas (1995) to ensure the observed shock expansion velocity at the initial stage of evolution $t < 1500$ days.

The other parameters—the progenitor surface magnetic field B_*, injection rate η, and radii R_T and R_C—were chosen in such a way as to reproduce the observed properties of the radio emission from SNR 1987A.

We calculated the radio flux, which is synchrotron radiation of relativistic electrons, by using the formula (Berezinsky *et al.* 1990)

$$S = \frac{13500}{d^2} \int_0^\infty dr r^2 aCB_\perp^{\frac{\gamma+1}{2}} \left(\frac{6.26 \times 10^{18}}{\nu}\right)^{\frac{\gamma-1}{2}} \text{mJu}, \quad (29)$$

where ν is the frequency of the radio emission,

$$a = \frac{\sqrt{3}2^{\frac{\gamma-1}{2}}\Gamma\left(\frac{3\gamma-1}{12}\right)\Gamma\left(\frac{3\gamma+19}{12}\right)\Gamma\left(\frac{\gamma+5}{4}\right)}{8\sqrt{\pi}(\gamma+1)\Gamma\left(\frac{\gamma+7}{4}\right)},$$

$\gamma = -d\ln N_e/d\ln\epsilon_e$ is the local index of the electron energy spectrum, $\Gamma(x)$ is the Gamma function, $C = N_e\epsilon_e^\gamma$, $\epsilon_e = m_ec^2\sqrt{8.3 \times 10^{-7}\nu/B_\perp}$, $d = 50$ kpc is the distance to SN 1987A, and $B_\perp$ is the magnetic-field component perpendicular to the line of sight. In the case under consideration, the emitting electrons concentrate in a narrow region behind the front. We therefore disregard the dependence of the magnetic field on coordinate r and take $B_\perp = 0.5\sigma B_0(R_s)$ with some degree of arbitrariness.

The constant C and the spectral index γ are complex function of injection rate η. At low injection rates $\eta < 10^{-5}$, when the CR energy content is small and the acceleration takes place in a linear regime, $C \propto \eta$ and $\gamma \approx 2$ (Berezhko *et al.* 1996). However, at the expected injection rates $\eta = 10^{-3}$–10^{-2}, when the shock structure is significantly modified by the inverse effect of CRs, there is a complex, nonlinear relationship between the injection rate and the particle spectrum at relativistic energies.

The calculations presented below correspond to $B_* = 59$ G and $\eta = 10^{-2}$, which were chosen from several calculations performed for various B_* and η using the criterion for the closest reproduction of the observed properties of radio emission from SNR 1987A.

Our calculations of parameters for the shock, CRs, and the emission produced by them during the shock propagation in the supersonic-wind zone at $r < R_T$ are shown in Figs. 2 and 3.

In Fig. 2, the calculated radio fluxes at four frequencies are compared with their experimental values mea-
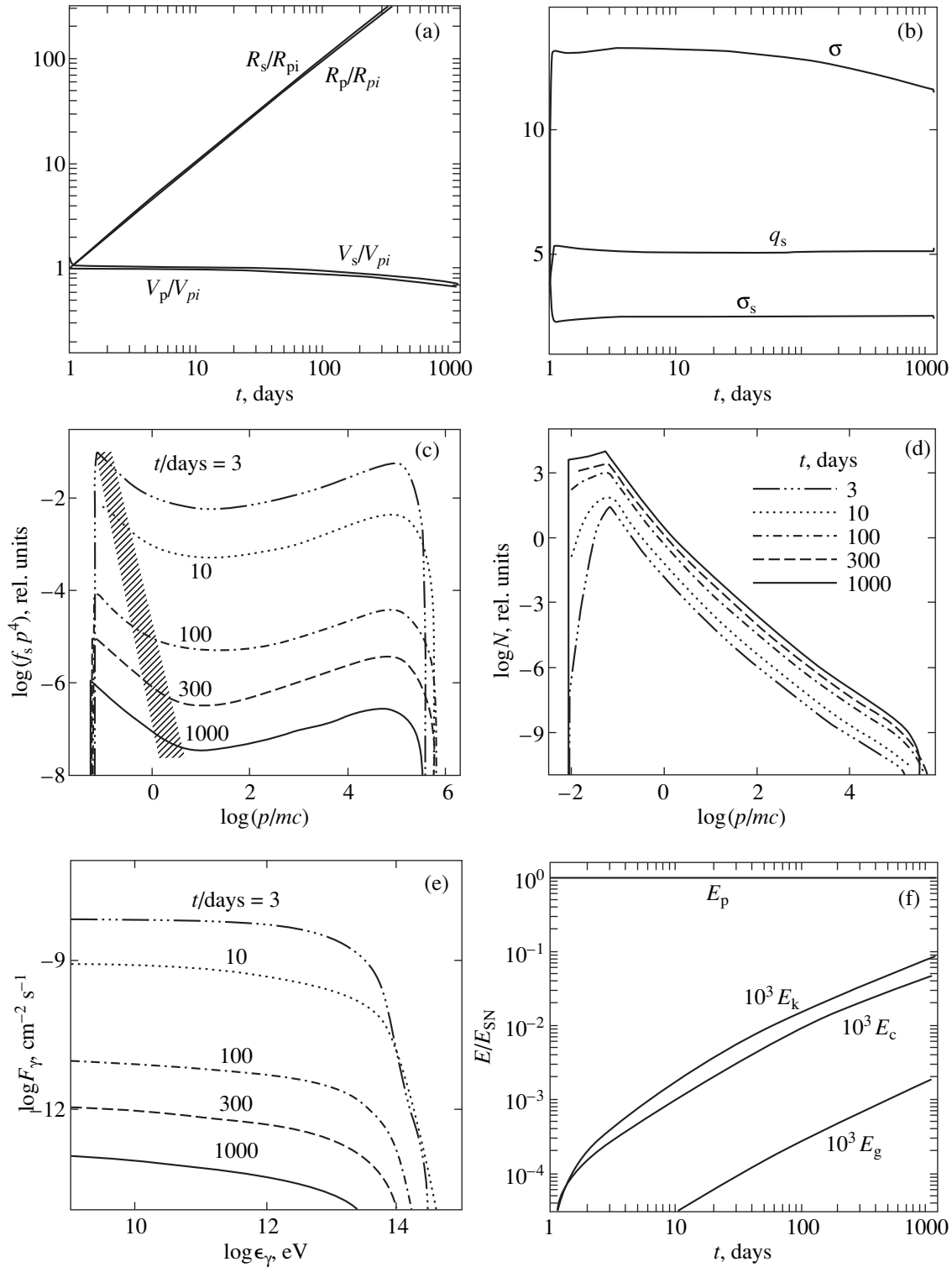
Fig. 3. (a) The radius and velocity of the shock (R_s and V_s) and the piston (R_p and V_p); (b) the total compression ratio σ, the subshock compression ratio σ_s, and the spectral index q_s; (f) the CR energy E_c, kinetic (E_k) and thermal (E_g) energies transferred by the shock to the gas, and the ejecta energy E_p versus time. (c) The distribution function of the accelerated CRs at the shock front versus momentum, (d) the overall accelerated-CR spectrum versus momentum, and the total gamma-ray flux versus energy for times $t = 3$, 10, 100, 300, and 1000 days from the explosion. The initial piston size and velocity are $R_{pi} = 3.46 \times 10^{14}$ cm and $V_{pi} = 40000$ km s^{-1}, respectively. The hatched region corresponds to the momenta of electrons emitting in the frequency range $\nu = 0.84$–8.4 GHz.

sured within 12 days after the supernova explosion (Turtle *et al.* 1987). We see that the observed behavior (rise) of flux S in the first three days differs markedly from predictions of the theory, which, on the contrary, reproduces the monotonic decrease in flux S with time at all frequencies. This can be attributed to self-absorption of the radio emission at an early stage of evolution (Mc Cray 1993), which we disregarded in our calculations. At $t > 3$ days, when the absorption of the emission presumably becomes small, the theory is in qualitative agreement with experiment. At the same time, we see that the theory predicts underestimated fluxes $S(\nu)$ during the initial period $t = 3–5$ days. In other words, the experimental flux during this period decreases more rapidly than does the theoretical one. This can be assumed to be explained by a more rapid decrease of the wind density or of the magnetic-field strength at small distances r than that given by formulas (23) and (24), respectively. The latter can be caused by an increase in mass loss rate $\dot{M}$ immediately before the explosion (see, e.g., Chevalier and Dwarkadas 1995). Figure 1 also shows the calculation corresponding to the progenitor rotation rate $\Omega = 4 \times 10^{-8}$ s^{-1}. In this case, the wind magnetic field at large distances $r \gg V_w/\Omega \approx 10^{15}$ cm was taken to be the same as that in the previous case: according to formula (14), this implies that the stellar surface magnetic field in the latter case is $B_* = 649$ G. This magnetic-field strength should be considered to be overestimated, while the rotation rate $\Omega = 4 \times 10^{-8}$ s^{-1} should be considered to be underestimated for the blue supergiant. Therefore, the second calculation most likely illustrates the effect of increase in $\dot{M}$ before the explosion, resulting in a more rapid falloff of the ambient density and magnetic field at small r: as we see from (24), the region of distances r where the magnetic field falls off more rapidly than r^{-1} expands with decreasing Ω. As is evident from Fig. 1, in this case, the theory at $t > 3$ days satisfactorily reproduces both the time dependence (decline) of the radio flux and the spectral shape characterized by an index $\alpha \approx 0.9$ for a power-law fit $S \propto \nu^{-\alpha}$, which corresponds to an index $\gamma \approx 2.8$ of the electron energy spectrum.

Such a soft spectrum at the energies of the electrons $\epsilon_e = 0.1–1$ GeV producing synchrotron radiation in the frequency range $\nu = 0.84–8.4$ GHz under consideration results from the supernova shock being strongly modified by the inverse effect of CRs (see Fig. 3). In Fig. 3b, the total compression ratio $\sigma = \rho_2/\rho_s$, the compression ratio $\sigma_s = \rho_2/\rho_1$, and the CR spectral index q_s at $p < mc$ are plotted against time. We see that, during the entire period $t < 10^3$ days, the degree of compression considerably exceeds the classical value of 4. In the early period ($t \lesssim 10$ days), $\sigma \approx 13$ and then slowly decreases to $\sigma \approx 11$ at $t = 10^3$ days. The subshock compression ratio remains approximately constant, $\sigma_s \approx 3.2$.

It is important to note that the proton injection rate η is the main parameter affecting the degree of shock modification; the required substantial modification can be achieved if the injection rate exceeds the critical value (Berezhko and Ellison 1999)

$$\eta_* = \frac{3V_s}{10\sqrt{2}\lambda c}\left(\frac{p_m}{mc}\right)^{-1/4}. \qquad (30)$$

The shock is unmodified for $\eta < \eta_*$, $\sigma = \sigma_s = 4$, yielding the radio spectral index $\alpha = 0.5$, which is clearly in conflict with experiment. In our case, $\eta_* \sim 10^{-3}$ and $\eta = 10^{-2} > \eta_*$ is needed to ensure the required degree of modification with $\sigma_s \approx 3$.

For the chosen proton injection rate η, the parameters directly affecting the intensity of the radio emission are the magnetic field B_* and the electron injection rate η_e (or K_{ep}). As we see from Fig. 2, $B_* = 59$ G and $K_{ep} = 0.04$ ($\eta_e \approx 8\eta$) ensure reasonable agreement with experiment. Since, according to (29), $S \propto B_*^2 K_{ep}$, approximately the same agreement can be achieved at other values of B_* and K_{ep} giving the same product $B_*^2 K_{ep}$. We used B_* typical of a blue supergiant at which the required $\eta_e \approx 8\eta$, which is kept constant in our calculation, ensures that $K_{ep} = 0.01$ at the stage when $\epsilon_{inj} < m_e c^2$ (see below). This value, in our view, seems most acceptable, because it agrees with the electron-to-proton ratio in Galactic CRs. $K_{ep} = 0.01$ is also in agreement with theoretical electron injection rates (Bykov and Uvarov 1999).

The shape of the accelerated-particle spectrum is shown in Fig. 3c, where the CR (proton) distribution function at the shock front $f_s(p, t) = f(r = R_s, p, t)$ is plotted against momentum p for five times [recall that the electron spectrum in the presented range of momenta has the same shape, in accordance with relation (15)]. We see from the figure that the proton spectrum is complex because of the strong shock modification. At $p < mc$, it is similar to a power law $f \propto p^{-q}$ with $q = q_s$. The particles of such low energies have a low energy content and a small diffusion length $l = \kappa/u$. Therefore, they "feel" only the subshock during the acceleration, and their spectral shape is similar to the universal one corresponding to the compression ratio $\sigma = \sigma_s$. According to Fig. 3b, the spectral index of the radio-emitting electrons is $q \approx q_s \approx 5$, corresponding to the radio spectral index $\alpha \approx 1$, which is in good agreement with experiment.

By contrast, the CR spectrum at high energies, $10mc < p < 10^5 mc$, is very hard: $f_s \propto p^{-q}$, $q \approx 3.65$ (see Fig. 3c). Note that this spectral index is close to the minimum possible value $q_{min} = 3.5$, which can occur during the shock acceleration (Berezhko 1996).

As we see from Fig. 3c, the cutoff (or maximum) momentum p_m varies only slightly with time. Its value

is determined by geometric factors and by adiabatic CR acceleration for the Bohm diffusion coefficient (9),

$$\frac{p_m}{mc} = \frac{R_s V_s}{A\kappa_s(mc)},\tag{31}$$

where the parameter A is determined by the time dependence of R_S, ρ_s, and B_s (Berezhko 1996). During the initial period $t < 100$ days, given that the velocity V_s is constant, we have $\rho_s \propto t^{-2}$ and $B_s \propto t^{-1}$, which yields $A = 3/4$ in the case of strong nonlinearity (see Berezhko 1996) and $p_m \approx 10^5 mc$, in good agreement with our calculations. At $t > 100$ days, the shock expands as $R_s \propto t^{\frac{k-3}{k-2}} = t^{0.85}$, and the maximum momentum can be represented as

$$\frac{p_m}{mc} = 10^5\left(\frac{t}{100 \text{ days}}\right)^{-0.15},\tag{32}$$

in good agreement with the exact calculation (Fig. 3c). Remarkably, a shock of small sizes $R_s \ll 1$ pc is capable of generating CRs with energies up to 10^{14} eV, which is mainly attributable to the very high shock velocity.

The fact that the shape of the particle distribution function $f_s(p)$ is almost constant with time engages our attention; its value at all momenta decreases with time approximately as $f_s \propto t^{-2}$. As was shown by Berezhko and Völk (2000), a self-similar solution of the form $f_s(p, t) = \phi(p)/t^2$ takes place in the case of a constant shock velocity V_s. This roughly corresponds to an exact solution, in which the shock expands with a slight deceleration.

In Fig. 3a, the piston and shock sizes and velocities are plotted against time. If the gas distribution in the $R_p < r < R_s$ region between the piston and the shock front is assumed to be uniform, then it follows from the condition for mass conservation of the matter swept up by the shock that $R_s - R_p \approx R_s/\sigma$. Because of the large compression ratio $\sigma \approx 12$ (Fig. 3b), the shock radius R_s exceeds the piston radius R_p by a mere 8%. We also see from the figure that the piston and shock expansion velocities are nearly constant during the initial period $t < 100$ days. This can be explained by the fact that the piston mass M_p to which the mass of the matter swept up by the shock,

$$M_{sw} = 4\pi \int_0^{R_s} drr^2\rho_0(r),\tag{33}$$

becomes equal only at $t \approx 100$ days corresponds to the assumed initial piston expansion velocity V_{pi}. Before this time, $M_{sw} < M_p$, and the piston deceleration is insignificant. Since the number of accelerated particles $N_e \propto f_s V$ is proportional to the current ambient density ($f_s \propto \rho_s$) and to the volume occupied by the accelerated particles ($V \propto R_s^3$), the expected time dependence of the radio flux is $S \propto f_s V B_s^{(\gamma+1)/2} \propto R_s^{-(\gamma-1)/2}$, where $\gamma = q_s -2$. In the initial period, this yields $S \propto t^{-1}$.

At $t > 100$ days, $R_s \propto t^{\frac{k-3}{k-2}} = t^{0.85}$, which gives $S \propto t^{-0.85}$. The decrease in ambient density and magnetic-field strength as the shock expands in the supersonic-wind zone ($r < R_T$) is mainly responsible for the rapid decline in radio flux with time.

Figure 3d shows the overall spectrum of the CRs,

$$N(p, t) = 16\pi^2\int_0^\infty drr^2 f(r, p, t),\tag{34}$$

accelerated by time t. The spectral shape reflects all the preceding stages of CR evolution and acceleration. The low-energy part of the spectrum is soft, $N \propto p^{-3}$, reflecting the form of the distribution function $f_s \propto p^{-5}$ reproduced at the shock front at each time.

The high-energy part of the overall spectrum ($p > 10^2 mc$) is very hard, $N \propto p^{-1.4}$, up to the maximum momentum $p_m \sim 10^5 mc$. Interestingly, the overall spectrum at high energies is harder that the particle spectrum at the shock front $n_s = 4\pi p^2 f_s(p) \propto p^{-1.6}$. The reason is that, at $r > R_s$, the accelerated CRs occupy a region whose thickness $l = \kappa(p)/u_0$ is an increasing function of momentum (here, $u_0 = V_s - w_0(R_s) - c_a(R_s)$). In the period under consideration, when the downstream region is very thin, $R_s - R_p \approx 0.08R_s$, the contribution of the $r > R_s$ region to the overall spectrum $N(p)$ becomes significant at large momenta, which makes the spectrum $N(p)$ harder than $n_s(p)$.

In the course of time, the overall CR spectrum grows in proportion with the mass of the swept-up matter, $N \propto M_{sw} \propto R_s$. Figure 3e shows our calculations of the integrated gamma-ray flux density (the number of gamma-ray photons with energy above ϵ_γ per cm^2 per second) from the decay of π^0 mesons produced in nuclear collisions of CR protons with ambient atoms (p–p collisions) calculated by using the formula (Drury et al. 1994)

$$F_\gamma(\epsilon_\gamma) = Q_\gamma(\epsilon_\gamma)/4\pi d^2,\tag{35}$$

where

$$Q_\gamma(\epsilon_\gamma) = 4\pi\int_0^\infty drr^2\int_{\epsilon_\gamma}^\infty d\epsilon_\gamma q_\gamma^{pp}(\epsilon_\gamma)\tag{36}$$

is the total integrated gamma-ray flux from the SNR,

$$q_\gamma^{pp}(\epsilon_\gamma) = \sigma_{pp}Z_\gamma cN_g n(r, \epsilon_\gamma, t)\tag{37}$$

is the production rate of gamma-ray photons with energy ϵ_γ per unit volume of the SNR with proton

number density $N_g = \rho/m$,

$$\sigma_{pp} = 38.5 + 0.46\ln^2\frac{0.01876p}{mc} \text{ mb} \qquad (38)$$

is the total cross section for p–p collisions (Berezinskii $et\ al.$ 1990), Z_γ is the so-called spectrum-weighted moment of the cross section for the production of π^0 mesons in p–p collisions averaged over the CR proton power-law spectrum, $n(r, \epsilon_k, t) = 4\pi p\epsilon f(r, p, t)/c^2$ is the differential (in kinetic energy ϵ_k) CR proton number density, and $\epsilon = \sqrt{p^2c^2 + m^2c^4} = \epsilon_k + mc^2$ is the total CR proton energy. For the moment Z_γ, we use the fits (Drury $et\ al.$ 1994; Berezhko and Völk 1997, 1999)

$$Z_\gamma = \min\{0.2, 10^{1.49 - 2.73(\gamma - 1) + 0.53(\gamma - 1)^2}\}, \qquad (39)$$

where $\gamma = -d\ln n/d\ln\epsilon_k$ is the local CR spectral index.

The very hard spectrum—$F_\gamma \propto \epsilon_\gamma^{-\alpha}$, $\alpha \ll 1$, at $\epsilon_\gamma <$ 10 TeV—stems from the fact that it is dominated by the contribution of the CR interaction with the ejecta. In this case, the degree of CR penetration through the piston grows with energy, which ensures that the gamma-ray emission produced in the envelope is hard. The time dependence of the gamma-ray flux, $F_\gamma \propto M_{ej}e_c$, is determined by the decrease in CR energy density with time, $e_c \propto \rho_s V_s^2 \propto 1/t^2$ at $r \le R_p$ [see Berezhko and Völk (1999) for more detail]. Allowance for CR penetration into the envelope and nonlinear effects determine a more efficient production of gamma-ray emission with a considerably harder spectrum than do the linear approximation considered for SNR 1987A by Berizinsky and Ptuskin (1988).

One should allow for the fact that the absorption of gamma-ray photons in the ejecta due to their interaction with atomic nuclei and optical photons must be taken into account at the early stage of evolution $t <$ 100 days, when the calculated fluxes are particularly large. This issue was addressed fairly completely by Berezinsky $et\ al.$ (1990). As for the later period $t \simeq$ 300 days, the upper limits on TeV gamma-ray fluxes from SNR 1987A obtained in several experiments (see Berezinsky $et\ al.$ 1990) are consistent with our calculations (see Fig. 3e).

Figure 3f presents the various energy components of the system: the ejecta energy

$$E_p = M_pV_p^2/2 + 2\pi mt^3\int_0^{R_p/t} dv\,v^4\rho_{ej}(v, t), \qquad (40)$$

the kinetic and thermal energies transferred to the gas

$$E_k = 2\pi\int_{R_p}^\infty dr\,r^2\rho w^2, \qquad (41)$$

$$E_g = 6\pi\int_{R_p}^\infty dr\,r^2[P_g(r, t) - P_{g0}(r)], \qquad (42)$$

and the CR energy

$$E_c = 16\pi^2 mc^2\int_0^\infty dr\,r^2$$
$$\times \int_0^\infty dp\,p^2(\sqrt{(p/mc)^2 + 1} - 1)f(r, p, t). \qquad (43)$$

It shows that ~10^{-4} of the energy released during the explosion is converted into CRs in a mere thousand days of evolution, suggesting a very high efficiency of the CR acceleration at the early stage of SNR evolution.

The radio flux from SNR 1987A again began to rise rather rapidly starting from $t \approx 1100$ days (see Fig. 4). This fact can be explained most naturally by assuming that the shock reaches zone II of thermalized stellar wind ($r > R_T$) at $t \approx 1100$ days (Chevalier 1992). In this case, the piston velocity is $V_p = 27\,728$ km s^{-1}, which we use as the initial velocity V_{pi} when solving the problem of shock propagation in the $r > R_T$ zone. Given that $R_s = R_T = 3.1 \times 10^{17}$ cm at this time, relations (21)–(23) yield the initial values of ambient proton number density $N_{g0} = \rho_a/m = 0.21$ cm^{-3}, internal gas pressure $P_{g0} = 1.3 \times 10^{-10}$ dyne cm^{-2}, and magnetic field $B_{02} = B_{II} = 76$ μG. In zone III, we take B_{III} to be 38 μG. The results of our calculations for shock propagation in zones II and III ($r > R_T$) are presented in Figs. 4 and 5.

In Fig. 4, the radio fluxes S are plotted against time for four frequencies for which measurements are available (Gaensler $et\ al.$ 1997). As we see from the figure, the theory satisfactorily reproduces the measurements. The rise in radio flux from the SNR after the shock reaches the compressed-wind region is attributable to an increase in the magnetic field and ambient density at $r > R_T$. During the initial period, the shock expands in a nearly homogeneous region as $R_s \propto t^{\frac{k-3}{k}}$. Therefore, the expected rise in radio flux must follow a law $S \propto \rho_s R_s^3 V_s^2 \propto t^{1.26}$, in agreement with experiment.

As we see from Fig. 5a, agreement of the calculated time dependences of shock radius R_s and velocity V_s with experiment (Gaensler $et\ al.$ 1997, 1999) is achieved at $R_C = 5 \times 10^{17}$ cm and the red-supergiant wind number density (zone III, $r > R_C$) $N_{g0} = \rho_{III}/m = 420$ cm^{-3}, which is a factor of 3 larger than the estimates from Chevalier and Dwarkadas (1995). According to Fig. 5a, it is at these values of R_C and ρ_{III} that the shock decelerates from $V_s \approx 30000$ to 3000 km s^{-1} within 1500–2500 days after expansion onset. Note that the difference between the calculated and measured shock velocities V_s at $t = 1500$ days is slightly smaller than that shown in Fig. 5, considering that the measured $V_s = 34600$ km s^{-1} has the meaning of average $\bar{V}_s = R_s/t$. Since the shock expanded with deceleration over the

entire preceding period, the average velocity (at $t = 1500$ days, our calculation yields $\bar{V}_s = 30091$ km s^{-1}) is larger than its current value.

A probable reason for the disagreement with the results of Chevalier and Dwarkadas (1995) is as follows. As we see from Fig. 5a, the shock velocity rapidly falls off starting from $t \approx 1800$ days, because it enters the region of abrupt increase in ambient density. In this case, it becomes even lower than the velocity of the piston ($V_s < V_p$), which also decelerates but not so rapidly. Therefore, the shock velocity is slightly recovered through the piston effect. As the shock decelerates, the periods with $V_s > V_p$ and $V_s < V_p$ alternate several times. The reason is that, when the piston abruptly decelerates, its velocity drops below the velocity of freely expanding elements in the ejecta. As these most rapid elements catch up with the piston and impart an additional momentum to it, its velocity again slightly increases. It is for this reason, according to Fig. 5a, that the ejecta and the shock at $t > 3000$ days expand with some acceleration.

The ten-fold decrease in shock velocity during 1500–2500 days is accompanied by a hundred-fold reduction in injected-particle energy $\epsilon_{inj} \propto V_s^2$. According to relations (18) and (22), this causes the constant K_{ep}, which determines the ratio of the accelerated electrons and protons at relativistic energies, to decrease from $K_{ep} = 0.015$ at the beginning of zone II to $K_{ep} = 0.01$ in zone III. As we see from Fig. 4, this allows satisfactory agreement to be reached between theory and experiment for the entire period $t > 1100$ days.

As in the supersonic-wind zone ($r < R_T$), the supernova shock is strongly modified. In the initial period, the total compression ratio is $\sigma \approx 9.5$ (see Fig. 5b). The shock deceleration is accompanied by a reduction in the Mach number and causes the compression ratio σ to decrease significantly with time. Although the shock velocity continues to drop at $t > 1700$ days, its Mach number, both the sonic ($M_S = V_s/c_S$) and Alfven ($M_a = V_s/c_a$) ones, increases because of the more rapid reduction in the speed of sound $c_S \propto 1/\sqrt{\rho_s}$ and Alfven velocity $c_a \propto B/\sqrt{\rho_s}$ in the medium. This results in a growth of the shock modification: the Alfven velocity at $r > R_T$ decreases by approximately a factor of 100, which, given the ten-fold drop in V_s, is accompanied by an increase in M_a by a factor of 10 and an increase in the total compression ratio to $\sigma \approx 20$ (see Fig. 5b) at $t > 4000$ days, in good agreement with the expected dependence $\sigma \approx 1.5 M_a^{3/8}$ (Berezhko et al. 1996; Berezhko and Ellison 1999). As in the $r < R_T$ zone, the shock does not become completely modified, and the subshock does not disappear, which is the result of a crucial role of geometric effects.
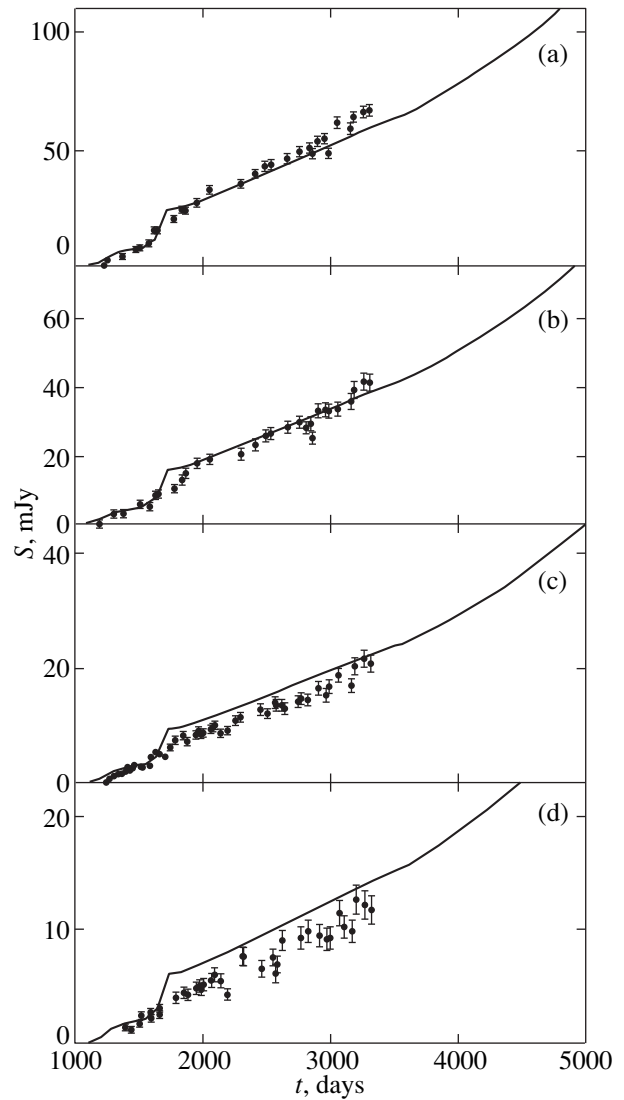
Fig. 4. The radio flux from SNR 1987A for four frequencies $\nu = 1.4$ (a), 2.4 (b), 4.8 (c), and 8.4 (d) GHz versus time measured from the supernova explosion. Experimental values were taken from Gaensler et al. (1997).

The subshock compression ratio is $\sigma_s \approx 3$ and varies only slightly in the course of evolution (see Fig. 5b). Therefore, as in the $r < R_T$ zone, the CR spectrum in the range $p_{inj} \leq p < 10mc$, which includes the energy range $\epsilon_e = 1$–10 GeV of the electrons emitting at $\nu = 1$–10 GHz, has the shape $f_s \propto p^{-q}$ with $q = q_s \approx 4.6$ (see Fig. 5b). This corresponds to the index of the energy spectrum $\gamma = q - 2 \approx 2.6$ and to the index of the frequency radio spectrum $\alpha \approx 0.85$, which is in good agreement with experiment. At the same time, the high-energy part of the CR spectrum is very hard, $f \propto p^{-3.5}$, which is attributable to the large compression ratio σ.

Since, according to relation (30), $p_m \propto R_s V_s$, the maximum accelerated-particle momentum p_m decreased from
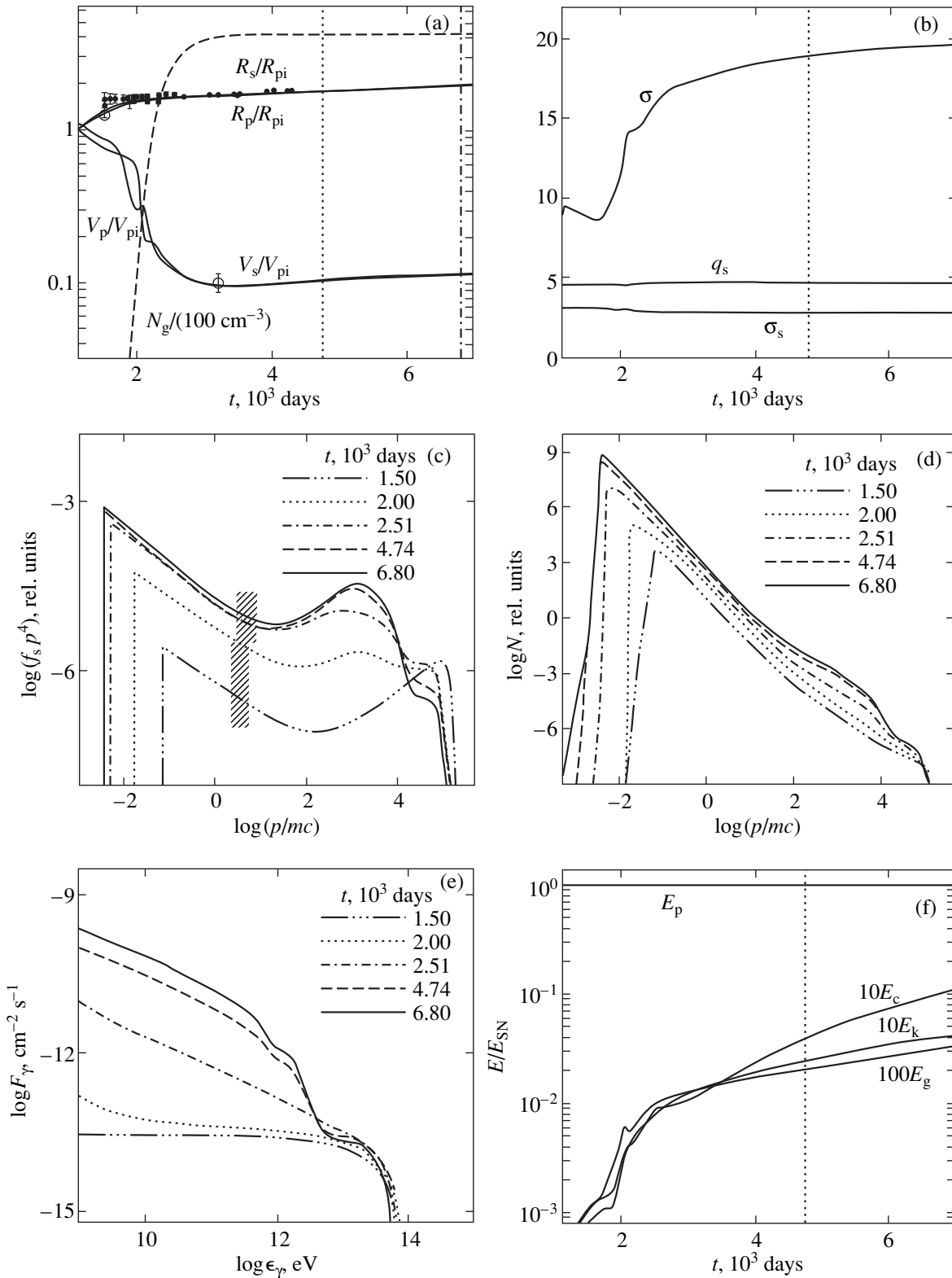
Fig. 5. Same as Fig. 2 for the period when the shock propagates in the $r > R_T$ region. The initial piston size and velocity are $R_{pi} = 3.1 \times 10^{17}$ cm and $V_{pi} = 27728$ km s^{-1}, respectively. The vertical line, indicated by dots in Figs. 4a, 4b, and 4e, corresponds to the current epoch of evolution; the vertical dot–dashed line in Fig. 4a corresponds to the time when the shock reached the ring-shaped clump ($r = R_R$). The experimental shock size (filled circles) and velocity (open circles) in Fig. 4a were taken from Gaensler *et al.* (1997, 1999).

$p_m \sim 10^5 mc$ at $t < 1500$ days to $p_m \sim 10^4 mc$ at $t > 2500$ days because of the shock deceleration. The particles with momenta $10^4 < p/mc < 10^5$ at $t > 2500$ cease to be accelerated by the shock because of its low velocity during this period. The increase in the volume occupied by them follows a diffusion law, causing the distribution function $f_s \propto t^{-3/2}$ to decrease.

Figure 5d shows the overall spectrum $N(p, t)$ of the CRs accelerated by the corresponding time $t > t_i = 1100$ days. The spectral shape reflects the preceding stages of CR evolution and acceleration. During the initial evolution $t/t_i < 3$, the high-energy part $(p > 10^2 mc)$ of the overall spectrum is very hard, $N \propto p^{-1.5}$, up to the maximum momentum $p_m \approx 10^5 mc$. The spectral shape becomes more complex with time. The overall spectrum $N(p)$ ceases to grow at large momenta $p > 10^4 mc$, because the acceleration here becomes inefficient at $t > 2500$ days. At smaller momenta $p < 10^4 mc$, the overall spectrum continues to monotonically grow, with the portion of the hardest spectrum $N \propto p^{-1.5}$ being formed at $10 < p/mc < 10^4$. The low-energy part of the spectrum is much softer, $N \propto p^{-2.7}$.

Note that the distribution function $f_s(p)$ and the overall CR spectrum $N(p)$ are presented in Figs. 5c and 5d in the same relative units as those in Figs. 3c and 3d, respectively. Therefore, a direct comparison of Figs. 3d and 5d shows that, already by $t = 1500$ days, the spectrum of the CRs accelerated in the $r > R_T$ zone is considerably higher than the spectrum $N(t = 1000$ days, $p)$ formed over the entire period of the shock passage through the $r < R_T$ zone. The latter serves as a justification for disregarding the CR particles produced in the $r < R_T$ zone when describing the shock evolution at $r > R_T$.

Figure 5e presents the results of our calculations of the expected integrated gamma-ray spectrum for five times. During the initial period $t < 2000$ days, the spectrum $F_\gamma(\epsilon_\gamma)$ is dominated by the gamma-ray photons produced by the CR interaction with the ejecta, especially at high energies. Therefore, the gamma-ray spectrum at $1 < t/t_i < 2$ is as hard as that during the preceding period of the shock propagation at $r < R_T$. As the shock expands, the mass of the swept-up matter M_{sw} grows; as a result, the spectrum $F_\gamma(\epsilon_\gamma)$ is dominated by the gamma-ray photons produced in the matter swept up by the shock at $t > 2000$ days. For this reason, the gamma-ray spectrum at late stages is considerably softer than that during the initial period $t < 2000$ days. Note that the total gas mass at $r < R_R$, $M \approx 0.3 M_\odot$, is significantly smaller than the ejecta mass, $M_{ej} = 10 M_\odot$. The dominance of gamma-ray emission from the $R_p < r < R_s$ region stems from the fact that the CR number density at $r < R_p$ is lower than that at $R_p < r < R_s$ by more than a factor of 100.

The pattern of evolution of the gamma-ray spectrum at $t > 2500$ days can be understood by taking into account the following circumstances. Gamma-ray photons with energy $\epsilon_\gamma < 3$ TeV are produced by CR particles with energy $\epsilon < 30$ TeV, which continue to be effectively accelerated by the shock; therefore, the expected flux $F_\gamma \propto M_{sw} e_c$ is proportional to the CR energy density at $R_p < r < R_s$, where the swept-up matter of mass M_{sw} is concentrated. Since the shock velocity is approximately constant at $t > 2000$ days, the CR energy density $e_c \propto \rho_s V_s^2$ does not vary, while the swept-up mass grows as $M_{sw} \propto R_s^3 \propto t^3$. This causes an increase in the expected flux $F_\gamma \propto t^3$ with time until late 2006, when the shock will reach the beginning of the ring-shaped clump at $r = R_R = 6 \times 10^{17}$ cm (McCray 1993). Note that the calculated time when the shock reaches the $r = R_R$ boundary is in agreement with the estimates by Chevalier and Dwarkadas (1995) and Gaensler $et\ al.$ (1997).

The most energetic gamma-ray photons $(\epsilon_\gamma > 3$ TeV) are produced by CRs with $\epsilon > 30$ TeV, which are barely affected by the shock at $t > 3000$ days. At the same time, these particles are distributed almost uniformly over the entire $r < R_s$ region. Therefore, gamma rays with energy $\epsilon_\gamma > 3$ TeV originate predominantly in the ejecta and their flux $F_\gamma \propto M_{ej} e_c \propto t^{-3/2}$ decreases with time.

As we see from Fig. 5e, the TeV gamma-ray flux at the current stage of evolution is $F_\gamma \approx 7 \times 10^{-13}$ cm^{-2} s^{-1}, and it is expected to almost double by 2006. The expected gamma-ray spectrum steepens precisely at $\epsilon_\gamma \sim 1$ TeV, implying that the flux $F_\gamma(1$ TeV) is very sensitive to the parameters determining the maximum CR energy. Thus, in particular, if the actual magnetic field at $r > R_T$ is slightly weaker that we assumed, or if the actual CR diffusion coefficient is larger than the Bohm one, this can result in a decrease of the maximum CR energy by more than a factor of 2, which, in turn, will cause the flux $F_\gamma(1$ TeV) to decrease at least by an order of magnitude (see Fig. 5e). In this situation, energies $\epsilon_\gamma \sim 0.1$ TeV are preferred for detecting the gamma rays from SNR 1987A generated by the CR nucleon component.

High-energy gamma rays are also generated by the CR electron component during Compton backward scattering by cosmic microwave background photons. The specific production rate of gamma-ray photons corresponding to this process is given by (Berezinsky $et\ al.$ 1990)

$$q_\gamma^{IC}(\epsilon_\gamma) = \sigma_T c N_{ph} n_e(\epsilon_e)(d\epsilon_e/d\epsilon_\gamma), \qquad (44)$$

where $\sigma_T = 6.65 \times 10^{-25}$ cm^2 is the Thomson cross section; $\epsilon_e = m_e c^2 \sqrt{3\epsilon_\gamma/(4\epsilon_{ph})}$ is the energy of the electrons producing gamma-ray photons with energy ϵ_γ during scattering; $\epsilon_{ph} = 6.7 \times 10^{-4}$ eV and $N_{ph} = 400$ cm^{-3} are the mean energy and number density of cosmic microwave background photons. If, for simplicity, we take $\sigma_{pp} = 40$ mb in (35) and a purely power-law spectrum

of the accelerated CRs, $n(\epsilon_k) \propto \epsilon_k^{-\gamma}$, then the ratio of the specific production rates of the gamma rays generated by the electron and nucleon components is given by

$$\frac{q_\gamma^{IC}}{q_\gamma^{pp}} = 1.8 \times 10^4 \frac{K_{ep}}{N_g}\left(\frac{\epsilon_\gamma}{290\ \text{TeV}}\right)^{(\gamma-1)/2}. \qquad (45)$$

Given that, in our case, $K_{ep} \approx 0.01$, $N_g \approx \sigma N_{g0} \sim 10^4$ cm^{-3}, and $\gamma \approx 1.6$, it thus follows that $q_\gamma^{IC} \ll q_\gamma^{pp}$; i.e., the contribution of the electron component to the generation of gamma rays with energy $\epsilon_\gamma \lesssim \leq 1$ TeV is small compared to that of the nucleon component.

Figures 5f, where the various energy components of the system are presented, shows that about one percent of the explosion energy is converted into CRs in less than three decades of evolution. This suggests a very high efficiency of the CR acceleration at the early stage of SNR evolution. The latter is ensured by the high ejecta expansion velocity at the early stage and by the relatively high ambient density.

Note that, for a number of reasons, any detailed comparison of our results with those of Duffy *et al.* (1995) does not seem possible. The set of physical parameters taken by Duffy *et al.* (1995) differs markedly from our set. One reason is that the dynamics of the expanding shock was not calculated by the above authors in a self-consistent way: instead, these authors assumed the shock velocity to be constant ($V_s = 22\,000$ km s^{-1}), which is at variance with the requirements of the experiment whose results are presented in Fig. 5a.

CONCLUSION

Our calculations have shown that the observed properties of the radio emission from SNR 1987A can be satisfactorily explained on the basis of views about regular acceleration of the CR nucleon and electron components by the supernova shock propagating through the progenitor stellar wind. In this case, the nonlinear kinetic theory developed for an inhomogeneous ISM (Berezhko and Völk 2000) predicts a high efficiency of CR acceleration and a large degree of shock modification by the inverse effect of CR pressure on the shock. The available set of experimental data leads us to a definitive conclusion about the physical parameters of SNR 1987A.

The relatively low rate of mass loss by the blue-supergiant progenitor of SN 1987A, $\dot{M} = 7.5 \times 10^{-8} M_\odot$ yr^{-1}, is limited by the requirement that follows from experiment (Gaensler *et al.* 1997): the mean shock expansion velocity within the first 1500 days after the explosion must be $V_s \approx 30000$ km s^{-1}. A higher $\dot{M}$ results in a stronger deceleration in the blue-supergiant supersonic-wind zone, which is inconsistent with experiment.

The rate of proton injection into the acceleration directly affects the degree of shock modification, which is characterized by the subshock compression ratio (σ_s) and the entire shock transition (σ). The observed, relatively soft radio spectrum of SNR 1987A, $S \propto \nu^{-\alpha}$, $\alpha \approx 0.9$ (Turtle *et al.* 1987; Staveley-Smith *et al.* 1992; Gaensler *et al.* 1997), is produced by synchrotron radiation of relativistic electrons with a power-law spectrum $f \propto p^{-q}$, $q \approx 4.8$, which is naturally reproduced by a modified shock with a subshock compression ratio $\sigma_s \approx 3$. Such a degree of modification is reached when the fraction $\eta = 10^{-2}$ of protons of the medium swept up by the shock are drawn (injected) into the acceleration. This value of the required injection rate is consistent with interplanetary measurements (see, e.g., Trattner *et al.* 1994) and with numerical simulations of collisionless shocks (Quest 1988; Trattner and Scholer 1993). Note that, although there is no direct experimental evidence for the effective acceleration of the CR nucleon component in SN 1987A, the need for a substantial shock modification can be considered as circumstantial evidence that the CR nucleon component is actually accelerated.

As for the rate of electron injection into the acceleration, we suggest that it is closely related to the proton injection rate at which the number of accelerated electrons at relativistic energies $\epsilon_k \gg mc^2$ accounts for 0.01 of the number of protons. In this case, we proceed from the observed electron-to-proton ratio in Galactic CRs, although such a consideration cannot be regarded as a strict justification of the above number.

Apart from the above two parameters $\dot{M}$ and η, the magnetic field directly affects the radio flux. Agreement with the measured flux over the first twelve days is achieved at the blue-supergiant surface field strength $B_* = 59$ G, which is typical of this class of stars.

The detected rise in the radio flux from SNR 1987A at phase $t \approx 1200$ days (Staveley-Smith 1992; Gaensler *et al.* 1997) is naturally associated with the time when the blast wave reaches zone II of the thermalized stellar wind at $r > R_T$. The abrupt increase in the ambient density and magnetic field at the termination shock ($r = R_T$), which separates this zone I from the supersonic-wind zone II, causes a rise in the radio flux. Our calculations yield $R_T = 3.1 \times 10^{15}$ cm for the size of the termination shock.

The experimentally observed significant shock deceleration at phase $t = 1500$–3000 days, during which the shock velocity dropped from 30 000 to 3000 km s^{-1} as inferred from measurements of the dynamics of the radio image for SNR 1987A (Gaensler *et al.* 1997), is reproduced in our calculations by the third, denser zone III occupied by the red-supergiant wind matter with the number density $N_g = 420$ cm^{-3} located at $r > 5 \times 10^{17}$ cm. The theory ensures reasonable agreement of the properties of radio emission from SNR 1987A with experi-

ment at the magnetic-field strengths $B = 76$ and 38 μG in zones II and III, respectively.

Since the shock at the current evolutionary phase propagates in a fairly dense medium and effectively accelerates CRs up to energies ~10 TeV, the total gamma-ray flux generated by the CR nucleon component in collisions with ambient nuclei at energies $\epsilon_\gamma \lesssim 1$ TeV is $F_\gamma = 7 \times 10^{-13} (\epsilon_\gamma/1 \text{ TeV})^{-0.6} \text{ cm}^{-2} \text{ s}^{-1}$; its monotonic rise is expected at least until 2006, when the flux will approximately double. It should be emphasized that the available experimental data impose no significant constraints on the maximum energy of the accelerated CRs $\epsilon_{max} = p_m c$. The shock parameters, the CR spectrum at moderate energies $p \ll p_m$, and, consequently, the properties of SNR radio emission depend only slightly on p_m (Berezhko and Ellison 1999). A change in p_m even by an order of magnitude compared to the value calculated above, which can be caused by a deviation of the diffusion coefficient from the Bohm limit, will not make any significant changes in the achieved agreement between theory and experiment. Of particular importance are therefore measurements of the high-energy ($\epsilon_\gamma \gtrsim 100$ GeV) gamma-ray flux, which can provide direct information about the maximum CR energy ϵ_{max}. It is important to note that, at energies $\epsilon_\gamma = 0.1$–1 TeV, the modern stereoscopic systems of gamma-ray telescopes are sensitive enough to detect the expected gamma-ray emission from SNR 1987A (see Aharonian *et al.* 1997).

ACKNOWLEDGMENTS

REFERENCES

1. F. A. Aharonian, W. Hofmann, A. K. Konopelko, and H. J. Völk, Astropart. Phys. **6**, 369 (1997).

2. W. I. Axford, E. Leer, and G. Skadron, in *Proceedings of the 15th International Cosmic Ray Conference, 1977*, Vol. 11, p. 132.

3. L. Ball and J. G. Kirk, Astrophys. J. Lett. **396**, L39 (1992).

4. A. R. Bell, Mon. Not. R. Astron. Soc. **182**, 147 (1978); **182**, 443 (1978a).

5. A. R. Bell, Mon. Not. R. Astron. Soc. **182**, 443 (1978b).

6. E. G. Berezhko, Pis'ma Astron. Zh. **12**, 842 (1986) [Sov. Astron. Lett. **12**, 352 (1986)].

7. E. G. Berezhko, Astropart. Phys. **5**, 367 (1996).

8. E. G. Berezhko and D. C. Ellison, Astrophys. J. **526**, 385 (1999).

9. E. G. Berezhko and G. F. Krymsky, Usp. Fiz. Nauk **154**, 49 (1988) [Sov. Phys. Usp. **31**, 27 (1988)].

10. E. G. Berezhko and L. T. Ksenofontov, Zh. Éksp. Teor. Fiz. **116**, 737 (1999) [JETP **89**, 391 (1999)].

11. E. G. Berezhko and H. J. Völk, Astropart. Phys. **7**, 183 (1997).

12. E. G. Berezhko and H. J. Völk, in *Proceedings of the 26th International Cosmic Ray Conference, 1999*, Vol. 4, p. 435; Astron. Astrophys. **357**, 283 (2000).

13. E. G. Berezhko, V. K. Elshin, G. F. Krymsky, and S. I. Petukhov, *Cosmic-Ray Generation by Shock Waves* (Nauka, Novosibirsk, 1988).

14. E. G. Berezhko, V. K. Yelshin, and L. T. Ksenofontov, Astropart. Phys. **2**, 215 (1994).

15. E. G. Berezhko, L. T. Ksenofontov, and V. K. Yelshin, Nucl. Phys. B (Proc. Suppl.) **39A**, 171 (1995).

16. E. G. Berezhko, V. K. Elshin, and L. T. Ksenofontov, Zh. Éksp. Teor. Fiz. **109**, 3 (1996) [JETP **82**, 1 (1996)].

17. E. G. Berezhko, L. T. Ksenofontov, and S. I. Petukhov, in *Proceedings of the 26th International Cosmic Ray Conference, 1999*, Vol. 4, p. 431.

18. V. S. Berezinsky and V. S. Ptuskin, Pis'ma Astron. Zh. **14**, 713 (1988) [Sov. Astron. Lett. **14**, 304 (1988)].

19. V. S. Berezinsky, S. V. Bulanov, V. L. Ginzburg, *et al.*, *Astrophysics of Cosmic Rays* (Nauka, Moscow, 1990).

20. A. M. Bykov and Yu. A. Uvarov, Zh. Éksp. Teor. Fiz. **115**, 846 (1999) [JETP **88**, 465 (1999)].

21. R. A. Chevalier, Astrophys. J. **259**, 302 (1982).

22. R. A. Chevalier, Nature **360**, 628 (1992).

23. R. A. Chevalier and V. V. Dwarkadas, Astrophys. J. Lett. **452**, L45 (1995).

24. R. A. Chevalier and C. Fransson, Nature **328**, 44 (1987).

25. E. A. Dorfi, Astron. Astrophys. **251**, 597 (1991).

26. L. O'C. Drury, Rep. Prog. Phys. **46**, 973 (1983).

27. L. O'C. Drury, Adv. Space Res. **4**, 185 (1984).

28. L. O'C. Drury, W. Markiewcz, and H. J. Völk, Astron. Astrophys. **225**, 179 (1989).

29. L. O'C. Drury, F. A. Aharonian, and H. J. Völk, Astron. Astrophys. **287**, 959 (1994).

30. L. O'C. Drury, H. J. Völk, and E. G. Berezhko, Astron. Astrophys. **299**, 222 (1995).

31. P. Duffy, L. Ball, and J. G. Kirk, Astrophys. J. **447**, 364 (1995).

32. D. C. Ellison, F. C. Jones, and D. Eichler, J. Geophys. **50**, 110 (1981).

33. B. M. Gaensler, R. N. Manchester, L. Staveley-Smith, *et al.*, Astrophys. J. **479**, 845 (1997).

34. B. M. Gaensler *et al.*, private communication (1999).

35. E. M. Jones, B. W. Smith, and W. C. Starka, Astrophys. J. **249**, 185 (1981).

36. J. G. Kirk, P. Duffy, and L. Ball, Astron. Astrophys. **293**, L37 (1995).

37. G. F. Krymsky, Geomagn. Aéron. **4**, 977 (1964).

38. G. F. Krymsky, Dokl. Akad. Nauk SSSR **234**, 1306 (1977) [Sov. Phys. Dokl. **22**, 327 (1977)].

39. P. O. Lagage and C. J. Gesarsky, Astron. Astrophys. **125**, 249 (1983).

40. M. A. Lee, J. Geophys. Res. **87**, 5063 (1982).

41. A. Levinson, Astrophys. J. **401**, 73 (1992).

42. A. Levinson, Astrophys. J. **426**, 327 (1994).

43. A. Levinson, Mon. Not. R. Astron. Soc. **278**, 1018 (1996).

44. M. A. Malkov and H. J. Völk, Astron. Astrophys. **300**, 605 (1995).

45. R. Mc Cray, Annu. Rev. Astron. Astrophys. **31**, 175 (1993).

46. J. F. McKenzie and H. J. Völk, Astron. Astrophys. **116**, 191 (1984).

47. E. N. Parker, Planet. Space Sci. **13**, 9 (1965).

48. K. B. Quest, J. Geophys. Res. **93**, 9649 (1988).

49. L. Staveley-Smith, R. N. Manchester, M. G. Kestenev, *et al.*, Nature **355**, 147 (1992).

50. M. C. Storey and R. N. Manchester, Nature **329**, 421 (1987).

51. T. Terasawa, K. Maezawa, M. Moshino, *et al.*, in *Proceedings of the 26th International Cosmic Ray Conference, 1999,* Vol. 6, p. 528.

52. K. J. Trattner and M. Scholer, Ann. Geophys. **9**, 774 (1993).

53. K. J. Trattner, E. Möbius, M. Scholer, *et al.*, J. Geophys. Res. **99**, 389 (1994).

54. A. J. Turtle, D. Campbell-Wilson, J. D. Bunton, *et al.*, Nature **327**, 38 (1987).

55. H. J. Völk, L. A. Zank, and G. P. Zank, Astron. Astrophys. **188**, 274 (1988).

Translated by V. Astakhov

The Praesepe Open Cluster and the Galactic Distance Scale

A. V. Loktin*

Astronomical Observatory, Ural State University, pr. Lenina 51, Yekaterinburg, 620083 Russia
Received January 13, 1999; in final form, March 14, 2000

Abstract—Updated proper motions for 328 probable members of the Praesepe are used to determine the distance to this open cluster by Hertzsprung's geometric method. The cluster distance was found to be $r = 171 \pm 15$ pc, which corresponds to the distance modulus $V_0 - M_V = 6\overset{m}{.}16 \pm 0.19$. The distance scale for open clusters is discussed. © *2000 MAIK "Nauka/Interperiodica".*

Keywords: *star clusters and associations, stellar dynamics*

INTRODUCTION

Recent Hipparcos determinations of stellar trigonometric parallaxes have cast doubt on the reliability of the methods used to estimate the distances to open star clusters.

Mermilliod *et al.* (1997) and Robichon *et al.* (1997) determined the distances to thirteen nearby open clusters by using trigonometric parallaxes. They inferred a possible inadequacy of the method of estimating distance moduli by fitting photometric diagrams as a probable source of discrepancies between the distance estimates obtained from Hipparcos trigonometric and photometric parallaxes. This inference calls into question the numerous distance determinations for open clusters and other Galactic objects. New, independent estimates of the distance moduli for open clusters are therefore required.

## DISTANCE MODULI FOR OPEN CLUSTERS

Table 1 compares the distance moduli for nearby clusters estimated from trigonometric parallaxes and by diagram fitting. Its columns give the following: (1) cluster names; (2) distance moduli deduced by Mermilliod *et al.* (1997) and Robichon *et al.* (1997) from trigonometric parallaxes; (3) rms errors of the distance moduli from the above papers; (4) distance moduli from the catalog by Lynga (1987); (5) and (6) distance moduli from a new version of the catalog of cluster parameters by Loktin *et al.* (1997); and (7) values from our catalog shifted by $0\overset{m}{.}43$ to correct for a systematic difference between the distance scales in the two series of estimates. The table provides no data for the Stock2 and Blanco1 clusters included in the lists of Mermilliod

et al. (1997) and Robichon *et al.* (1997), for which no data are available in our catalog. As we see from the table, the distance modulus for only one cluster (IC 4756) deviates appreciably from good agreement (given the above errors) between the estimates obtained from trigonometric parallaxes and the estimates of our catalog. Given the systematic difference between the two scales, the rms difference between the estimates is $0\overset{m}{.}20$. This value is smaller than the mean error of the distance moduli determined from trigonometric parallaxes (see the table), so the discrepancies in the estimates can all be attributed to random errors. Only the cluster IC 4756 requires a separate study.

THE PRAESEPE CLUSTER AND THE GEOMETRIC METHOD

To solve the problem of whether the photometric method is applicable requires an independent distance determination at least for several nearby clusters. Distances can be estimated by the geometric method. Until now, the geometric method of distance determination has been applied to the Hyades alone [with the exception of one unsuccessful attempt outlined by Loktin and Matkin (1988)]. However, a continuous increase in the amount of astrometric data and an improvement in their quality give hope that the applicability of the trigonometric method will be extended to other nearby open clusters as well. Using data on 189 stars, which are probable members of the Praesepe, Loktin and Matkin (1988) estimated the distance to this cluster to be $r = 175 \pm 43$ pc with a mean proper-motion error of $0\overset{''}{.}2/100$ yr. As new observations of Praesepe stars have appeared in the literature since the publication of the above paper, we have decided to repeat an attempt to determine the distance to this cluster by the geometric method. We took our catalog prepared for the study (Loktin and Matkin 1988) as the main new catalog of

* E-mail address for contacts: Alexander.Loktin@usu.ru
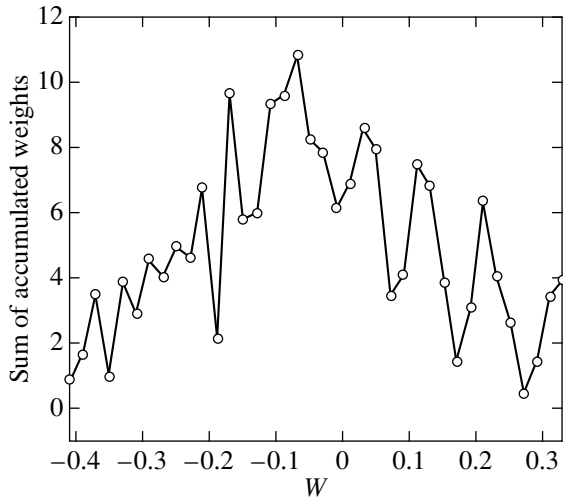
Frequency distribution of W estimates for probable members of the Praesepe.

data on Praesepe members. However, the proper motions of this catalog were reduced to the system of the Hipparcos catalog; data from the latter were combined with those used previously. The Hipparcos catalog was used in the form of a computer-readable version, which was kindly provided by Volkov from the Sternberg Astronomical Institute (Moscow State University).

The available data were supplemented (by calculating appropriate corrections) with data from Wang *et al.* (1995). We checked whether some stars belonged to the cluster by using radial velocities and *UBV* photometry from Mermilliod *et al.* (1990); only stars falling on the Praesepe main sequence were retained in the sample. As a result, we compiled a catalog of proper motions for 328 probable members of the Praesepe.

The formulas used to determine the cluster distance by Hertzsprung's method and the technique for statistical data reduction are given in Loktin and Matkin (1988) and were left here without changes. We only

give the main formula for estimating the distances to cluster stars:

$$r = -0.4208 \, v_R \tan(\theta/2)/\mu_\theta.$$

Here, r is the sought-for distance, v_R is the radial velocity (in our case, the velocity of the cluster as a whole), θ is the angular distance of the star from the cluster center, and μ_θ is the star's proper-motion component in the direction of the cluster center. Since the catalog size increased, the cluster parameters used to estimate the distances by the geometric method were redetermined. Thus, we took $V_R = +34.23 \pm 0.14$ km s^{-1} as the radial velocity of the cluster as a whole; it was determined as the mode of the frequency distribution of radial velocities for cluster members. In just the same way, using the modes of the corresponding distributions, we determined the coordinates of the cluster center, $\alpha_c = 8^h37^m45^s$ and $\delta_c = +19°46'42''$, and the proper-motion components of the cluster as a whole, $\mu_\alpha = -3''49/100$ yr and $\mu_\delta = -1''36/100$ yr. As previously, we estimated the mean distance to the cluster as the reciprocal of the mean of inverse distances $(1/r)$, which, as was shown by Loktin and Matkin (1988), yields a slightly biased estimate of the cluster distance. The frequency distribution of $W = \mu_\theta/\tan(\theta/2)$, which, to within a constant factor, matches the stellar trigonometric parallaxes, is presented in the figure, where only the core of the distribution without its broad wings is shown; the wings probably contain field stars that fell in the sample by chance or cluster stars with large errors of their proper motions. The figure presents the estimates of W obtained from 282 stars; the remaining ones refer to the distribution wings. As we see from the figure, the distribution maximum is determined quite reliably. Its position, the mode of the distribution, was found as a weighted mean of 15 central columns of the histogram. In this way, we obtained the distance to the Praesepe, $r = 171 \pm 15$ pc, which corresponds to an estimate of $6\overset{m}{.}16 \pm 0\overset{m}{.}19$ for its distance modulus. The errors

Table 1. Comparison of cluster parameters

Cluster	$(m - M)(\pi)$	$\sigma(\pi)$	$(m - M)$(Lyn)	$(m - M)$(Cat)	σ(Cat)	$(m - M)$(Cat) $- \Delta$
Praesepe	6.24	0.31	5.99	6.51	0.14	6.08
IC 4756	7.30	0.30	8.58	8.58	–	8.15
NGC 6475	7.32	0.30	7.08	7.55	0.11	7.12
NGC 6633	7.32	0.53	8.01	8.03	–	7.60
NGC 2516	7.71	0.20	8.49	8.21	0.13	7.78
NGC 3532	8.10	0.40	8.53	8.59	0.13	8.16
Coma	4.73	0.22	4.49	5.06	0.05	4.63
Pleiades	5.33	0.24	5.61	6.04	–	5.61
IC 2602	5.83	0.22	6.02	6.18	0.02	5.75
IC 2391	5.84	0.25	5.96	6.34	0.05	5.91
αPer	6.33	0.22	6.36	6.50	0.05	6.07

quoted here were determined as follows. We randomly divided our sample into five subsamples of equal size and determined the position of the maximum of the estimate distribution in each of them. The error in the mean of these five estimates was taken as an estimate of the error in the position of the distribution maximum found from the entire sample. Clearly, this error estimate is likely to be an upper limit for the error in the position of the maximum of the entire distribution.

As we see, our estimate of the distance modulus for the Praesepe lies exactly between its estimates (see Table 1) obtained from trigonometric parallaxes and photometrically (given the difference between the distance scales). In this case, the error in the distance determined by the trigonometric method is still fairly large, so even more accurate and homogeneous proper-motion measurements in the fields of several nearby clusters are required for a more successful use of the trigonometric method.

CONCLUSION

An analysis of the data in Table 1 leads us to conclude that the discrepancy between the distance estimates for open clusters obtained from Hipparcos trigonometric parallaxes and available photometric estimates is mainly random in nature. In this case, the separation of clusters into groups by agreement of data made by Mermilliod *et al.* (1997) appears unjustified, because the random errors in the distance moduli are fairly large—of the order of the distance-modulus differences established in the paper. The drawbacks of Hipparcos trigonometric parallaxes, which were mentioned, in particular, by Narayanan and Gould (1999) and Narayanan (1999), are also worthy of note here. In the former study, Narayanan and Gould used the trigonometric method to verify the distance to the Hyades estimated from Hipparcos trigonometric parallaxes, while in the latter, the authors found the distance modulus for the Pleiades to be $5^{m}.58 \pm 0^{m}.18$, which essentially matches the value in the last column of Table 1.

To elucidate the situation with Hipparcos trigonometric parallaxes requires both a careful search for possible sources of systematic errors in the distance moduli estimated from trigonometric parallaxes and increasing the number of clusters to which the trigonometric method of distance determination can be applied; in particular, the geometric method needs to be applied to other nearby clusters. Table 2 give data for open clusters which, in the near future, can become the objects of study by the moving-cluster method, provided that the proper motions of their members would

Table 2. Clusters with the largest v_R/r ratio

Cluster	r, pc	v_R/r
NGC 2232	396	0.051
NGC 2422	526	0.070
NGC 2516	439	0.050
NGC 2682	974	0.033
NGC 6622	404	0.072
IC 2391	185	0.081
IC 4756	519	0.055
Cr 121	642	0.055
Cr 135	339	0.099
Hyades	48	0.917
Praesepe	190	0.179

be determined with a high accuracy. Its columns give the following: (1) cluster names; (2) distance estimates for the clusters taken from our catalog (Loktin *et al.* 1997); and (3) ratios of radial velocity to distance, which determine whether the geometric method is applicable. We included NGC 2682 in the table, because this cluster is reach and well studied. We thus hope that the large sample size can offset the cluster remoteness. For comparison and for estimating the required accuracy of proper motions, the last two columns of the table give data for the Hyades and Praesepe clusters.

REFERENCES

1. A. V. Loktin and N. V. Matkin, Kinematika Fiz. Nebesn. Tel **4**, 59 (1988).
2. A. V. Loktin, P. E. Zakharova, *et al.*, Baltic Astron. **6**, 316 (1997).
3. G. Lynga, *Catalog of Open Cluster Data* (1987).
4. J.-C. Mermilliod, C. Turon, *et al.*, in *Proceedings of the ESA Symposium "Hipparchos-Ven.," Venice, Italy, 1997,* p. 643.
5. J.-C. Mremilliod, E. W. Weis, *et al.*, Astron. Astrophys. **235**, 114 (1990).
6. V. K. Narayanan, Astrophys. J. (1999) (in press).
7. V. K. Narayanan and A. Gould, Astrophys. J. **515**, 256 (1999).
8. N. Robichon, F. Arenou, *et al.*, in *Proceedings of the ESA Symposium "Hipparchos-Ven.," Venice, Italy, 1997,* p. 567.
9. J. J. Wang, L. Chen, *et al.*, Astron. Astrophys., Suppl. Ser. **113**, 419 (1995).

Translated by V. Astakhov

Unsteady Mass Outflow from Wolf–Rayet Stars

Kh. F. Khaliullin and A. I. Khaliullina*

Sternberg Astronomical Institute, Universitetskiĭ pr. 13, Moscow, 119899 Russia
Received December 27, 1999

Abstract—We show that hydrostatically equilibrium models for the thin photospheres of helium stars based on new opacities κ_R (OPAL and OP) can be constructed only for masses $M < 5M_\odot$. The parameter $\Gamma = \kappa L/4\pi GMc$, defined as the ratio of light pressure to gravity, exceeds a critical value of 1.0 for larger masses, which must result in mass outflow under light pressure. This mass limit matches the observed lower limit for the masses of Wolf–Rayet stars ($M_{WR} > 5M_\odot$)), which is an additional argument that the Wolf–Rayet stellar cores are actually helium stars. By solving the equation of radiative transfer in extended atmospheres, we construct a semiempirical model for a WN5 star ($M_{WN5} = 10M_\odot$)) with a helium core and an expanding envelope, whose physical and geometric parameters are known mainly from light-curve solution for the eclipsing binary V444 Cyg (WN5 + O6): outflow rate $\dot{M} \approx 1.0 \times 10^{-5}\,M_\odot\,\mathrm{yr}^{-1}$, terminal velocity $V_\infty \approx 2000\,\mathrm{km\,s^{-1}}$, and expanding-envelope optical depth $\tau_{env} \approx 25$. The temperature at the outer boundary of the photosphere of a helium star surrounded by such an envelope is approximately 130 kK higher than that in the absence of an envelope, being $T_{ph} \approx 240$ kK. Because of the high temperatures, the absorption coefficients at the corresponding photospheric levels are smaller than those in models with no envelope; therefore, the photosphere turns out to be in hydrostatic equilibrium and stable against light pressure ($\Gamma_{max} \approx 0.9$). As a way out of this conflicting situation (an expanding envelope together with a hydrostatically equilibrium photosphere), we propose a model of discrete mass outflow, which is also supported by the observed cloudy structure of the envelopes in this type of stars. To quantitatively estimate parameters of the nonuniform outflow model requires detailed gas-dynamical calculations. © *2000 MAIK "Nauka/Interperiodica".*

Keywords: *stars—variable and peculiar*

1. INTRODUCTION

Both observations and theoretical calculations suggest that the Wolf–Rayet (WR) stars are helium stars whose envelopes outflow under light pressure (Bisnovatyi–Kogan and Nadyozhin 1972; Cherepashchuk *et al.* 1984; Langer 1989; Maeder and Conti 1994; Moffat and Marchenko 1996; Heger and Langer 1996). However, there are problems here that have not yet been solved (Haman 1995; Schmutz 1995, 1996; Hillier 1995; Owocki and Gayley 1995). One of them is a large difference between the momentum flux ($\dot{M}_{WR} V_\infty$) carried away by the outflowing matter and the photon momentum flux (L_{WR}/c). Abbot *et al.* (1986) estimated the flux ratio to be $4 < (\dot{M}_{WR} V_\infty)/(L_{WR}/c) < 14$, while its values obtained by Barlow *et al.* (1981) are even a factor of 3 larger. Multiple photon scattering in an extended envelope in optically thick lines increases the efficiency of photon-momentum transfer to the outflowing matter several-fold (Abbot and Lucy 1985), but does not remove this problem completely. At the same time, for the mechanism of multiple photon scattering

to work more efficiently than it does in O and Of stars, the matter in optically deep (in continuum) atmospheric layers of these stars must be initially accelerated. There is direct observational evidence that the acceleration of matter begins in deep layers of WR stellar envelopes. For example, an analysis of light curves for the eclipsing binary V444 Cyg (WN5 + O6) shows that the velocity of mass outflow from the WN5 component at the optical depth for electron scattering $\tau_e = 2/3$ is ~400 km s^{-1} (Cherepashchuk *et al.* 1984). In addition, an analysis of the widths of emission lines and their absorption components indicates that the upper regions of continuum formation in WR envelopes expand at velocities from several hundred to a thousand km s^{-1} (Abbot and Conti 1987).

However, as follows from the solution of the equation of radiative transfer in extended envelopes, light pressure is not enough to overcome the gravitational attraction and for mass outflow to begin in optically deep layers of a homogeneous envelope (Schmutz 1996).

This study aims at seeking the cause of matter acceleration at large optical depths. We use the iterative method of solving the equation of radiative transfer for gray extended atmospheres developed by Hummer and Rybicki (1971). The theory of gray atmospheres is vir-

* E-mail address for contacts: hvh@sai.msu.ru

tually always used in investigating optically deep layers of WR stellar envelopes to determine the dependence $T(r)$ for a given density $\rho(r)$ (Pauldrach *et al.* 1985; Hillier 1987; Heger and Langer 1996).

In our model calculations, we focused on ascertaining physical conditions in the thin photospheres of helium stars, which are in a state close to hydrostatic equilibrium. This approach allowed us to elucidate the physical nature of the lower mass limit for WR stars ($M_{min} \approx 5M_\odot$)). Besides, our investigation of the quasi-equilibrium photospheres of helium stars hidden by optically thick expanding envelopes led us to the idea of mass outflow from WR stars in the form of ejection of individual microenvelopes and necessitated performing gas-dynamical calculations in terms of the nonuniform outflow model.

2. PHOTOSPHERIC MODELS FOR HELIUM STARS

A general model of a WR star with a helium core surrounded by an expanding envelope is considered in the next section, while here we construct plane-parallel models for the thin photospheres of helium stars without envelopes in hydrostatic equilibrium:

$$dP_g(r) = -\rho g_{eff} dr, \qquad (1)$$

Here, $g_{eff} = g(1 - \Gamma)$; P_g is the gas pressure; g_{eff} is the effective gravity; $g = GM_{WR}/r^2$; and Γ is a well-known parameter, the ratio of light pressure to gravity,

$$\Gamma = \kappa \frac{L_{WR}}{4\pi G M_{WR} c}, \qquad (2)$$

where G is the gravitational constant, c is the speed of light, and κ is the mean absorption coefficient per unit mass. We take the approximation $\kappa = \kappa_R(\rho, T)$, where κ_R is the mean Rosseland coefficient.

We took basic physical model parameters (M, L, and R) for helium stars from Langer (1989) for the mean $Y = 0.50$, C $= 0.354$, and O $= 0.146$. Since we are mainly interested in problems related to light pressure in optically deep layers, we use the simplest LTE model of a gray atmosphere whose methods of solution are well known. In our calculations, we used the currently available OPAL tables for $\kappa_R(\rho, T)$ published by Iglesias and Rogers (1996). By contrast to previous data, bound–bound transitions have already been taken into account in these tables; therefore, there is no need to separately allow for absorption in spectral lines. The new values of $\kappa_R(\rho, T)$ in the temperature range from 100 to 400 kK are a factor of 2 or 3 larger than the previous ones, which, according to our calculations, is of fundamental importance in solving the problem of WR stars.

Note that Langer (1989) computed models for the internal structure of helium stars as standard models of WR stars before the publication of the first OPAL tables by Rogers and Iglesias (1992). However, the new tables essentially match the previous data for temperatures
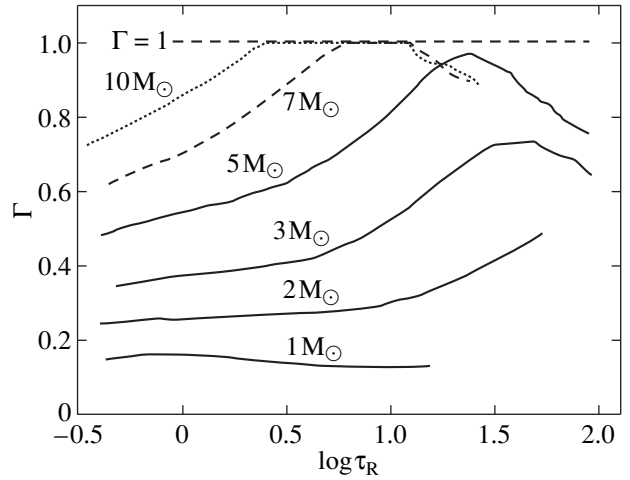
Fig. 1. $\Gamma = \kappa L/4\pi GMc$ versus $\log \tau_R$ (ρ, T) for the hydrostatically equilibrium photospheres of helium stars of various masses without envelopes. The actual equilibrium photospheric configurations are obtained only for helium stars with $M \le 5M_\odot$ (solid lines). For $M > 5M_\odot$ (dashed lines), quasi-equilibrium of the photospheres is reached only artificially, through the adopted constraint $\Gamma_{max} \le 1$.

$T \ge 5 \times 10^5$ K, at which more than 99% of the stellar mass is. Therefore, the new opacity data cannot change significantly the fundamental parameters of helium stars used here. In addition, Beech and Mitalas (1992) inferred luminosities of helium stars similar to those determined by Langer (1989).

Since there is virtually no hydrogen in the envelopes of WR stars (Torres *et al.* 1986; Nugis and Niedzielski 1995), we took the following chemical composition: $X = 0.00$ and $Z = 0.02$. The mass fraction of N, C, and O should apparently be increased significantly in detailed gas-dynamical calculations. According to our estimates, increasing the mass fraction of these elements causes $\kappa_R(\rho, T)$ to slightly increase in the temperature range 100–400 kK of interest. It should be noted, however, that the chemical composition of the outer layers of a helium star can differ markedly from the mean for the entire star.

Figure 1 shows the results of our calculations of the thin photospheres in helium stars of various masses in the form of a plot of Γ against $\log \tau$. We see that, as the mass of the helium star increases, the maximum value of this parameter Γ_{max} in its photosphere increases and reaches almost unity for $M = 5M_\odot$. At the same time, the actual values of this parameter are $\Gamma_{max} > 1$ for helium stars with $M > 5M_\odot$, although we introduced the following formal constraint for the effective gravity in the programs of calculations (to ensure that the photosphere be quasi-stable): $g_{eff} = g(1 - \Gamma) \ge 0$, i.e., $\Gamma \le 1$.

It is clear from Fig. 1 that the helium stars have hydrostatically equilibrium photospheres and can be observed as normal main-sequence stars with thin

photospheres only for $M \le 5M_\odot$. For $M > 5M_\odot$, the light pressure in certain photospheric layers exceeds the force of gravitational attraction, and conditions for the onset of mass outflow and for the formation of an extended envelope arise. Since the lower limit on the measured masses of WR stars is also $5M_\odot$ (Massey 1981; Cherepashchuk 1996), our result is an additional argument that the helium stars are WR cores.

Clearly, the structure and physical parameters of an envelope outflowing under light pressure must be determined from specific gas-dynamical calculations. At present, effective algorithms for computing gas-dynamical models have been developed [see Bisnovatyi-Kogan and Dorodnitsyn (1999) and references therein], and results of such calculations have been published (Lucy and Abbot 1993; Springmann 1994; Haman 1995; Heger and Langer 1996). Here, we do not analyze the results of these calculations. We only note that, first, the envelopes of WR stars are interpreted only in terms of the uniform outflow model, and, second, the boundary conditions, unfortunately, are commonly taken to be far from the observed parameters of WR stars.

In the next section, in which a semiempirical model is developed for a WN5 star, we attempt to justify the necessity of using nonuniform outflow models and present the initial physical and geometric parameters of the WN5 star and the photosphere of its helium core required for subsequent gas-dynamical calculations, which are closer to the actual parameters of WR stars.

3. A SEMIEMPIRICAL MODEL FOR A WN5 STAR

The most reliable data on WR stars were obtained by analyzing the light and radial-velocity curves of eclipsing binaries. Seven of ~200 WR stars are known to be eclipsing systems, of which V444 Cyg (WN5 + O6) has been studied best. From the light-curve solution for this system in a wide wavelength range 1200 Å–3.5 μm (Cherepashchuk *et al.* 1984), it was mainly established that the helium remnants of initially more massive stars predicted by the evolutionary theory are observed as WR stars. To construct a semiempirical model for a WR star, we therefore took the WN5 component of V444 Cyg, whose physical parameters were determined by many authors (Khaliullin 1974; Hartman 1978; Eaton *et al.* 1982; Khaliullin *et al.* 1984; Cherepashchuk *et al.* 1984, 1995; Eaton *et al.* 1985; Robert *et al.* 1990; St-Louis *et al.* 1993; Marchenko *et al.* 1994; Antokhin *et al.* 1995; Moffat and Marchenko 1996):

$i = 78°0 \pm 0°5,$ $M_{WN5} = (9.3 \pm 0.5)M_\odot,$

$R_{2/3} = (2.9 \pm 0.5)R_\odot,$ $L_{WN5} \approx (0.5–1.0) \times 10^{39}$ erg s^{-1},

$V_{2/3} = (400 \pm 100)$ km s^{-1}, $r_\infty = (35 \pm 5)R_\odot$

$V_\infty = (2000 \pm 300)$ km s^{-1}, $T_{WN5}^{eff} \approx (75 \pm 10)$ kK,

$\dot{M}_{WN5} = (1.0 \pm 0.3) \times 10^{-5}M_\odot$ yr^{-1}.

Here, r_∞ is the maximum acceleration radius of the envelope matter in the model of uniformly accelerated motion, $R_{2/3}$ and $V_{2/3}$ are the radius and velocity of outflow at the optical depth for electron scattering $\tau_e = 2/3$; the remaining notation is conventional.

Our model of the WN5 star consists of a helium star with a thin photosphere surrounded by an envelope whose expansion follows a specified law $V(r)$ with a mass outflow rate $\dot{M}$. Based on the observed parameters of the WN5 star, we chose the model for the stellar core with $M = 10M_\odot$, $X = 0$, $Y = 0.5$, $C = 0.354$, and $O = 0.146$ from the series of helium-star models computed by Langer (1989):

$M_{WR} = 10M_\odot,$ $\log L_{WR} = 5.19,$ $R_{ph} = 1.00R_\odot,$ $\bar{\mu} = 1.76.$

The so-called β law with $\beta \approx 1.0$ (Lamers and Cassinelli 1999) is commonly taken for the velocity distribution $V(r)$ in an envelope expanding under light pressure. An analysis of observational data shows that the β law appears to be a suitable approximation for the atmospheres of O and Of stars. However, this law is inconsistent with the light curves of V444 Cyg, whose solution better corresponds to uniformly accelerated motion of matter in the envelope of the WN5 component (Khaliullin and Khaliullina 2000). This may be because the acceleration of matter in WR stars appears to be first produced by light pressure in the entire continuum and then by the absorption of emission mainly outside the major series of various species; in higher layers of the envelope, the absorption and scattering of emission in individual spectral lines of various species at various ionization stages contribute to the acceleration of matter. For WR stars, all these processes may have a more uniform radial distribution than those for O and Of stars. For uniformly accelerated motion, we have

$$V(r) = \begin{cases} \sqrt{(r - r_0)2a + V_s^2} & \text{for} \quad r < r_\infty \\ V_\infty = \text{const} & \text{for} \quad r \ge r_\infty, \end{cases} \quad (3)$$

where the acceleration a is given by

$$a = \frac{1}{2}\frac{V_\infty^2 - V_s^2}{r_\infty - r_0}. \quad (4)$$

Here, $r_\infty = (35 \pm 5)R_\odot$ is the envelope acceleration radius, $V_s \approx 30$ km s^{-1} is the speed of sound near the envelope base, and $V_\infty = 2000$ km s^{-1} is the terminal velocity. The parameters r_∞ and V_∞ were taken in accordance with the most recent solution of the most accurate continuum (λ 4500 Å) light curve for V444 Cyg (Khaliullin and Khaliullina 2000). They differ only slightly from previous results (Cherepashchuk *et al.* 1984; Eaton *et al.* 1982).

Relation (3) establishes the density distribution in the envelope through the continuity equation:

$$\rho(r) = \dot{M}/4\pi r^2 V(r). \quad (5)$$

The mass outflow rate $\dot{M}$ is one of the fundamental parameters of WR stars. The values of $\dot{M}$ obtained from infrared (Barlow *et al.* 1981) and radio (Abbot *et al.* 1986) observations of these stars reach 10^{-4} $M_\odot$ yr^{-1}. However, transforming the free–free flux into a mass flux requires knowledge of the velocity distribution in the envelope, its chemical composition, electron temperature, etc. In addition, this transformation is made by assuming a spherically symmetric expanding homogeneous envelope with density $\rho \propto r^{-2}$. The assumption of a homogeneous envelope is most critical here, because the intensity of free–free emission is roughly proportional to the density squared. At the same time, Cherepashchuk *et al.* (1984) adduced convincing arguments for inhomogeneity of the WR envelopes, and the view that the WR stellar winds are essentially inhomogeneous prevails among the researchers of these stars.

In the model of the WN5 star, we therefore used $\dot{M}$ estimated from the dynamics of change in the orbital period of V444 Cyg (Khaliullin 1974; Khaliullin *et al.* 1984; Antokhin *et al.* 1995):

$$\dot{M}_{WN5} = (1.0 \pm 0.2) \times 10^{-5} \, M_\odot \, \text{yr}^{-1}, \quad (6)$$

which is free from *a priori* model assumptions, in particular, of uniform outflow.

When solving the equation of radiative transfer in an expanding envelope, we use the so-called effective opacity (Lucy and Abbot 1993),

$$\kappa_{eff} = \frac{4\pi r^2 c}{L}\left(V\frac{dV}{dr} + \frac{GM}{r^2}\right), \quad (7)$$

which provides the required light-pressure force for motion with the specified velocity distribution $V(r)$. This opacity is commonly used to analyze moving envelopes (Heger and Langer 1996). In section 4, we return to the practice of using κ_{eff}. At the same time, for the thin photosphere of a helium star, we use, as in section 2, the actual absorption coefficients $\kappa_R(\rho, t)$ as inferred by Iglesias and Rogers (1996).

Having determined all the required model parameters, we performed numerical calculations. Simultaneously solving the equation of radiative transfer for our model of a WN5 star consisting of an expanding envelope with $V(r)$ and $\dot{M}$ specified above and the thin photosphere of a helium star with the specified L, M, R, and $\bar{\mu}$ yielded the radial distributions of temperature and other physical parameters. In Fig. 2, Γ is plotted against $\tau_R^{ph} = (\tau - \tau^{env})$ for the thin photosphere of a helium star surrounded by an envelope. Here, τ is the total optical depth, and τ^{env} is the optical depth of the expanding envelope. Since the results of these calculations are of considerable importance, the model of this photosphere is presented in the table in the form of radial (r [$R_\odot$]) distributions of temperature T [K],
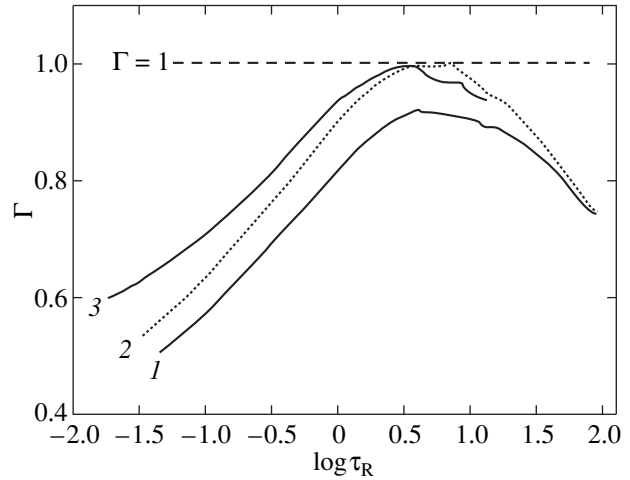
Fig. 2. $\Gamma = \kappa L/4\pi GMc$ versus $\log\tau_R$ (ρ, T) for the photosphere of the helium core in a WN5 star for various times of the scenario for single microenvelope ejection: curve *1* for a hydrostatically equilibrium photosphere (see the table) at the initial time ($t_0 = 0$), when $\Gamma_{max} = 0.92$; curve *2* for a hydrostatically nonequilibrium photosphere ($t_{rel} = \infty$) at the critical time $t = t_{cr}$, when $\Gamma_{max} = 1$ is reached; curve *3* for a hydrostatically equilibrium photosphere ($t_{rel} = 0$) at the critical time $t = t_{cr}$, when $\Gamma_{max} = 1$ is reached.

logarithm of density $\log\rho$ [g cm^{-3}], optical depth $\tau_R^{ph} = (\tau - \tau^{env})$, mean Rosseland absorption coefficient κ_R [cm^2 g^{-1}], effective gravity g_{eff} [cm s^{-2}] $= g(1 - \Gamma)$, gas pressure P_g [g cm^{-2}], Γ, and photospheric mass ΔM [g] above the r level.

We see from Fig. 2 and the table that the photosphere of a helium star surrounded by an envelope with the observed physical parameters of a WN5 star is in hydrostatic equilibrium and stable against light pressure ($\Gamma_{max} = 0.92$), by contrast to the case of no envelope (Fig. 1) where $\Gamma_{max} \geq 1$ (for $M = 10M_\odot$)); i.e., the optically thick envelope of a WN5 star stabilizes the thin photosphere of its core (it is in hydrostatic equilibrium) and makes it stable against light pressure. This is our main conclusion. Varying the input parameters over a range that is twice the probable errors in the observed parameters of a WN5 star does not change this result qualitatively.

4. DISCUSSION

From the viewpoint of steady uniform outflow, it is clear that the situation when a hydrostatically equilibrium and stable photosphere is surrounded by an expanding envelope is internally conflicting. There are three possible ways out of this situation:

(i) **Invoking other mechanisms** to trigger mass outflow in optically deep layers of the envelope: a rotating magnetic field (Underhill *et al.* 1990), radial pulsations (Maeder 1985), nonradial pulsations (Vreux

A hydrostatically equilibrium photosphere of the helium core in a model WN5 star surrounded by an expanding envelope ($\dot{M} = 1.0 \times 10^{-5}\,M_\odot\,\mathrm{yr}^{-1}$; $\tau^{\mathrm{env}} = 24.9$)

| $r, R_\odot$	T, K	$\tau_R^{\mathrm{ph}} = \tau - \tau^{\mathrm{env}}$	κ_R, cm^2 g^{-1}	$\log\rho$, g cm^{-3}	$g_{\mathrm{eff}} = g(1 - \Gamma)$	P_{g}, g cm^{-2}	Γ	ΔM, g
1.0198	211951.	.001	.382	−9.85	.144E+06	.143E+04	.4530	.189E+21
1.0196	211965.	.003	.382	−9.69	.144E+06	.204E+04	.4530	.459E+21
1.0193	211983.	.005	.382	−9.53	.144E+06	.292E+04	.4529	.844E+21
1.0187	212033.	.013	.382	−9.22	.145E+06	.599E+04	.4528	.218E+22
1.0184	212070.	.020	.382	−9.07	.145E+06	.858E+04	.4526	.331E+22
1.0178	212185.	.045	.427	−8.78	.131E+06	.166E+05	.5059	.708E+22
1.0172	212387.	.095	.478	−8.54	.115E+06	.293E+05	.5668	.138E+23
1.0166	212719.	.187	.538	−8.33	.961E+05	.468E+05	.6376	.249E+23
1.0160	213226.	.338	.591	−8.17	.795E+05	.685E+05	.7007	.413E+23
1.0154	213941.	.563	.636	−8.04	.655E+05	.931E+05	.7537	.638E+23
1.0148	214890.	.872	.679	−7.93	.520E+05	.119E+06	.8046	.928E+23
1.0145	215455.	1.060	.697	−7.89	.462E+05	.131E+06	.8264	.110E+24
1.0139	216754.	1.498	.727	−7.82	.371E+05	.155E+06	.8608	.148E+24
1.0133	218258.	2.016	.747	−7.76	.306E+05	.177E+06	.8853	.191E+24
1.0124	220829.	2.925	.767	−7.70	.245E+05	.209E+06	.9084	.266E+24
1.0121	221756.	3.261	.771	−7.68	.231E+05	.219E+06	.9136	.293E+24
1.0118	222711.	3.613	.775	−7.66	.220E+05	.229E+06	.9177	.321E+24
1.0115	223688.	3.979	.777	−7.65	.211E+05	.239E+06	.9211	.351E+24
1.0112	224438.	4.165	.775	−7.64	.219E+05	.244E+06	.9183	.366E+24
1.0108	226021.	4.746	.775	−7.61	.221E+05	.260E+06	.9176	.412E+24
1.0106	226558.	4.946	.774	−7.60	.222E+05	.266E+06	.9173	.428E+24
1.0102	228206.	5.573	.773	−7.58	.225E+05	.284E+06	.9161	.479E+24
1.0100	228768.	5.790	.773	−7.57	.227E+05	.291E+06	.9157	.496E+24
1.0099	229336.	6.011	.772	−7.56	.228E+05	.297E+06	.9151	.514E+24
1.0094	231082.	6.700	.771	−7.54	.233E+05	.318E+06	.9134	.569E+24
1.0093	231677.	6.939	.770	−7.53	.235E+05	.325E+06	.9127	.589E+24
1.0091	232279.	7.183	.770	−7.52	.237E+05	.333E+06	.9121	.608E+24
1.0087	234127.	7.943	.768	−7.49	.243E+05	.356E+06	.9099	.669E+24
1.0085	234757.	8.206	.767	−7.48	.245E+05	.365E+06	.9091	.691E+24
1.0079	237351.	9.315	.765	−7.45	.254E+05	.401E+06	.9058	.780E+24
1.0075	239375.	10.207	.762	−7.42	.261E+05	.431E+06	.9032	.852E+24
1.0065	243835.	12.162	.756	−7.36	.283E+05	.501E+06	.8952	.101E+25
1.0057	248091.	14.182	.752	−7.31	.294E+05	.580E+06	.8914	.118E+25
1.0050	252231.	16.250	.750	−7.26	.302E+05	.661E+06	.8888	.135E+25
1.0043	256170.	18.318	.744	−7.21	.321E+05	.748E+06	.8820	.152E+25
1.0036	260326.	20.608	.739	−7.16	.339E+05	.850E+06	.8754	.171E+25
1.0029	264717.	23.157	.733	−7.11	.358E+05	.971E+06	.8686	.192E+25
1.0022	269497.	26.003	.726	−7.06	.383E+05	.112E+07	.8598	.216E+25
1.0015	274792.	29.368	.719	−7.00	.406E+05	.130E+07	.8513	.244E+25
1.0015	275080.	29.557	.718	−7.00	.407E+05	.131E+07	.8509	.246E+25
1.0015	275369.	29.747	.718	−6.99	.409E+05	.132E+07	.8504	.247E+25
1.0009	279828.	32.759	.712	−6.95	.429E+05	.150E+07	.8433	.273E+25
1.0004	283567.	35.401	.706	−6.91	.447E+05	.166E+07	.8368	.296E+25
.9997	290157.	40.328	.696	−6.84	.482E+05	.199E+07	.8243	.339E+25
.9990	296503.	45.417	.686	−6.77	.516E+05	.236E+07	.8122	.383E+25
.9985	302121.	50.222	.676	−6.72	.546E+05	.273E+07	.8015	.426E+25
.9979	308058.	55.628	.667	−6.66	.578E+05	.319E+07	.7901	.475E+25
.9974	313479.	60.876	.658	−6.61	.607E+05	.366E+07	.7796	.523E+25
.9970	318274.	65.785	.651	−6.56	.632E+05	.412E+07	.7708	.569E+25
.9966	322807.	70.670	.644	−6.52	.655E+05	.461E+07	.7628	.614E+25
.9963	327029.	75.448	.637	−6.48	.677E+05	.511E+07	.7550	.659E+25
.9959	331387.	80.623	.630	−6.44	.700E+05	.567E+07	.7467	.709E+25
.9956	335385.	85.607	.628	−6.41	.706E+05	.623E+07	.7445	.757E+25
.9955	336945.	87.579	.627	−6.39	.710E+05	.645E+07	.7434	.776E+25

1985), pure rotation and mass outflow in the equatorial plane (Sreenivasan and Wilson 1982; Cassinelli 1992), etc. Although these and other possible mechanisms can contribute to the acceleration of matter for some stars, as yet none of these mechanisms has been observationally supported for the physical nature of the entire class of WR stars to be determined.

(ii) **Revising the absorption coefficients.** After publication of the OPAL tables of Rosseland mean absorption coefficients $\kappa_R(\rho, t)$ (Rogers and Iglesias 1992; Iglesias and Rogers 1996) and other (OP, SYMP) tables, which turned out to be a factor of 2 or 3 higher than their values from previous studies in the range $T = 10^5$–4×10^5 K, in particular, the tables by Cox and Stewart (1970) widely used for more than twenty years, and which opened up new pages in the physics of many types of stars (Rogers and Iglesias 1994), the possibility that the currently available κ_R will not change appreciably in the future cannot be completely ruled out. However, the fact that the independent results of several competing teams of researchers, in particular, OPAL, OP, SYMP, etc. (Iglesias and Rogers 1996) have recently differed by no more than 10–15% (for the temperature range of interest), gives hope that the errors of the currently available κ_R do not exceed 15%. Variations of κ_R in this range cannot change significantly the results of our calculations and cannot remove the conflict under discussion.

(iii) **Discrete (nonuniform) mass outflow from the photosphere.** The essence of nonuniform outflow is as follows. As the envelope expands (without mass influx) and as its optical depth decreases, the temperature of the initially stable photosphere drops, causing the absorption coefficient κ_R and, accordingly, $\Gamma(r)$ to increase in the photosphere. When $\Gamma(r_{cr})$ at some r_{cr} levels exceeds a critical value equal to unity, the necessary condition for the ejection of part of the photosphere above the r_{cr} level as a separate microenvelope arises. This mechanism of discrete (nonuniform) mass outflow seems most likely and natural as a way out of the conflicting situation found.

To illustrate how such an outflow model works, let us consider the scenario of a single microenvelope ejection. Figure 3 shows variations in some parameters of this scenario with time, where $\tau^{env}(t)$ is the optical depth of the envelope expanding under light pressure with the specified $V(r)$ and $\dot{M}$. Since the photosphere is in hydrostatic equilibrium at the initial time ($t_0 = 0$) and $\Gamma_{max} = 0.92$, we assume that there is no continuous "replenishment" of the envelope with photospheric matter. That is why the envelope optical depth decreases with time, while the photospheric temperature drops.

$\Gamma_{max}(t)$ is the maximum value of $\Gamma(r)$. It varies due to the expansion of the surrounding envelope and the corresponding decrease in photospheric temperature. If the temperature of the photosphere varies much faster than its dynamical relaxation, the density distribution
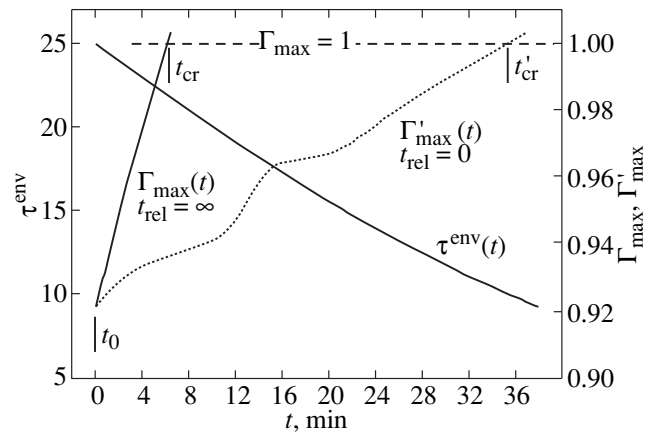
Fig. 3. $\tau^{env}(t)$, $\Gamma_{max}(t)$, and $\Gamma'_{max}(t)$ versus time in the scenario for single microenvelope ejection by the helium core of a WN5 star.

can remain virtually constant: $\rho(r, t) = \rho(r, t_0)$. We calculated the dependence $\Gamma_{max}(t)$ under this assumption, i.e., that the dynamical relaxation time of the photosphere is $t_{rel} = \infty$.

$\Gamma'_{max}(t)$ is the variation of the same parameter with time in a series of photospheric models calculated for the other extreme case: $t_{rel} = 0$, i.e., when $\rho(r, t)$ instantaneously rearranges following the temperature variations.

We see from Fig. 3 that, both for $t_{rel} = \infty$ and for $t_{rel} = 0$, envelope expansion results in $\Gamma_{max}(t)$ becoming larger than unity, and the part of the photosphere above the critical level r_{cr} can be ejected as a microenvelope. In Fig. 2, Γ is plotted against $\log\tau_R$ for the critical times t_{cr} and t'_{cr}, when $\Gamma_{max}(t)$ and $\Gamma'_{max}(t)$ reach unity for the $t_{rel} = \infty$ and $t_{rel} = 0$ models, respectively. The critical value $\Gamma_{max} = 1$ is seen to be reached at optical depths $\tau \approx 3$–7, depending on t_{rel}. The ejection time also depends on t_{rel}: $t_{cr} = 6$ min for $t_{rel} = \infty$ and $t'_{cr} = 35$ min for $t_{rel} = 0$. The mass of the ejected microenvelope can be estimated as well: $\Delta M \approx (3$–5$) \times 10^{23}$ g. However, these estimates, which are valid for the model of single envelope ejection considered above, can change appreciably in the case of steady-state periodic microenvelope ejection, because it is clear that the photosphere cannot completely return to equilibrium in the time between two cycles of microenvelope ejection.

A helium core with a thin unsteady photosphere plus a set of microenvelopes expanding under light pressure and breaking up because of various kinds of instability can represent a WR star in the nonuniform outflow model. To quantitatively estimate parameters of this model requires detailed gas-dynamical calculations. This model is supported by the observed cloudy structure of the envelopes of this type of stars (Chere-

pashchuk *et al.* 1984; Moffat *et al.* 1988). Since the time scale of microenvelope ejection (6–35 min) was estimated roughly, it is also interesting to note that quasi-periodic light variations on a time scale $t \sim 20$–30 min with an amplitude $A \approx 0\overset{m}{.}05$ were detected in some WR stars, including the WN5 star of HD 50896 (Bratschi 1995).

We now turn to the practice of using the effective absorption coefficient κ_{eff} given by relation (7). It is used, because the actual absorption coefficients $\kappa_R(\rho, T)$ in the uniform outflow model are always considerably smaller than κ_{eff}, which is commonly attributed to absorption in spectral lines that have not been taken into account (Heger and Langer 1996). However, as was noted above, after a series of fruitful works by several teams of researchers on the revision of absorption coefficients, there is no particular hope that spectral lines that have not yet been taken into account or other unknown causes can change significantly the absorption coefficients for conditions close to local thermodynamic equilibrium. Therefore, the only possibility to reconcile κ_{eff} with actual $\kappa_R(\rho, T)$ is to accept the hypothesis that the envelope matter is inhomogeneous and collected in clumps (microenvelopes, clouds, globules). According to our calculations, for κ_{eff} to be reconciled with $\kappa_R(\rho, T)$, the matter in optically deep layers of the envelope ($\tau_e > 2/3$) must be collected in such globules (microenvelopes), whose density is a factor of 10–100 higher than the density given by the continuity equation (5). This is yet another weighty argument for the initially nonuniform mass outflow from the cores of WR stars.

REFERENCES

1. D. C. Abbott and P. C. Conti, Annu. Rev. Astron. Astrophys. **25**, 113 (1987).
2. D. C. Abbott and L. B. Lucy, Astrophys. J. **288**, 679 (1985).
3. D. C. Abbott, J. H. Bieging, E. Churchwell, and A. V. Torres, Astrophys. J. **303**, 239 (1986).
4. I. I. Antokhin, S. V. Marchenko, and A. F. J. Moffat, in *Wolf–Rayet Stars: Binaries, Colliding Winds, Evolution*, Ed. by K. A. van der Hucht and P. M. Williams, IAU Symp. No. 163 (Kluwer, Dordrecht, 1995), p. 520.
5. M. J. Barlow, L. J. Smith, and A. J. Willis, Mon. Not. R. Astron. Soc. **196**, 101 (1981).
6. M. Beech and R. Mitalas, Astron. Astrophys. **262**, 483 (1992).
7. G. S. Bisnovatyi-Kogan and A. V. Dorodnitsyn, Astron. Astrophys. **344**, 647 (1999).
8. G. S. Bisnovatyi-Kogan and D. K. Nadyozhin, Astrophys. Space Sci. **15**, 353 (1972).
9. P. Bratschi, in *Wolf–Rayet Stars: Binaries, Colliding Winds, Evolution*, Ed. by K. A. van der Hucht and P. M. Williams, IAU Symp. No. 163 (Kluwer, Dordrecht, 1995), p. 64.
10. J. P. Cassinelli, Astron. Soc. Pac. Conf. Ser. **22**, 134 (1992).
11. A. M. Cherepashchuk, in *Proceedings of 33rd Liege International Astrophysical Colloquium, Liege, Universite de Liege, Institut d'Astrophysique, 1996*, Ed. by J. M. Vreux *et al.*, B-4000, p. 155.
12. A. M. Cherepashchuk, J. A. Eaton, and Kh. F. Khaliullin, Astrophys. J. **281**, 774 (1984).
13. A. M. Cherepashchuk, G. Koenigsberger, S. V. Marchenko, and A. F. J. Moffat, Astron. Astrophys. **293**, 142 (1995).
14. A. N. Cox and J. N. Stewart, Astrophys. J., Suppl. Ser. **19**, 243 (1970).
15. J. A. Eaton, A. M. Cherepashchuk, and Kh. F. Khaliullin, in *Advances in Ultraviolet Astronomy: Four Years of IUE Reseach*, Ed. by Y. Kondo, J. M. Mead, and R. D. Chapman, NASA Conf. Publ. **2238**, 542 (1982).
16. J. A. Eaton, A. M. Cherepashchuk, and Kh. F. Khaliullin, Astrophys. J. **297**, 266 (1985).
17. W.-R. Haman, in *Wolf–Rayet Stars: Binaries, Colliding Winds, Evolution*, Ed. by K. A. van der Hucht and P. M. Williams, IAU Symp. No. 163 (Kluwer, Dordrecht, 1995), p. 105.
18. L. Hartman, Astrophys. J. **221**, 193 (1978).
19. A. Heger and N. Langer, Astron. Astrophys. **315**, 421 (1996).
20. D. J. Hillier, Astrophys. J., Suppl. Ser. **63**, 965 (1987).
21. D. J. Hillier, in *Wolf–Rayet Stars: Binaries, Colliding Winds, Evolution*, Ed. by K. A. van der Hucht and P. M. Williams, IAU Symp. No. 163 (Kluwer, Dordrecht, 1995), p. 116.
22. D. G. Hummer and G. B. Rybicki, Mon. Not. R. Astron. Soc. **152**, 1 (1971).
23. C. A. Iglesias and F. J. Rogers, Astrophys. J. **464**, 943 (1996).
24. Kh. F. Khaliullin, Astron. Zh. **51**, 395 (1974) [Sov. Astron. **18**, 229 (1974)].
25. Kh. F. Khaliullin and A. I. Khaliullina, personal communication, 2000.
26. Kh. F. Khaliullin, A. I. Khaliullina, and A. M. Cherepashchuk, Pis'ma Astron. Zh. **10**, 600 (1984) [Sov. Astron. Lett. **10**, 250 (1984)].
27. H. J. G. L. M. Lamers and J. P. Cassinelli, *Introduction to Stellar Winds* (Cambridge Univ. Press, Cambridge, 1999).
28. N. Langer, Astron. Astrophys. **210**, 93 (1989).
29. L. B. Lucy and D. C. Abbott, Astrophys. J. **405**, 738 (1993).
30. A. Maeder, Astron. Astrophys. **147**, 300 (1985).
31. A. Maeder and P. S. Conti, Annu. Rev. Astron. Astrophys. **32**, 227 (1994).
32. S. V. Marchenko, A. F. J. Moffat, and G. Koenigsberger, Astrophys. J. **422**, 810 (1994).
33. P. Massey, Astrophys. J. **246**, 153 (1981).

34. A. F. J. Moffat and S. V. Marchenko, Astron. Astrophys. **305**, L29 (1996).

35. A. F. J. Moffat, L. Drissen, R. Lamontagne, and C. Robert, Astrophys. J. **334**, 1038 (1988).

36. T. Nugis and A. Niedzielski, Astron. Astrophys. **300**, 237 (1995).

37. S. P. Owocki and K. G. Gayley, in *Wolf–Rayet Stars: Binaries, Colliding Winds, Evolution*, Ed. by K. A. van der Hucht and P. M. Williams, IAU Symp. No. 163 (Kluwer, Dordrecht, 1995), p. 138.

38. A. Pauldrach, J. Puls, D. G. Hummer, and R. P. Kudritzki, Astron. Astrophys. **148**, L1 (1985).

39. C. Robert, A. F. J. Moffat, P. Bastien, *et al.*, Astrophys. J. **359**, 211 (1990).

40. F. J. Rogers and C. A. Iglesias, Astrophys. J., Suppl. Ser. **79**, 507 (1992).

41. F. J. Rogers and C. A. Iglesias, Science **263**, 50 (1994).

42. W. Schmutz, in *Wolf–Rayet Stars: Binaries, Colliding Winds, Evolution*, Ed. by K. A. van der Hucht and P. M. Williams, IAU Symp. No. 163 (Kluwer, Dordrecht, 1995), p. 127.

43. W. Schmutz, in *Proceeding of 33rd Liege International Astrophysical Colloquium, Liege, Universite de Liege, Institut d'Astrophysique, 1996*, Ed. by J. M. Vreux *et al.*, B-4000, p. 655.

44. U. Springmann, Astron. Astrophys. **289**, 505 (1994).

45. S. R. Sreenivasan and W. J. F. Wilson, Astrophys. J. **254**, 287 (1982).

46. N. St-Lous, A. F. J. Moffat, L. Lapointe, *et al.*, Astrophys. J. **410**, 342 (1993).

47. A. V. Torres, P. S. Conti, and P. Massey, Astrophys. J. **300**, 379 (1986).

48. A. B. Underhill, K. K. Gilroy, G. M. Hill, and N. Dinshaw, Astrophys. J. **351**, 666 (1990).

49. J.-M. Vreux, Publ. Astron. Soc. Pac. **97**, 274 (1985).

Translated by V. Astakhov

The Orbit of the Nearby Low-Mass Binary Gliese 600

A. A. Tokovinin[1], Yu. Yu. Balega[2*], K.-H. Hofmann[3], and G. Weigelt[3]

[1] Sternberg Astronomical Institute, Universitetskiĭ pr. 13, Moscow, 119899 Russia
[2] Special Astrophysical Observatory, Russian Academy of Sciences,
Nizhniĭ Arkhyz, Stavropolskiĭ kraĭ, 357147 Russia
[3] Max-Planck-Institut für Radioastronomie, Bonn, 53121 Germany
Received April 5, 2000

Abstract—We have computed a combined spectroscopic–interferometric orbit for the nearby binary Gliese 600 discovered by us. The orbital period is 2.78 years, and the semimajor axis is 100 mas (0.1″). Its M0 V components are almost identical and have a mass of $0.5 M_\odot$. The mass ratio is uncertain because of the low radial-velocity semiamplitude (7 km s^{-1}) associated with the low orbital inclination (37°). The orbital parallax of the binary (52 ± 11 mas) matches its dynamical and photometric parallaxes but differs significantly from the Hipparcos parallax (44.3 ± 1.6) mas; the latter was probably distorted by the orbital motion that was not taken into account. © 2000 MAIK "Nauka/Interperiodica".

INTRODUCTION

Object no. 600 in the Catalogue of Nearby Stars (Gliese 1969), Gl 600, is an unremarkable star of the 9th magnitude, also known as BD+11°2874 or HIP 77725. Its coordinates are $15^{\rm h}52^{\rm m}08^{\rm s}$ and $+10°52'18''$ (2000.0), the magnitudes are $m_V = 9.38$ and $m_B = 10.78$, and the spectral type is K7 V. However, judging by the color index and luminosity, which is determined below, its spectral type is most likely M0 V.

In 1986, this star was included in our program of a radial-velocity survey of nearby K and M dwarfs with a correlation spectrometer (Tokovinin 1988; 1992a). In the former paper, the radial velocity was recognized to be constant. Subsequently, it emerged that, although velocity variations were actually barely detectable, the contrast and width of the correlation profile varied, suggesting the presence of a double-lined, low-amplitude spectroscopic binary. Tokovinin (1992a) estimated the orbital period in order of magnitude to be 200 days. We now know it to be a factor of 5 longer.

Several new spectroscopic binaries from the solar neighborhood were observed in 1989–1990 with a speckle interferometer on the 6-m telescope. These also included Gl 600, which was first resolved as a close (77 mas) interferometric pair by Balega *et al.* (1991). Apart from radial velocities, the speckle measurements served as a basis for determining the orbit, which is presented here.

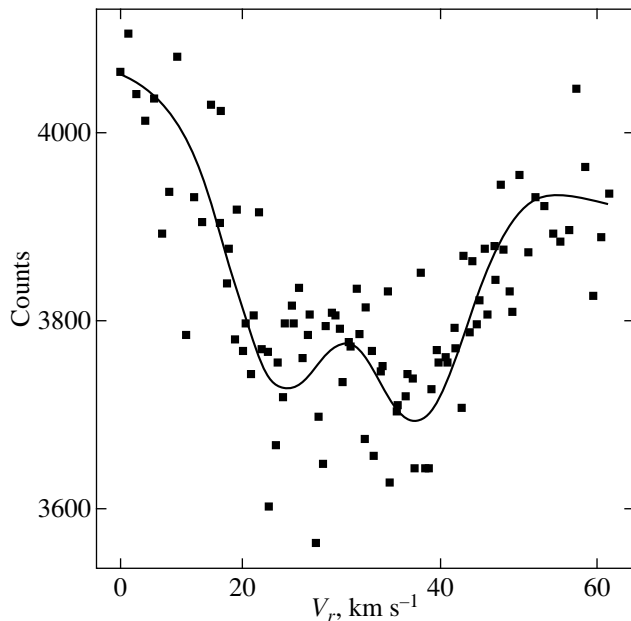* E-mail address for contacts: balega@sao.ru

INPUT DATA

Radial velocities of Gl 600 were measured in 1986–1998 using a correlation radial-velocity meter (RVM) (Tokovinin 1987) on various telescopes with apertures from 0.6 to 1.25 m in Crimea, Moscow, Abastumani, and at Maidanak. The RVM accuracy reaches 0.3 km s^{-1}, but, in our case, it was lower because the object was faint and the profile contrast was low.

With the FWHM of the RVM instrumental profile being 14.5 km s^{-1}, we have never been able to completely resolve the components' profiles. In order to determine their radial velocities, we have to fix the FWHM and contrast of the components' profiles and to fit the observations by their sum. An example of such a fit is given in Fig. 1. For both components, we assumed the profile parameters to be the same: a FWHM of 15 km s^{-1} and a contrast of 7%. The radial-velocity semiamplitudes determined under these assumptions were found to be 6.6 and 7.0 km s^{-1}. Slightly different semiamplitudes are obtained for different profile parameters. For example, the semiamplitudes at contrasts of 8 and 6% are 5.9 and 8.0 km s^{-1}, respectively, resulting in an implausibly low mass ratio. Thus, one of the sources of uncertainty in the spectroscopic orbital elements is related to the assumed parameters of the components profiles. Formal fitting errors, ranging from 0.5 to 1.5 km s^{-1}, are another source.

In 1986 and 1987, only the central part of the correlation profile was recorded, and these data proved to be unsuitable for reduction by the above method. The remaining spectroscopic observations in 1988–1998 span three complete orbital periods. Our radial-velocity measurements are given in Table 1. The first part of this

Fig. 1. An example of the correlation profile for Gl 600 recorded on August 5, 1992 (JD 2448840). The dots represents the number of photoevents in each bin; the solid line represents a double Gaussian fit with fixed FWHM and contrast. The profile contrast is about 10%. The total slope is instrumental in origin and is modeled by an additional parameter. The velocity zero point is arbitrary.
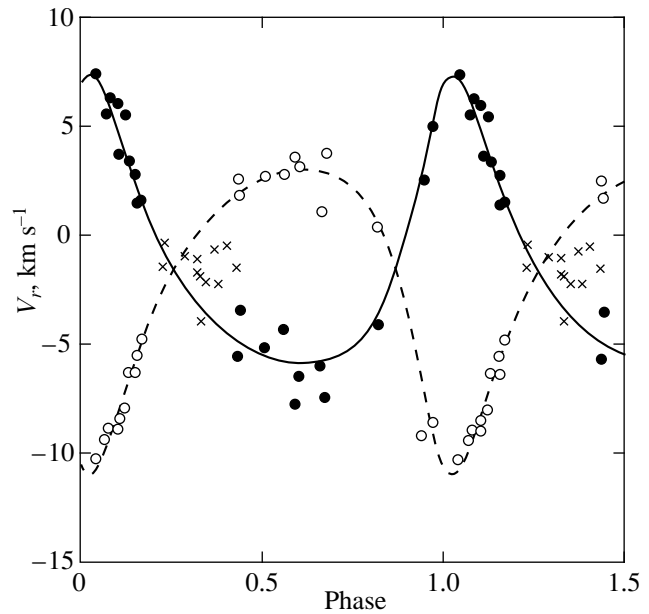
Fig. 2. The radial-velocity curve. The filled circles and the solid line represent the primary component; the open circles and the dashed line represent the secondary component; and the crosses indicate unresolved profiles, which were not used to determine the orbit.

table contains the results of our data reduction without the profiles being resolved, which were not used to compute the orbit. Its second part gives radial velocities, formal errors, and residuals to the orbit for the primary and secondary components.

In 1990, Gl 600 was first resolved with the 6-m telescope in a 600-nm filter during our speckle-interferometric survey of red dwarfs with variable radial velocities (Balega *et al.* 1991). It was included in the Third Catalog of Interferometric Measurements of Binary Stars (Hartkopf *et al.* 1998) under the name Bag 7. The observations performed three years later confirmed the identity of the interferometric and spectroscopic systems. In 1996, the binary was observed in the infrared (2.2 μm) using the NICMOS-3 detector (Balega *et al.* 2000). The speckle measurements of Gl 600 are given in Table 2. The magnitude difference between the components does not exceed $0\overset{m}{.}2$ in all bands.

THE ORBIT

We determined all ten elements of the combined spectroscopic–interferometric orbit by least squares using the ORBIT code (Tokovinin 1992b). The weights are inversely proportional to the measurement errors. The speckle-measurement errors in angle and distance were taken to be 3 mas. During the final adjustment, the weights were renormalized in such a way that the *S/N* ratio was equal to unity for each of the four types of data (primary velocity, secondary velocity, position

angles, and distances). Thus, the contribution of each type of data to the general solution corresponds to their quality. Figure 2 shows radial-velocity curves; the interferometric measurements and orbit projection onto the plane of the sky are shown in Fig. 3. Note the extremely small errors of the speckle measurements.
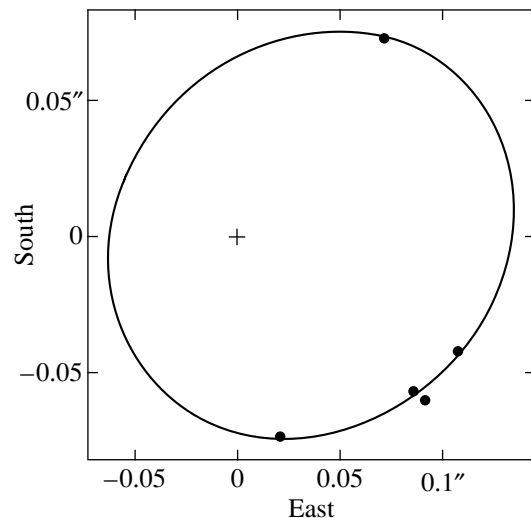
Fig. 3. Projection of the Gl 600 orbit onto the plane of the sky. The dots represent interferometric measurements. The short rectilinear segments connect measurements with computed orbital positions. The primary component is marked by a cross at the coordinate origin.

Table 1. Radial velocities of Gl 600 and residuals to the orbit

A. Unresolved profiles

JD 2400000+	V_r, km s^{-1}	σ, km s^{-1}	JD 2400000+	V_r, km s^{-1}	σ, km s^{-1}
47204.494	−1.45	0.47	49028.538	−0.32	0.43
48074.375	−0.94	0.35	49124.355	−1.01	0.51
48111.295	−1.71	0.53	49149.366	−2.12	0.28
48117.292	−1.81	0.44	49172.353	−0.63	0.35
48118.327	−3.89	0.11	49206.322	−0.41	0.77
48167.154	−2.18	0.46	51055.238	−1.41	0.38

B. Resolved profiles and residuals to the orbit

JD 2400000+	V_{r_A}, km s^{-1}	σ_A, km s^{-1}	$(O{-}C)_A$, km s^{-1}	V_{r_B}, km s^{-1}	σ_B, km s^{-1}	$(O{-}C)_B$, km s^{-1}
47753.285	5.09	0.87	−0.32	−8.50	0.86	0.35
48345.450	−4.30	0.64	1.45	2.92	0.64	−0.03
48387.413	−6.47	0.82	−0.61	3.32	0.82	0.25
48460.305	−7.36	1.16	−1.61	3.87	1.18	0.92
48738.425	2.63	1.49	−0.68	−9.20	1.46	−2.57
48840.276	7.41	0.97	0.15	−10.19	0.99	0.62
49234.223	−5.59	0.55	−0.81	2.66	0.58	0.73
49240.219	−3.36	0.69	1.49	1.86	0.69	−0.14
49389.640	−7.72	1.10	−1.88	3.80	1.11	0.76
49463.438	−5.99	0.70	−0.20	1.18	0.85	−1.82
49893.358	6.35	0.88	0.44	−8.85	0.89	0.53
49913.318	6.09	0.94	1.14	−8.84	0.94	−0.47
49919.336	3.73	0.63	−0.92	−8.40	0.64	−0.35
49934.272	5.59	0.83	1.69	−7.91	0.83	−0.65
49944.262	3.51	0.78	0.10	−6.27	0.78	0.47
49980.226	1.67	0.72	−0.08	−4.67	0.73	0.31
50324.235	−5.13	0.58	0.34	2.77	0.58	0.11
50635.334	−4.00	0.72	−0.36	0.47	0.72	−0.25
50899.528	5.63	0.90	−0.65	−9.32	0.90	0.46
50977.321	2.86	0.75	0.33	−6.25	0.74	−0.44
50982.368	1.56	0.69	−0.74	−5.47	0.69	0.09

Table 2. Speckle measurements and their residuals

Epoch	θ	ρ	$(O{-}C)_\theta$, km s^{-1}	$(O{-}C)_\rho$, km s^{-1}	References
1990.2083	15.5°	0.077″	1.3	0.000	Balega *et al.* (1991)
1993.3491	56.4	0.109	−0.6	0.003	Balega *et al.* (1999)
1993.3516	56.2	0.103	−1.0	−0.003	Balega *et al.* (1999)
1996.2000	68.4	0.115	1.1	−0.001	Balega *et al.* (2000)
1997.3913	135.7	0.102	−0.4	0.000	Balega *et al.* (1999)

Elements of the combined orbit and their errors are given in Table 3. Also given here are errors of unit weight for each type of data, orbital masses, and orbital parallaxes. Recall that, according to recommendations of the International Astronomical Union, the masses and parallaxes inferred from combined spectroscopic–visual orbits are called so. The relatively low accuracy of the orbital masses can be explained by the low orbital inclination i, because the masses are proportional to $\sin^3 i$.

Knowing the orbit, we again reduced all correlation profiles as single ones in the hope of finding variations in the mean radial velocity. Having fixed all elements except K_1, we obtained $K_1 = 0.58 \pm 0.46$ km s^{-1}; i.e., there are no statistically significant variations. This suggests that the components' magnitudes are almost

Table 3. Orbital elements for Gl 600

Element	Value	Error
P, days	1014.5	3.0
T, JD	2450828.1	11.2
e	0.367	0.017
a''	0.100	0.004
$\Omega°$	286.9	2.9
$\omega°$	339.6	4.9
$i°$	37.9	3.7
K_1, km s^{-1}	6.64	0.28
K_2, km s^{-1}	7.03	0.27
V_0, km s^{-1}	−1.52	0.11
σ_A, km s^{-1}	0.89	
σ_B, km s^{-1}	0.65	
σ_ρ''	0.002	
$\sigma_\theta°$	0.9	
$M_A/M_\odot$	0.48 ± 0.13	
$M_B/M_\odot$	0.46 ± 0.12	
π_{orb}, mas	52 ± 11	

equal, which is also confirmed by speckle interferometry.

DISCUSSION

Astrometric parameters of Gl 600, in particular, its parallax $\pi_{Hip} = 44.3 \pm 1.6$ mas, were measured during the Hipparcos experiment (ESA 1997). With this parallax and our orbital elements, the sum of the masses is $1.53 \pm 0.27 M_\odot$, which is implausibly large for a pair of M0 V dwarfs. Failure to take into account the binary's orbital motion during Hipparcos data reduction probably resulted in the erroneous parallax, which was also noted in several other similar cases.

The color index $B-V=1.40$ corresponds to the spectral type M0 V. The standard mass of such stars is $0.51 M_\odot$ (Lang 1992). Taking this value for each component, we obtain a dynamical parallax of 50 mas; i.e., it essentially matches the orbital parallax. By contrast to the orbital parallax, the dynamical parallax does not depend on the measured radial-velocity semiamplitudes, which are not too reliable, and depends only slightly on the assumed mass. We therefore have no doubt that the Hipparcos parallax is erroneous.

Thus, we take the dynamical parallax as the most reliable estimate of the distance to Gl 600, which is, hence, 20 pc. With the components magnitudes being the same, their absolute magnitudes are $V = 8^m.62$, cor-

responding to the luminosity of M0 V dwarfs (Lang 1992). Consequently, the components of Gl 600, to all appearances, satisfy the standard mass–luminosity relation. Refining the orbital elements will allow the errors in the parallax and mass to be considerably reduced, and a comparison with the mass–luminosity relation will be more significant. A more accurate determination of this relation in the range of low masses is still of current interest.

Knowing the distance to the object, the radial velocity of its center of mass, and its proper motion (as inferred from Hipparcos data), we can easily calculate the spatial velocity components in Galactic coordinates: $U, V, W = 2.6, -31.7, 7.2$ km s^{-1}. These values are typical of the Galactic disk population.

A further study of the binary Gl 600 is primarily associated with a refinement of its spectroscopic elements. A spectral resolution of no less than 40000 is required to reliably resolve its components. The inferred orbital elements will help plan future observations.

REFERENCES

1. I. I. Balega, Yu. Yu. Balega, V. A. Vasyuk, and A. A. Tokovinin, Pis'ma Astron. Zh. **17**, 530 (1991) [Sov. Astron. Lett. **17**, 226 (1991)].
2. I. I. Balega, Y. Y. Balega, A. F. Maksimov, *et al.*, Astron. Astrophys., Suppl. Ser. **140**, 287 (1999).
3. I. I. Balega, Yu. Yu. Balega, K.-H. Hofmann, *et al.*, Pis'ma Astron. Zh. **25**, 910 (1999) [Astron. Lett. **25**, 797 (1999)].
4. W. Gliese, *Catalogue of Nearby Stars* (Karlsruhe, G. Braun, Heidelberg, 1969), Veroef. Astron. Rechen-Instituts, Heidelberg, No. 22 (1969).
5. W. I. Hartkopf, H. A. McAlister, and B. D. Mason, *Third Catalog of Interferometric Measurements of Binary Stars*, CHARA Contrib. No. 4 (Georgia State Univ., Atlanta, 1998).
6. *Hipparcos, Venice'97: Presentation of the Hipparcos and Tycho Catalogues and Results of the Hipparcos Space Astromerty Mission*, Ed. by B. Battrick (European Space Agency, Noordwijk, 1997), SP 1200.
7. K. R. Lang, *Astrophysical Data: Planets and Stars* (Springer-Verlag, New York, 1992).
8. A. A. Tokovinin, Astron. Zh. **64**, 196 (1987) [Sov. Astron. **31**, 98 (1987)].
9. A. A. Tokovinin, Astrofizika **29**, 297 (1988).
10. A. A. Tokovinin, Astron. Astrophys. **256**, 121 (1992a).
11. A. A. Tokovinin, in *Complementary Approaches to Double and Multiple Star Research: Proceedings of the 135th Cool. of International Astronomical Union*, Ed. by H. A. McAlister and W. I. Hartkopf, Astron. Soc. Pac. Conf. Ser. **32**, 573 (1992b).

Translated by V. Astakhov

Tests for Spatial Isotropy of Three Thousand Gamma-Ray Bursts Found in BATSE Archival Data

Ya. Yu. Tikhomirova[1, 2*] and B. E. Stern[1, 2, 3]

[1] *Astrospace Center, Lebedev Physical Institute, Russian Academy of Sciences, Profsoyuznaya ul. 84/32, Moscow, 117810 Russia*
[2] *Stockholm Observatory, Stockholm, Sweden*
[3] *Institute for Nuclear Research, Russian Academy of Sciences, prospekt Shestidesyatiletiya Oktyabrya 7a, Moscow, 117312 Russia*
Received July 5, 1999; in final form, November 1, 1999

Abstract—We apply isotropy tests to our new uniform catalog of cosmic gamma-ray bursts (GRBs) (Stern and Tikhomirova 1999). The catalog contains trigger and nontrigger bursts found in 1024-ms BATSE records over seven years. Based on this catalog, we confirm isotropy of the GRB spatial distribution for a sample that surpasses previous samples in size (2934 bursts) and in achieved threshold (fluxes down to 0.1 phot. cm^{-2} s^{-1}, which is a factor of ~2 lower than the BATSE trigger threshold). We also confirm that there is no excess of bursts toward the galaxy M 31. © *2000 MAIK "Nauka/Interperiodica".*

Keywords: *gamma-ray bursts*

1. INTRODUCTION

Whether all gamma-ray bursts (GRBs) arrive from cosmological distances or, apart from the cosmological population, there is a population of GRB sources of a different nature, in particular, a population of sources forming a halo around our Galaxy at distances up to hundreds of kpc from its center (Shklovskiĭ and Mitrofanov 1985; Paczynski 1991), has been an open question ever since evidence for the cosmological nature of several GRBs emerged (Djorgovski *et al.* 1998).

The existence of GRB sources comprising the Galactic halo population suggests the existence of an analogous halo population around the Andromeda galaxy (M 31), the nearest galaxy similar to ours. Detecting an excess of bursts toward M 31 would prove the existence of such a population, while isotropy of the observed GRB distribution constrains the Galactic halo population.

Of special interest in testing isotropy in general and an excess of events toward M 31 in particular is our new catalog of GRBs (Stern and Tikhomirova 1999; below referred to as ST99). This is the largest (to date) uniform catalog of GRBs with fluxes down to 0.1 phot. cm^{-2} s^{-1} found in records of the US Burst And Transient Source Experiment (BATSE) (Fishman 1992).
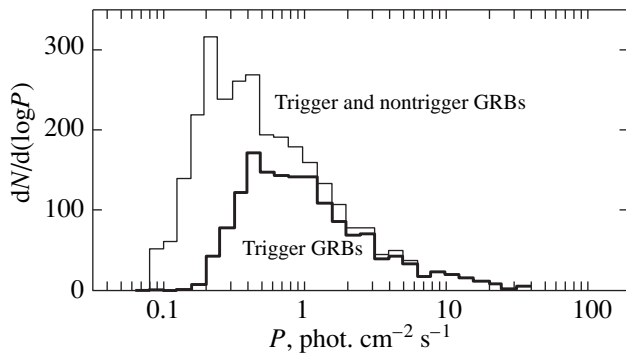
2. THE DATA

The ST99 new catalog of GRBs was compiled by searching for nontrigger bursts in BATSE archival records (Stern *et al.* 1999a, 1999b, 1999c) and represents a combined catalog of trigger and nontrigger GRBs. The records contain data from continuous BATSE observations onboard the CGRO orbiting observatory in the energy range 20–600 keV with a time resolution of 1024 ms.

By trigger bursts we mean the GRBs that were detected and identified during the BATSE experiment and included in the BATSE catalog (Meegan *et al.* 1999). Nontrigger bursts are statistically significant GRBs that were not caused BATSE triggering; consequently, they were not detected during the BATSE experiment either because of insufficient intensity or for other reasons: because of the smooth rise, high background, and falling within periods of data transfer from the satellite to the Earth.

All the bursts included in the ST99 catalog were found by scanning archival records of observations and by subsequent data reduction using the same procedure. Thus, the catalog is homogeneous. Details of this search were described by Stern *et al.* (1999a, 1999b, 1999c). Trigger bursts were identified by using the BATSE catalog (Meegan *et al.* 1999). Some of the trigger bursts (~24%) were not found in the search: they were too short to be detected with a 1024-ms resolution or fell within breaks of records in this type of data. Trigger bursts that were not found by scanning were not included in the catalog for the sake of its homogeneity.

* E-mail address for contacts: jana@anubis.asc.rssi.ru

Fig. 1. The peak-flux distribution of GRBs from the ST99 catalog.

Since the time resolution of the data used is low, the catalog does not lend itself to studying short bursts.

As of August 25, 1999, the catalog contains 1581 trigger and 1353 nontrigger (2934 in total) GRBs found in records over seven years of observations (from April 21, 1991, until October 2, 1997, and from March 19, 1998, until October 17, 1998); it is thus the largest GRB catalog to date. The current electronic BATSE catalog for this time includes more than ~2000 GRBs [while the published catalog by Paciesas *et al.* (1999) includes a mere 1637 bursts). The supplement to it in the form of a catalog of nontrigger GRBs compiled by Kommers *et al.* (1998), together with the trigger

bursts found during the data reduction, numbers 2265 bursts (873 of them are nontrigger ones).

The detected nontrigger bursts, which were included in the ST99 catalog along with the trigger ones, extended the sample of known GRBs to fluxes of 0.1 phot. $cm^{-2} s^{-1}$ and probably made more distant burst sources accessible for investigation. The increased number of known GRBs allows their statistical properties, in particular, the pattern of their spatial distribution, to be analyzed with greater significance.

Figure 1 shows the peak-flux distribution of bursts. We give a diagram for all bursts from the catalog and separately for trigger bursts.

The spatial distribution of GRBs from the ST99 catalog is mapped in Fig. 2. Maps of the nontrigger and all (trigger and nontrigger) bursts from the catalog are shown separately.
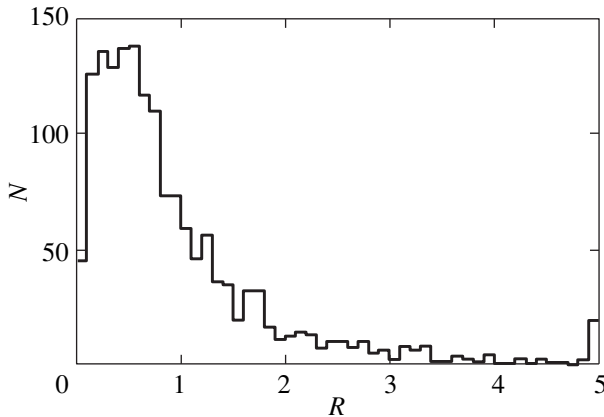
Stern *et al.* (1999a, 1999b, 1999c) used in their search a signal fitting technique for a simultaneous determination of both the locations and the light curve as a pure signal. They fitted a light curve that yielded a minimum χ^2 when compared with the observed signal for the second and third energy channels (50–300 keV) in all eight BATSE detectors for each time bin. The burst location and spectrum are varied. The error region in the catalog is the distance from the point at which χ^2 is at a minimum when fitting the photon flux and the burst location to the farthest point of the contour corresponding to 1σ.
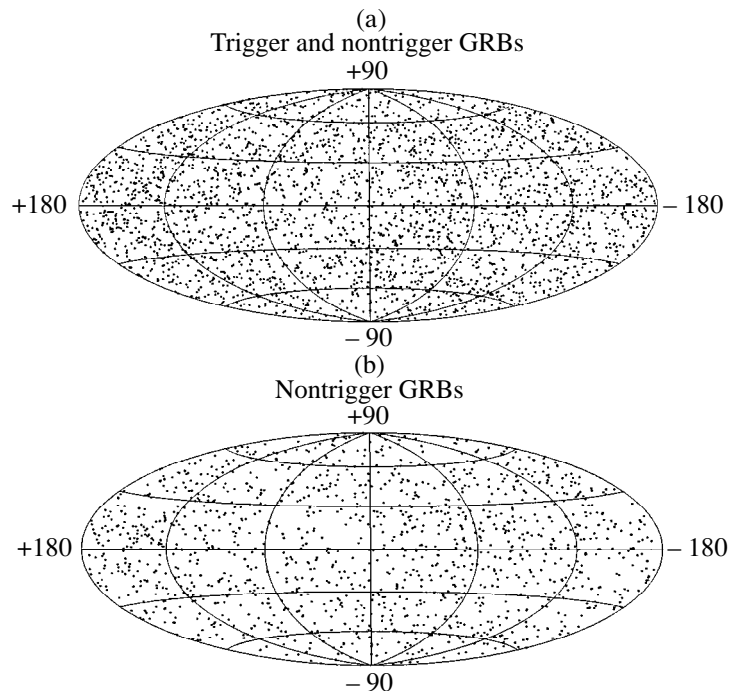
Fig. 2. The sky distribution of GRBs from the ST99 catalog in Galactic coordinates in Gummer projection: (a) all bursts (2934) and (b) only nontrigger bursts (1353).
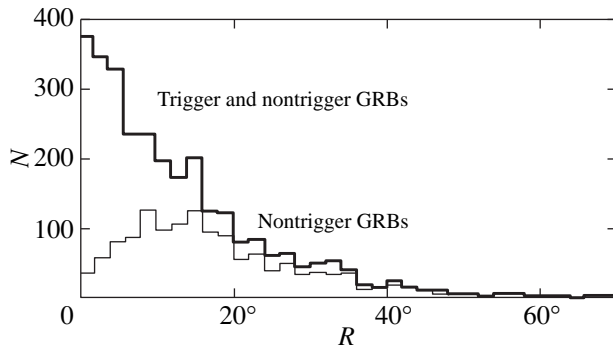
Fig. 3. The angular distribution of location errors from the ST99 catalog in degrees: the heavy and thin lines represent all bursts and only the nontrigger bursts, respectively.

Fig. 4. The distribution of discrepancies between the GRB locations determined during the BATSE experiment and in the search by Stern *et al.* (1999a, 1999b, 1999c) in standard deviations σ.

In general, the error region is not circular. Apart from the statistical error, the systematic errors associated with inaccuracy of the detector response matrix and the fitting photon spectrum, as well as non-Poisson background fluctuations, contribute to the location error.

Figure 3 shows the distribution of location errors for the ST99 catalog. The location error is less than 10° for only half of all the bursts from the catalog and less than 20° for 80% of the bursts. The nontrigger bursts, as mostly weaker ones, generally have larger location errors. However, such a low location accuracy is quite sufficient for a statistical analysis of the spatial distribution and the isotropy tests used here (see Subsection 3.2).

It should be noted that GRBs are rather difficult to locate (see, e.g., Briggs *et al.* 1999). The programs of determining the locations and contours of the error region used in the BATSE experiment and in Stern *et al.* (1999a, 1999b, 1999c) are complex. Their algorithms differ in spectrum-fitting method, and both are imper-

fect [see, e.g., Subsection 4.1 in Paciesas *et al.* (1999)]. Figure 4 shows discrepancies between the burst locations from the last BATSE 4Br catalog (Paciesas *et al.* 1999) and the ST99 catalog. The scatter is significant, although most deviations between the locations lie within 1σ.

In their search for nontrigger bursts, Stern *et al.* (1999a, 1999b, 1999c) used a method that involved "planting" artificial test bursts in records of observations to estimate the efficiency of burst detection and allowance for some selective effects. The planted test bursts were made from known trigger bursts that were detected during the BATSE experiment and randomly added to records of observations. Without revealing its artificial nature, the planted bursts, along with the actual ones, were subjected to the same data reduction technique and identified only after completion of the data reduction.

Test bursts were planted with a higher rate (a larger number of bursts per unit time) than the rate with which actual bursts are detected; thus, the statistics of the test bursts found by scanning (4365 events) exceeds the statistics of the detected actual bursts (2934 events).

The locations of test bursts were randomly specified from the outset in accordance with an isotropic spatial distribution. The final distributions for test bursts exhibit all the systematic effects which the actual bursts found by Stern *et al.* (1999a, 1999b, 1999c) in their search are subjected to: these include both system peculiarities of the BATSE experiment (including nonuniform sky exposure) and flaws of the search itself.

3. ISOTROPY TESTS

3.1. The Tests

We see the following tests to be of current interest in testing the distribution of our new sample of GRBs for isotropy:

• the dipole moment **R** in an independent coordinate system defined as

$$\mathbf{R} = \frac{\sum \mathbf{r}_i}{N},\qquad(1)$$

where $\mathbf{r}_i$ is a unit vector directed toward the burst, and N is the number of bursts in the sample;

• its three components $R1$, $R2$, and $R3$ (in equatorial coordinates); and the statistics widely used previously (see, e.g., Briggs *et al.* 1994):

• $\langle\cos\theta\rangle$, where θ is the angle between the directions toward the Galactic center and the burst,

• $\langle\sin^2 b - 1/3\rangle$, where b is the Galactic latitude of the burst,

• $\langle\sin\delta\rangle$,

• $\langle\sin^2\delta - 1/3\rangle$, where δ is the burst declination. The latter characterize the dipole and quadrupole moments in Galactic and equatorial coordinates, respectively.

These statistics are sensitive to the anisotropies associated with the characteristic directions and planes of the coordinate systems used. The statistics $\langle\sin\delta\rangle$ and $\langle\sin^2\delta - 1/3\rangle$ test the anisotropy attributable to the Earth and can reveal systematic errors. Using the statistics $\langle\cos\theta\rangle$ and $\langle\sin^2b - 1/3\rangle$ was determined by the hypotheses of a Galactic origin for GRBs.

Confirmation of the cosmological hypothesis for the origin of GRBs (Djorgovski *et al.* 1998) makes the use of an independent coordinate system for isotropy tests of current interest [note, however, that this system was used well before this, for example, by Hartmann and Epstein (1989)].

The 4Br catalog of GRBs detected during the BATSE experiment uses Watson's (*W*) and Bingham's (*B*) statistics, which characterize the dipole and quadrupole moments in an independent coordinate system, respectively (Paciesas *et al.* 1999). An advantage of the *W* test is considered to be its independence of the number of sources *N* and the χ_3^2 probability density distribution. However, this test yields a scalar quantity and does not indicate the direction of a possible anisotropy. We therefore used a simpler, but more descriptive parameter—the dipole moment **R**.

The identification of GRB 980425 with a supernova (Sadler *et al.* 1998) suggests that some of the GRBs may be associated with supernovae in galaxies at redshifts $z \leq 0.01$. In this case, the super-Galactic plane can be felt in the sky distribution of GRBs, which was tested by using yet another statistics, $\langle\sin^2\gamma - 1/3\rangle$, where γ is the angle between the super-Galactic plane and the direction toward the burst.

3.2. Errors in the Quantities Used

The statistical errors are

$$\sigma = \frac{1}{\sqrt{3N}}, \qquad (2)$$

for the statistics $\langle\cos\theta\rangle$ and $\langle\sin\delta\rangle$, as well as the components of the dipole moment *R*1, *R*2, and *R*3;

$$\sigma = \frac{\sqrt{4}}{\sqrt{45N}}, \qquad (3)$$

for the statistics $\langle\sin^2b - 1/3\rangle$ and $\langle\sin^2\delta - 1/3\rangle$; and

$$\sigma = \frac{1}{\sqrt{N}}, \qquad (4)$$

for the magnitude of the dipole moment **R**. Here, *N* is the number of bursts in the sample (Briggs 1993).

The uncertainties introduced into the dipole and quadrupole moments by the location errors of the ST99 catalog are considerably smaller than the uncertainties that result from the sample being limited. As Monte Carlo simulations show, the uncertainties introduced by the location errors into the components of the dipole

Table 1. The isotropy tests

Statistics	Characteristic	Coordinate system	Expected value for BATSE exposure
R	Dipole	Independent	0.018*
*R*1			0.000
*R*2			0.000
*R*3			0.018
$\langle\cos\theta\rangle$	Dipole	Galactic	−0.009**
$\langle\sin^2b - 1/3\rangle$	Quadrupole	Galactic	−0.004**
$\langle\sin\delta\rangle$	Dipole	Equatorial	0.018**
$\langle\sin^2\delta - 1/3\rangle$	Quadrupole	Equatorial	0.024**

  * Magnitude of the vector.
** Paciesas *et al.* (1999).

moment in an independent coordinate system are 3.8×10^{-3} for the entire ST99 catalog and 7.1×10^{-3} for the nontrigger bursts, whereas the statistical errors are 1.1×10^{-2} and 1.8×10^{-2}, respectively.

The test for an excess of bursts toward the Andromeda galaxy is also efficient, despite the large location errors. We simulated the case where bursts in the M 31 halo give a uniform excess in the spatial distribution within a circle of radius 12°, 18°, and 25° in the sky around the direction toward M 31 over the remaining isotropic background by using the Monte Carlo method. Given the location errors of our catalog, 55, 66, and 74% of the bursts remain within 12°, 18°, and 25°, respectively; i.e., the excess is quite detectable. Actually, however, bursts in the M 31 halo must give an excess that is not uniform inside the circle but with a concentration of bursts toward the M 31 center; thus, the fraction of the remaining bursts must be even higher.

3.3. Comparative Quantities

For an isotropic distribution of GRB sources, the values of all tests in Table 1 are zero. However, because of the low, nearly equatorial orbit of the satellite on which the BATSE experiment was carried out and because of the varying ionospheric contribution to the background, the BATSE sky exposure is nonuniform (in particular, the nonuniformity in δ is especially large) (Paciesas *et al.* 1999). The last column of Table 1 gives the values expected for isotropy of the observed sources with allowance for the BATSE exposure.

However, other systematic effects could result from a nonuniform burst selection. One of such effects is caused by solar activity, Cyg X-1, and hard Galactic X-ray sources, which reduces the efficiency of GRB detection by its direction. These effects are more difficult to take into account than the exposure, and they are generally disregarded in such problems.

Table 2. Results of the isotropy tests

Statistics	Expected value for BATSE exposure	4Br catalog*	ST99 catalog		
			test	trigger, nontrigger	nontrigger
$\|\mathbf{R}\|$	0.018	0.029 ± 0.025	0.024 ± 0.015	0.031 ± 0.018	0.031 ± 0.027
$R1$	0.000	0.005 ± 0.014	-0.020 ± 0.009	-0.015 ± 0.011	-0.022 ± 0.016
$R2$	0.000	0.015 ± 0.014	0.008 ± 0.009	0.020 ± 0.011	0.022 ± 0.016
$R3$	0.018	0.024 ± 0.014	0.009 ± 0.009	0.018 ± 0.011	0.006 ± 0.016
$\langle \cos\theta \rangle$	-0.009	-0.025 ± 0.014	-0.010 ± 0.009	-0.025 ± 0.011	-0.020 ± 0.016
$\langle \sin^2 b - 1/3 \rangle$	-0.004	-0.001 ± 0.007	-0.006 ± 0.005	-0.007 ± 0.005	-0.005 ± 0.008
$\langle \sin\delta \rangle$	0.018	0.024 ± 0.014	0.009 ± 0.009	0.018 ± 0.011	0.006 ± 0.016
$\langle \sin^2\delta - 1/3 \rangle$	0.024	0.025 ± 0.007	0.027 ± 0.005	0.024 ± 0.005	0.030 ± 0.008

* Paciesas *et al.* (1999).

In the ST99 catalog, we overcame this problem by using planted test bursts (see section 2), which exhibit the same systematic deviations from isotropy as those expected for actual bursts. The results of our isotropy tests for planted bursts are presented in column 4 of Table 2.

Since the sample of planted bursts is relatively small (4365 events), we use both the values of the isotropy tests for planted bursts and the calculated values expected for isotropy with allowance for the BATSE exposure as comparative quantities.

3.4. Results of the Tests

Table 2 lists the inferred magnitudes of the dipole moment $\mathbf{R}$, its three components $R1$, $R2$, and $R3$, as well as the statistics $\langle \cos\theta \rangle$, $\langle \sin^2 b - 1/3 \rangle$, $\langle \sin\delta \rangle$, and $\langle \sin^2\delta - 1/3 \rangle$ for the ST99 catalog: column 5 for the entire catalog and column 6 for the nontrigger bursts separately. For comparison, the table gives the values expected for a uniform isotropic distribution with allowance for the BATSE exposure (column 2), the values for the 4Br catalog (column 3), and the values for the planted test bursts of the ST99 catalog (column 4).

Table 3. Deviations of the test values from the expected ones

Statistics	4Br catalog	ST99 catalog			
		trigger, nontrigger		nontrigger	
	σ/B.e.	σ/B.e.	σ/t.b.	σ/B.e.	σ/t.b.
$\mathbf{R}$	0.5**	1.9**	0.5**	1.5**	0.2**
$\langle \cos\theta \rangle$	-1.1*	-1.5	-1.1	-0.7	-0.5
$\langle \sin^2 b - 1/3 \rangle$	$+0.4$*	-0.5	-0.2	-0.1	$+0.1$
$\langle \sin\delta \rangle$	$+0.4$*	-0.0	$+0.6$	-0.8	-0.2
$\langle \sin^2\delta - 1/3 \rangle$	$+0.1$*	$+0.0$	-0.4	$+0.7$	$+0.3$

* Paciesas *et al.* (1999).
** Deviation of the vector.

The values of the tests are given with the rms errors defined by (2)–(4).

Table 3 shows deviations of the observed values of the tests from the expected ones. For the ST99 and 4Br catalogs, the table gives deviations of the observed values from the expected ones for a uniform isotropic distribution with allowance for the BATSE exposure in σ designated σ/B.e. and defined by (2)–(4). For the ST99 catalog, it also lists deviations of the observed values from the values for the test bursts in σ designated σ/t.b. and defined as

$$\sigma = \sqrt{\sigma^2_{\text{test burst}} + \sigma^2_{\text{act. burst}}}, \tag{5}$$

where $\sigma_{\text{test burst}}$ and $\sigma_{\text{act. burst}}$ are the statistical errors for the test and actual bursts of the catalog, respectively. The deviations are given both for the entire ST99 catalog and for the nontrigger bursts separately. For the dipole moment $\mathbf{R}$, the table gives the deviation of the vector

$$\frac{|\mathbf{R} - \mathbf{R}_{\text{comp}}|}{\sigma} \tag{6}$$

$$= \frac{\sqrt{(R1 - R1_{\text{comp}})^2 + (R2 - R2_{\text{comp}})^2 + (R3 - R3_{\text{comp}})^2}}{\sigma},$$

where σ is defined by (4) and (5) for σ/B.e. and σ/t.b., respectively.

Note that the magnitude of the dipole moment in an independent coordinate system was calculated for the 4Br catalog (Paciesas *et al.* 1999) separately, because it is not given in this catalog.

The vector of the dipole moment $\mathbf{R}$ exhibits the largest deviation from the expected values for the BATSE exposure: 1.9σ for the entire catalog and 1.5σ for the nontrigger bursts. However, the deviations from the values for the test bursts are small: 0.5σ and 0.2σ, respectively.

The dipole direction for the entire catalog is $\alpha = 126°$ and $\delta = 35°$, which roughly corresponds to the direction of the Galactic anticenter. The direction for the nontrigger bursts is $\alpha = 135°$ and $\delta = 10°$. The dipole direction for the test bursts is $\alpha = 159°$ and $\delta = 23°$.

The deviations of all tests from the values for the test bursts do not exceed 1.1σ.

The almost significant (1.9σ) deviation of the vector of the dipole moment from that expected for the BATSE exposure and the 1.5σ deviation for $\langle\cos\theta\rangle$ can be explained by selection effects in the search by Stern *et al.* (1999a, 1999b, 1999c). The effect is directly confirmed by the test bursts. As was already mentioned above, some bursts may be lost due to hard Galactic X-ray sources, which determines the anisotropy of the dipole moment toward the Galactic anticenter. The distribution in $\langle\cos\theta\rangle$ for the bursts of the catalog in Fig. 5 exhibits a small deficit of bursts toward the Galactic center. The test bursts give a dipole, which is also directed to the hemisphere opposite to the Galactic center.

The value of the test $\langle\sin^2\gamma - 1/3\rangle = -0.016 \pm 0.006$, which is -1.2σ of that expected for isotropy and suggests that there is no concentration to the super-Galactic plane.

Thus, the results for the ST99 catalog confirm that the spatial distribution of GRBs is isotropic.

3.5. Testing an Excess Toward the Galaxy M 31

Detection of an excess of GRBs toward the Andromeda galaxy (M 31) would prove that, apart from the cosmological population, a population of bursters exists in the Galactic halo.

GRB sources can constitute a halo around the Galaxy within hundreds of kpc from its center (see, e.g., Loredo and Wasserman 1998) with a spatial density of sources falling off to the periphery (such a halo can be produced, for example, by neutron stars). Since the spatial distribution for the sample of GRBs under study is isotropic (see subsection 3.4), the halo size cannot exceed considerably half the distance to the Andromeda galaxy, which is 670 kpc. Thus, the maximum effective opening of the cone in which an excess of sources could be expected is $\sim 25°$.

Since the halo size is not known, we tested an excess of bursts for three radii around M 31: $12°$, $18°$, and $25°$. An excess was tested both for the entire catalog and for weak bursts with fluxes below 0.4 phot. cm^{-2} s^{-1}. The catalog contains 1311 bursts with fluxes below 0.4 phot. cm^{-2} s^{-1}; thus, they account for slightly less than half of the total number.

The results of our test of an excess toward M 31 are summarized in Table 4. The second column gives the expected number of bursts within the cone of the corresponding radius around the direction of M 31 for an isotropic sky distribution of GRB sources with allowance for the BATSE exposure; the third and fourth columns list, respectively, the observed number of bursts accord-
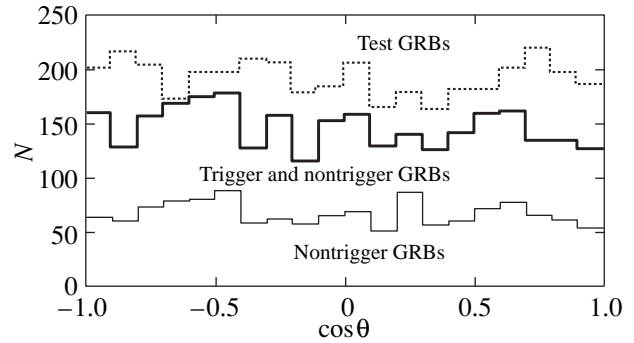
Fig. 5. The distribution of GRBs from the ST99 catalog in $\cos\theta$. The heavy, thin, and dotted lines represent all (trigger and nontrigger) bursts, only the nontrigger bursts, and the test bursts, respectively.
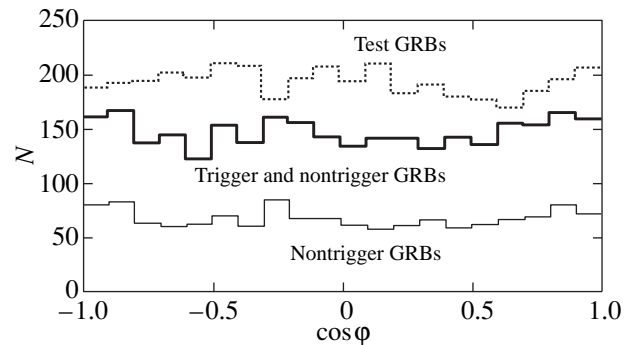
Fig. 6. The distribution of GRBs from the ST99 catalog in $\cos\varphi$. The notation is the same as in Fig. 5.

ing to the ST99 catalog and the deviation of the observed number from the expected one.

An excess, within 1.5σ, is detected only for the $12°$ radius and is not statistically significant.

The distribution of GRBs from the catalog in $\cos\varphi$ (Fig. 6), where φ is the angle between the M 31 and burst directions, clearly shows that there is no statistically significant excess.

Table 4. Excess toward M 31

Radius of cone around M 31	Expected number of bursts	Observed number of bursts	Deviation from expected number
Inferred from all 2934 bursts of ST99 catalog			
12°	34	41	1.2σ
18°	75	73	−0.2σ
25°	144	146	0.2σ
Inferred from 1311 weak bursts of ST99 catalog			
12°	15	21	1.5σ
18°	34	34	0σ
25°	64	63	−0.1σ

4. CONCLUSION

Our results confirm the absence of any anisotropy in the sky distribution of GRBs with an almost twice as large sample and half as low burst detection threshold as they were previously owing to the ST99 new catalog.

We have tested isotropy by using the dipole and quadrupole moments in Galactic and equatorial coordinates, as well as the dipole in an independent coordinate system, which can indicate the direction of a possible anisotropy, and the quadrupole in super-Galactic coordinates. The 1.9σ deviation of the magnitude of the dipole (directed away from the Galactic center) from the expected one is not statistically significant. In addition, it can be explained by selection effects measured using "planted" test bursts.

We have also separately tested and confirmed the absence of any excess of bursts toward the Andromeda galaxy.

Isotropy, which was confirmed for our new sample of known GRBs, must place more stringent constraints on Galactic models of GRBs [see, e.g., Loredo and Wasserman (1998) for a constraining technique] and, in particular, must determine the largest allowable fraction of Galactic GRBs in the total number of observed GRBs.

REFERENCES

1. M. Briggs, Astrophys. J. **407**, 126 (1993).
2. M. S. Briggs, W. S. Paciesas, M. N. Brock, *et al.*, *Gamma Ray Bursts,* Ed. By G. J. Fishman, AIP Conf. Proc., No. 307, 44 (1994).
3. M. S. Briggs, G. N. Pendleton, R. M. Kippen, *et al.*, astro-ph9901111; Astrophys. J., Suppl. Ser. **122**, 503 (1999).
4. S. G. Djorgovski, S. R. Kulkarni, D. A. Frail, *et al.*, Am. Astron. Soc. Meeting **192**, 3310 (1998).
5. G. J. Fishman, in *Compton Gamma Ray Observatory*, Ed. By M. Friedlander, N. Gehrels, and D. J. Macomb, AIP Conf. Proc., No. 280, 669 (1992).
6. D. Hartmann and R. I. Epstein, Astrophys. J. **346**, 960 (1989).
7. J. M. Kommers, W. H. C. Lewin, C. Kouveliotou, *et al.*, http://space.mit.edu/BATSE (1998).
8. T. J. Loredo and I. M. Wasserman, Astrophys. J. **502**, 75 (1998).
9. C. A. Meegan, G. N. Pendleton, M. S. Briggs, *et al.*, http://gammaray.msfc.nasa.gov/batse/grb/data/catalog (1999).
10. W. S. Paciesas, C. A. Meegan, G. N. Pendleton, *et al.*, astro-ph9903205; Astrophys. J., Suppl. Ser. **41** (3), 465 (1999).
11. B. Paczynski, Acta Astron. **41** (3), 157 (1991).
12. E. M. Sadler, R. A. Stathakis, B. J. Boyle, *et al.*, IAU Circ., No. 6901 (1998).
13. I. S. Shklovskiĭ and I. G. Mitrofanov, Mon. Not. R. Astron. Soc. **212**, 545S (1985).
14. B. Stern and Ya. Tikhomirova, http://www.astro.su.se/groups/head/grb.archive (1999), Preprint No. 48, FIAN (Lebedev Physical Institute, Russian Academy of Sciences, Moscow, 1999).
15. B. Stern, Ya. Tikhomirova, M. Stepanov, *et al.,* astro-ph9903094; Astron. Astrophys., Suppl. Ser. **138**, 413S (1999a).
16. B. Stern, Ya. Tikhomirova, M. Stepanov, *et al.*, Astron. Soc. Pac. Conf. Ser. **190**, 253 (1999b).
17. B. Stern, Ya. Tikhomirova, M. Stepanov, *et al.*, Preprint No. 43 FIAN (Lebedev Physical Institute, Russian Academy of Sciences, Moscow, 1999); accepted to Astrophys. J. Letters (1999c).

Translated by V. Astakhov

The Temperature of Nonspherical Circumstellar Dust Grains[1]

N. V. Voshchinnikov* and D. A. Semenov

Sobolev Astronomical Institute, St. Petersburg State University, Bibliotechnaya pl. 2, St. Petersburg–Peterhof, 198904 Russia

Received January 28, 2000

Abstract—The temperatures of prolate and oblate spheroidal dust grains in the envelopes of stars of various spectral types are calculated. Homogeneous particles with aspect ratios $a/b \leq 10$ composed of amorphous carbon, iron, dirty ice, various silicates, and other materials are considered. The temperatures of spherical and spheroidal particles were found to vary similarly with particle size, distance to the star, and stellar temperature. The temperature ratio T_d(spheroid)/T_d(sphere) depends most strongly on the grain chemical composition and shape. Spheroidal grains are generally colder than spherical particles of the same volume; only iron spheroids can be slightly hotter than iron spheres. At $a/b \approx 2$, the temperature differences do not exceed 10%. If $a/b \gtrsim 4$, the temperatures can differ by 30–40%. For a fixed dust mass in the medium, the fluxes at wavelengths $\lambda \gtrsim 100$ are higher if the grains are nonspherical, which gives overestimated dust masses from millimeter observations. The effect of grain shape should also be taken into account when modeling Galactic-dust emission properties, which are calculated when searching for fluctuations of the cosmic microwave background radiation in its Wien wing. © *2000 MAIK "Nauka/Interperiodica"*.

Keywords: *interstellar medium, circumstellar shells*

1. INTRODUCTION

The observed infrared and submillimeter emission from interstellar clouds, circumstellar envelopes, and galaxies is generally thermal emission of dust heated by stellar radiation or shock waves. When infrared spectra of these objects are computed, the dust temperature must be calculated. This temperature is also used to determine the mass and thermal balance of the matter in various objects and is important for the formation of molecules on the grain surfaces.

Calculations of the interstellar dust temperature were initiated in the 1940s [see Van de Hulst (1949) for a discussion]. The equilibrium temperature of spherical dust grains is commonly considered (see, e.g., Mathis *et al.* 1983). However, it has been known for fifty years (since the discovery of interstellar polarization by Hiltner (1949), Hall (1949), and Dombrovskiĭ (1949) that there are nonspherical aligned particles in the interstellar medium.

Nonspherical particles appear to be also present in circumstellar dust shells. The variations in the position angle of linear polarization with time and wavelength observed in red giants provide circumstantial evidence for this (Dyck and Jennings 1971; Shawl 1975). Even

after correction for the interstellar polarization, the position-angle difference in the blue and in the red can reach 20–60°. This behavior is very difficult to explain in terms of the model of a single star with a shell containing spherical particles alone. If, alternatively, there are nonspherical grains in the shell, then variations in the degree and direction of grain alignment may result in observable variations of the polarization angle.

The first attempt to take into account the effect of the shape of interstellar grains on their temperature was made by Greenberg and Shah (1971). These authors considered metallic and dielectric Rayleigh spheroids and infinite ice cylinders of 0.1-μm radius. They concluded that nonspherical particles were approximately 10% colder than spheres, a result that entered the books on interstellar dust (Whittet 1992).

Recently, Fogel and Leung (1998) have computed the infrared radiation of fractal dust grains produced by two processes of stochastic growth and composed of amorphous carbon and silicate. They concluded that the temperature of nonspherical particles was typically 10–20% lower than that of spherical ones, which results in a longward shift of the maximum of the object's radiation. Fogel and Leung (1998) proposed to consider the fractal particle size as a parameter of the grain shape, but they ignored the effects of alignment.

Here, we study in detail the dependence of the temperature of spheroidal circumstellar dust grains on their shape and alignment. We consider prolate and oblate particles of various sizes, which are composed of a variety of absorbing and dielectric materials and which lie at various distances from stars with various temper-

---

[1] To the memory of Gennadii Borisovich Sholomitskiĭ, an enthusiast for research in the field of infrared and submillimeter astronomy.

* E-mail address for contacts: nvv@dust.astro.spbu.ru

atures. The nonsphericity effect of interstellar dust grains on their temperature was discussed by Voshchinnikov *et al.* (1999).

2. THE MODEL

2.1. The Radiation Field

Dust particles are present in the envelopes of late-type stars (red giants and supergiants) and hotter stars, such as Herbig Ae/Be stars. Dust grains are heated mainly by the absorption of stellar radiation. As was pointed out by Lamy and Perrin (1997), in some cases, it is important to take into account the star's true spectral energy distribution as well. In addition, in the outer regions of optically thick dust shells, the maximum in the energy distribution is redshifted (see, e.g., Bagnulo *et al.* 1995). For simplicity, however, we assume the energy distribution to be a blackbody one with an effective temperature $T_\star$. Since we are going to compare the temperatures of particles under the same conditions, this assumption is of no fundamental importance.

In most cases, we take the stellar temperature to be $T_\star = 2500$ K, typical of late-type giants and supergiants (Pégourie 1987; Lorenz-Martins and Léfevre 1994). The effects of variations in $T_\star$ are discussed in subsection 4.5.

2.2. Dust Particles

Chemical composition. Particles of amorphous carbon and amorphous silicates are most commonly considered as the major sources of the infrared radiation observed from carbon and oxygen stars, respectively. Evidence in support of these materials follows both from theoretical models of dust formation (Gail and Sedlmayr 1984) and from laboratory experiments (Jäger *et al.* 1994).

The specific type of silicate or carbon material in the circumstellar medium is very difficult to determine. In addition, there is most likely a mixture of various dust components in the shells simultaneously. For example, bands of silicon carbide, sulfide silicates, and even amorphous silicates were detected in the spectra of some carbon stars (Baron *et al.* 1987; Goebel and Moseley; Little-Marenin 1986). Several emission bands found in the spectra of carbon stars were identified with crystalline silicates (Waters *et al.* 1999). Finally, iron and oxide particles can apparently condense in circumstellar envelopes irrespective of the C/O ratio.

In our modeling, we used the six materials that were previously chosen by Il'in and Voshchinnikov (1998) when considering the effect of radiation pressure on dust grains in the envelopes of late-type stars: amorphous carbon, iron, and magnetite (Fe_3O_4) as examples of strongly absorbing materials, as well as astronomical silicate (astrosil), transparent glassy pyroxene, and artificial dirty silicate (Ossenkopf *et al.* 1992; OHM silicate) as silicates of various types. References to the papers from which we took the optical constants of these materials can be found in Il'in and Voshchinnikov (1998).[2] This set of materials was extended to include carbon material (cellulose), which was produced by pyrolysis at a temperature of 1000°C (cel1000; Jäger *et al.* 1998), and dirty ice, which was used in the classical study by Greenberg and Shah (1971). In the latter case, the imaginary part of the refractive index was chosen to be $k = 0.02$ in the wavelength range 0.17–1.2 μm, as was done by Greenberg (1970, 1971).

Shape. The formation of only spherical particles in the envelopes of late-type stars has been considered thus far (see, e.g., Draine 1981; Gail and Sedlmayr 1985; Fadeyev 1987; Fleischer *et al.* 1992; Cadwell *et al.* 1994). The theory of nucleation and growth of nonspherical particles is still at the initial stage of its development.

We assume the circumstellar dust grains to be prolate and oblate homogeneous spheroids with aspect ratios a/b (a and b are the spheroid semimajor and semiminor axes, respectively). By varying a/b, we can model the particle shape over a wide range: from spheres to needles and disks.

Size. Dust grains form and grow in the envelopes of late-type stars. They range in size from tiny particles to particles with radii up to 1 μm or more [see Lafon and Berruyer (1991) for a discussion]. The upper limit of the grain size distribution is uncertain and is the subject of debate. However, it follows from model calculations that, in general, the particle size in oxygen stars is larger than that in carbon ones (Jura 1994, 1996; Bagnulo *et al.* 1995).

In order to compare the optical properties of particles of the same volume but different shape, it is convenient to characterize the particle size by the radius r_V of a sphere equal in volume to a spheroid. The spheroid semimajor axis is related to r_V by

$$a = r_V \left(\frac{a}{b}\right)^{2/3} \tag{1}$$

for prolate spheroids and by

$$a = r_V \left(\frac{a}{b}\right)^{1/3} \tag{2}$$

for oblate spheroids. In our calculations, we considered particles with $r_V = 0.005$–0.5 μm.

Structure. The dust grains growing in circumstellar shells can be fluffy or porous. To model the effect of porosity, we used Bruggeman's rule (Bohren and Huffman 1986) and obtained the mean effective dielectric

---

[2] Data on the refractive indices can also be extracted from an electronic database of optical constants (Henning *et al.* 1999) via Internet at http://www.astro.spbu.ru/JPDOC/entry.html.

function $\varepsilon_{\mathrm{eff}}$ of an aggregate composed of n materials with dielectric functions ε_i,

$$\sum_{i=1}^{n} f_i \frac{\varepsilon_i - \varepsilon_{\mathrm{eff}}}{\varepsilon_i + 2\varepsilon_{\mathrm{eff}}} = 0, \tag{3}$$

where f_i is the fraction of the volume occupied by the material of type i. The temperature is calculated for compact particles with $\varepsilon_{\mathrm{eff}}$. We considered spheroids composed of vacuum ($\varepsilon = 1$) and cellulose with vacuum fractions from 0 to 0.9.

Orientation. Collisions of dust grains with atoms and molecules cause rapid grain rotation with angular velocities $>10^5$ s^{-1}. Interstellar particles are believed to rotate around the direction of maximum moment of inertia, and, in general, the angular momentum is parallel to the magnetic field (Spitzer 1981). Circumstellar particles can be aligned by anisotropic radiation or gas fluxes (Dolginov *et al.* 1979). Radial grain motion in the shells must apparently cause particle rotation in the planes containing the radius vector. However, nonradical gas flows or the helical circumstellar magnetic fields produced by stellar rotation (see, e.g., Woitke *et al.* 1993) can also result in a different grain alignment.

In our modeling, we considered two types of grain orientation: particles randomly oriented in space (3D orientation) and in a plane (2D orientation or complete rotational orientation). In the latter case, the major axis of a rotating spheroid always lies in the same plane. The angle Ω between the particle angular velocity and the wave vector of the incident radiation is a model parameter ($0° \le \Omega \le 90°$).

3. BASIC EQUATIONS

Let us consider a dust grain at distance R from a star of radius $R_\star$ and temperature $T_\star$. The stellar radiation is assumed to be unpolarized. The equilibrium grain temperature T_{d} can be determined from Kirchoff's law by solving the energy balance equation for the absorbed and emitted energy (erg s^{-1})

$$W\int_0^{\infty} \overline{C}_{\mathrm{abs}}(\lambda)\pi B_\lambda(T_\star)d\lambda = \int_0^{\infty} \overline{C}_{\mathrm{em}}(\lambda)\pi B_\lambda(T_{\mathrm{d}})d\lambda, \tag{4}$$

where $\overline{C}_{\mathrm{abs}}(\lambda)$ and $\overline{C}_{\mathrm{em}}(\lambda)$ are the orientation-averaged absorption and emission cross sections, $\pi B_\lambda(T)$ is the blackbody flux with temperature T (erg cm^{-2} s^{-1} μm^{-1}), and $W = R_\star^2/R^2$ is the radiation dilution factor.

For particles randomly oriented in space, the absorption cross sections must be averaged over all orientations:

$$\overline{C}_{\mathrm{abs}}^{\mathrm{3D}} = \int_0^{\pi/2} \frac{1}{2}[Q_{\mathrm{abs}}^{\mathrm{TM}}(m_\lambda, r_V, \lambda, a/b, \alpha)$$
$$+ Q_{\mathrm{abs}}^{\mathrm{TE}}(m_\lambda, r_V, \lambda, a/b, \alpha)]G(\alpha)\sin\alpha d\alpha. \tag{5}$$

Here, m_λ is the refractive index of the grain material ($m_\lambda = \varepsilon_\lambda^{1/2}$), α is the angle between the spheroid rotation axis and the wave vector ($0° \le \alpha \le 90°$), and G is the geometric cross section of the spheroid (the area of the particle shadow):

$$G(\alpha) = \pi r_V^2 \left(\frac{a}{b}\right)^{-2/3} \left[\left(\frac{a}{b}\right)^2 \sin^2\alpha + \cos^2\alpha\right]^{1/2} \tag{6}$$

for prolate spheroids and

$$G(\alpha) = \pi r_V^2 \left(\frac{a}{b}\right)^{2/3} \left[\left(\frac{a}{b}\right)^{-2} \sin^2\alpha + \cos^2\alpha\right]^{1/2} \tag{7}$$

for oblate spheroids.

In the case of complete rotational orientation, the absorption cross sections are averaged over all rotation angles ϕ. For prolate spheroids, this yields

$$\overline{C}_{\mathrm{abs}}^{\mathrm{2D}}(\Omega) = \frac{2}{\pi}\int_0^{\pi/2} \frac{1}{2}[Q_{\mathrm{abs}}^{\mathrm{TM}}(m_\lambda, r_V, \lambda, a/b, \alpha)$$
$$+ Q_{\mathrm{abs}}^{\mathrm{TE}}(m_\lambda, r_V, \lambda, a/b, \alpha)]G(\alpha)d\phi, \tag{8}$$

where the angle α is related to Ω and ϕ ($\cos\alpha = \sin\Omega\cos\phi$). For oblate spheroids arbitrarily oriented in a plane, we have $\Omega = \alpha$ and

$$\overline{C}_{\mathrm{abs}}^{\mathrm{2D}}(\Omega) = \frac{1}{2}[Q_{\mathrm{abs}}^{\mathrm{TM}}(m_\lambda, r_V, \lambda, a/b, \Omega)$$
$$+ Q_{\mathrm{abs}}^{\mathrm{TE}}(m_\lambda, r_V, \lambda, a/b, \Omega)]G(\Omega). \tag{9}$$

The energy emitted by a particle is proportional to its surface area. The emission cross section can then be calculated as follows:

$$\overline{C}_{\mathrm{em}} = S\int_0^{\pi/2} \frac{1}{2}[Q_{\mathrm{abs}}^{\mathrm{TM}}(m_\lambda, r_V, \lambda, a/b, \alpha)$$
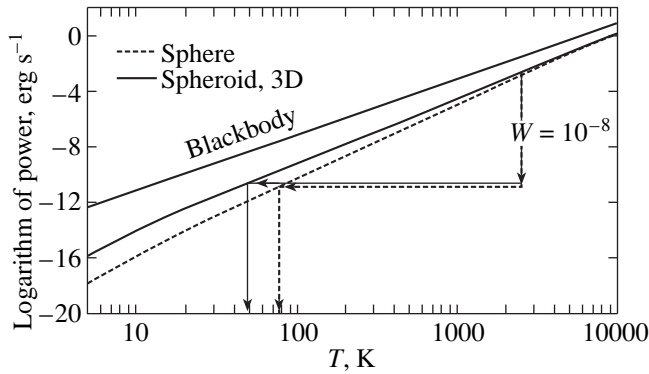$$+ Q_{\mathrm{abs}}^{\mathrm{TE}}(m_\lambda, r_V, \lambda, a/b, \alpha)]\sin\alpha d\alpha, \tag{10}$$

where

$$S = 2\pi r_V^2\left[\left(\frac{a}{b}\right)^{-2/3} + \left(\frac{a}{b}\right)^{1/3}\frac{\arcsin(e)}{e}\right] \tag{11}$$

for prolate spheroids and

$$S = 2\pi r_V^2\left[\left(\frac{a}{b}\right)^{2/3} + \left(\frac{a}{b}\right)^{-4/3}\frac{\ln[(1+e)/(1-e)]}{2e}\right] \tag{12}$$

for oblate spheroids, $e = \sqrt{1 - (a/b)^{-2}}$.

Fig. 1. The power absorbed (emitted) by dust particles with $r_V = 0.01$ μm in an isotropic radiation field. The straight line corresponds to a blackbody. The curves refer to spherical and prolate spheroidal ($a/b = 10$, 3D orientation) cellulose (cel1000) particles. A graphical method of determining the grain temperature is shown for $T_\star = 2500$ K and $W = 10^{-8}$. In this case, the temperatures of spherical and spheroidal particles and a blackbody are respectively, $T_d(\text{sphere}) = 76.8$ K, $T_d^{3D} = 48.7$ K, and $T_d^{BB} = 2500(10^{-8})^{1/4} = 25$ K.

In Eqs. (5), (8), (9), and (10), the superscripts TM and TE refer to two polarizations of the incident radiation (TM and TE modes). The efficiency factors $Q_{abs}^{TM, TE}$ can be calculated using an exact solution to the problem of diffraction of a plane electromagnetic wave by a homogeneous spheroid by separation of variables [see Voshchinnikov and Farafonov (1993) for more detail]. We used the benchmark results of calculations of the efficiency factors from Voshchinnikov *et al.* (2000) to thoroughly test the computational program.

4. RESULTS AND DISCUSSION

In this section, we discuss the dependence of the spheroidal-grain temperature on model parameters: the particle chemical composition, size, shape, and orientation, as well as the stellar temperature and distance to the star. We also consider the effects of porosity and partial polarization of the incident radiation on the particle temperature. Since the main goal of our study is to analyze the effects of change in the particle shape, we compare the temperature ratio of spheroidal and spherical particles of the same volume.

4.1. A Graphical Method of Temperature Determination and a Blackbody Model

This method, proposed by Greenberg (1970, 1971), allows the causes of temperature differences between dust grains with different characteristics to be clearly established if the particles are assumed to be in an iso-

tropic radiation field. Their temperature can then be determined by solving the following equation of thermal balance:

$$
\begin{aligned}
W &\int_0^\infty \overline{C}_{abs}(\lambda) 4\pi B_\lambda(T_\star) d\lambda \\
&= \int_0^\infty \overline{C}_{em}(\lambda) \pi B_\lambda(T_d) d\lambda.
\end{aligned}
\tag{13}
$$

If the spheroidal particles are randomly oriented in space (3D orientation), then numerical estimates show that

$$
\overline{C}_{abs}^{3D} \approx \frac{\overline{C}_{em}}{4}.
\tag{14}
$$

The integrals on the left- and right-hand sides of Eq. (13) then depend on the temperature T alone (for given particle chemical composition, size, and shape).

Figure 1 shows the power for the absorbed (emitted) radiation (in erg s^{-1}) for spheres and spheroids of the same volume ($r_V = 0.01$ μm) composed of cellulose (cel1000). The method of temperature determination is indicated by arrows: from the point on the curve corresponding to the stellar temperature ($T_\star = 2500$ K), we drop a perpendicular whose length is determined by the radiation dilution factor and then find the point of intersection of the horizontal segment with the same curve for the power. This point gives the dust grain temperature T_d determined from the equation of thermal balance (13).

It follows from Fig. 1 that the different temperatures of spheres and spheroids result from different particle emissivities at low T. The differences are most noticeable for cellulose. For other materials, the pattern of dependence is preserved: the emissivity of spheroidal particles at low temperatures is larger than that for spheres and closer to the blackbody one (see Fig. 2). Only iron particles constitute an exception: spheres composed of them at $T \lesssim 30$ K emit more energy than spheroids with $a/b \simeq 2$–6 but less energy than spheroids with $a/b \gtrsim 8$ (Fig. 3).

The straight lines in the upper parts of Figs. 2 and 3 refer to a blackbody, for which the emissivity is proportional to T^4, and the absorption efficiency factors are equal to unity,
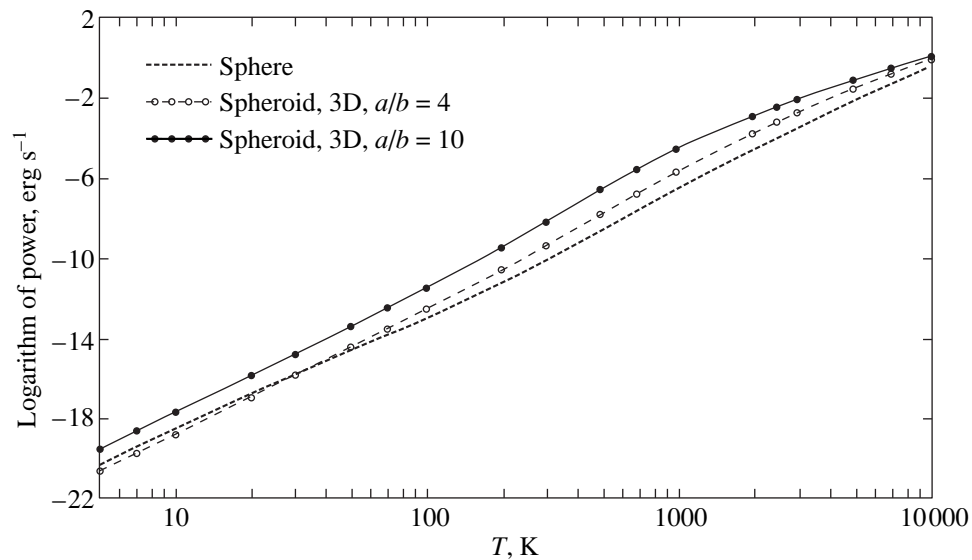
$$
Q_{abs}^{TM} = Q_{abs}^{TE} = 1.
\tag{15}
$$

Using Eq. (15) and Stefan–Boltzmann's law, instead of (13) we obtain for the 3D orientation

$$
4W\overline{G}^{3D}\sigma T_\star^4 = S\sigma T_d^4.
\tag{16}
$$
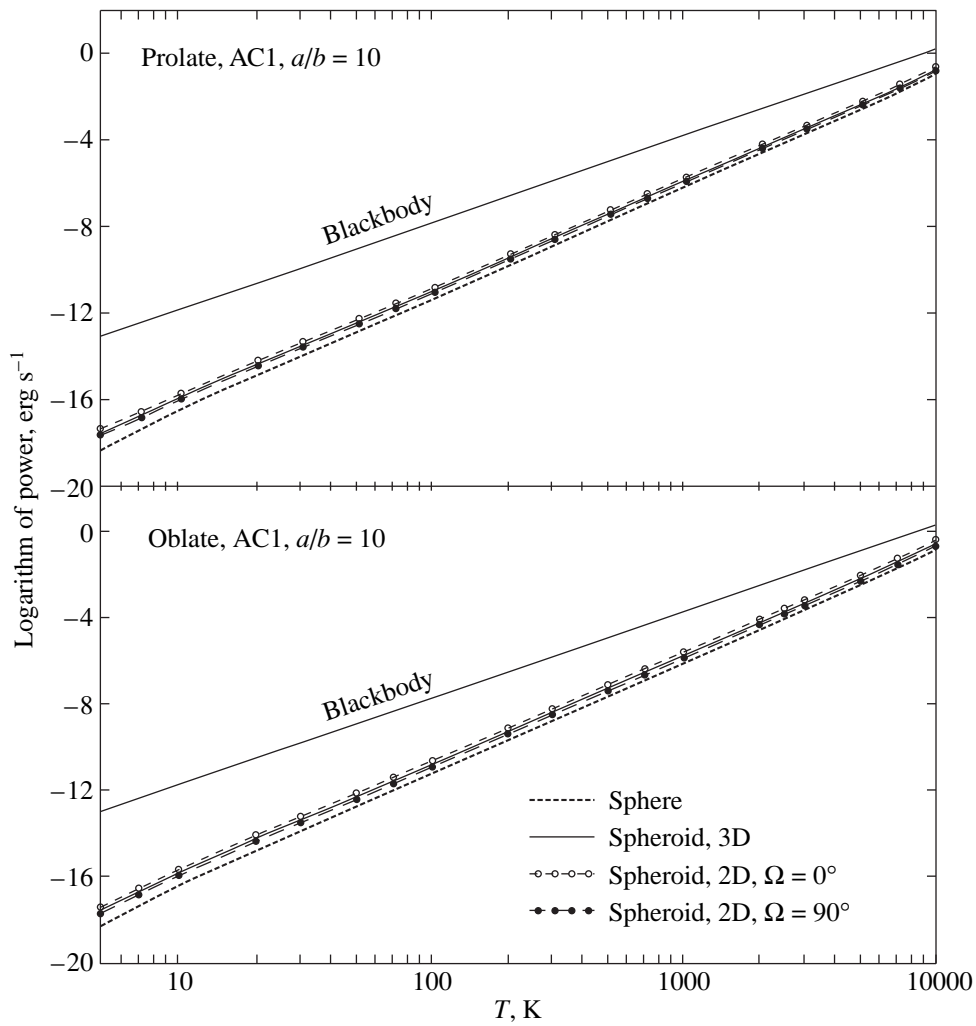
Fig. 2. The power absorbed by dust particles with $r_V = 0.01$ μm in an anisotropic radiation field. The curves refer to spherical, prolate, and oblate spheroidal amorphous carbon (AC1) particles with $a/b = 10$. The straight line corresponds to a blackbody.

Fig. 3. The power absorbed by iron dust particles with $r_V = 0.01$ μm in an anisotropic radiation field.
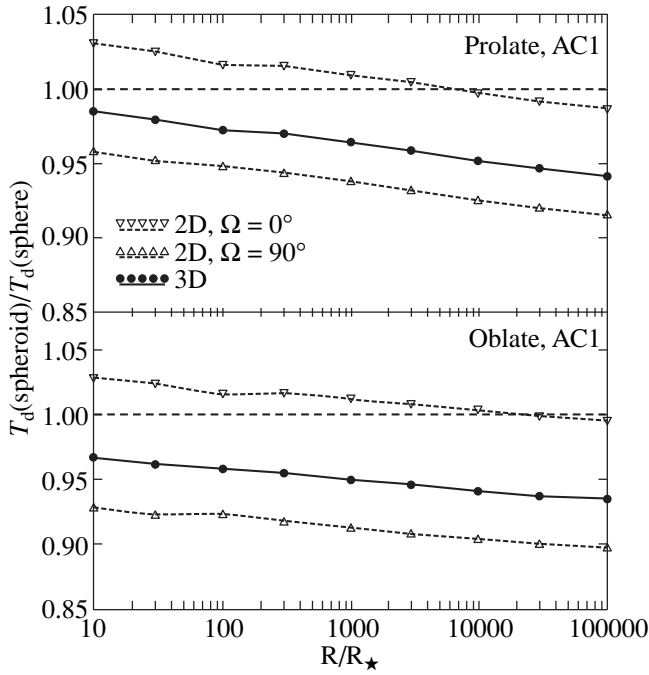
Fig. 4. The temperature ratio of prolate and oblate spheroidal ($a/b = 4$) and spherical amorphous carbon (AC1) grains with $r_V = 0.01$ μm at various distances from a star with $T_\star = 2500$ K. The sphere temperature is T_d(sphere) = 780.6, 318.0, 130.8, 52.3, and 20.8 K for $R = 10$, 10^2, 10^3, 10^4, and 10^5 $R_\star$, respectively.

Given that the mean projection area of any convex figure is a quarter of its surface area (see, e.g., Hildebrand 1983),[3]

$$\overline{G}^{3D} = \frac{S}{4}, \qquad (17)$$

we have for spheres and spheroids randomly oriented in space

$$T_d^{BB} = T_\star W^{1/4}. \qquad (18)$$

For the 2D orientation, the blackbody temperature is

$$T_d^{BB} = T_\star \left(\frac{4W\overline{G}^{2D}(\Omega)}{S} \right)^{1/4}. \qquad (19)$$

Expressions for the mean cross sections in the case of complete rotational orientation were derived by Il'in and Voshchinnikov (1998):

$$\overline{G}^{2D}(\Omega) = \pi r_V^2 \frac{2}{\pi} E\left(\left[1 - \left(\frac{a}{b} \right)^{-2} \right] \sin^2\Omega \right) \left(\frac{a}{b} \right)^{1/3} \qquad (20)$$

for prolate spheroids and

$$\overline{G}^{2D}(\Omega) = G(\Omega) \qquad (21)$$

---

[3] Relation (17) for prolate and oblate spheroids can be proved by directly integrating Eqs. (6) and (7).

for oblate spheroids. In relation (20), the complete elliptic integral of the second kind is denoted by $E(m)$.

Based on (20) and (21), we can easily determine the blackbody-temperature ratios for the two extreme cases of 2D orientation ($\Omega = 0°$ and $90°$):

$$\frac{T_d^{BB}(\Omega = 0°)}{T_d^{BB}(\Omega = 90°)} = \left(\frac{\overline{G}^{2D}(\Omega = 0°)}{\overline{G}^{2D}(\Omega = 90°)} \right)^{1/4}$$

$$= \left(\frac{\pi}{2E\left(1 - \left(\frac{a}{b}\right)^{-2}\right)} \right)^{1/4} \qquad (22)$$

for prolate spheroids and

$$\frac{T_d^{BB}(\Omega = 0°)}{T_d^{BB}(\Omega = 90°)} = \left(\frac{a}{b} \right)^{1/4} \qquad (23)$$

for oblate spheroids. We can also calculate the temperature ratio of a spheroid for the 2D orientation and a sphere (or a spheroid for the 3D orientation):

$$\frac{T_d^{BB}(\Omega)}{T_d^{BB}(\text{sphere, 3D})} = \left(\frac{4\overline{G}^{2D}(\Omega)}{S} \right)^{1/4}. \qquad (24)$$

Note that relations (22)–(24) allow the geometric effects on the temperature of nonspherical dust grains to be estimated. For example, $T_d^{BB}(\Omega = 0°)/T_d^{BB}(\text{sphere}) = 1.06$ (1.18) for $a/b = 10$ and $T_d^{BB}(\Omega = 90°)/T_d^{BB}(\text{sphere}) = 0.95$ (0.66) for prolate (oblate) spheroids.

4.2. Dependence on the Distance from the Star

The temperature of particles of any shape decreases with distance from the heating source (star). However, the temperature ratio of nonspherical and spherical particles varies over a narrow range. As follows from Fig. 4, which shows the results of our calculations for amorphous carbon particles, this ratio decreases approximately by 5% as the distance to the star increases from 10 to 10^5 $R_\star$. In this case, the sphere temperature decreases from 780.6 to 20.8 K. Given the insignificant variation of T_d(spheroid)/T_d(sphere) with R, below we consider the results only for $R = 10^4 R_\star$ ($W = 10^{-8}$).

4.3. Dependence on the Grain Size

The temperature variations of carbon and silicate dust grains with particle radius are given in Tables 1 and 2. As r_V increases, the particle temperature slightly rises and then begins to fall, as was also noted previously (Greenberg 1970). The temperature of spheroidal particles is always slightly lower than that of spherical ones; the difference can reach 10% at $a/b = 4$. The tem-

Table 1. The temperatures (in K) of spherical and spheroidal ($a/b = 4$) amorphous carbon grains; $T_\star = 2500$ K and $R = 10000 R_\star$

r_V, μm	Sphere	Prolate spheroid			Oblate spheroid		
		2D, $\Omega = 0°$	2D, $\Omega = 90°$	3D	2D, $\Omega = 0°$	2D, $\Omega = 90°$	3D
0.005	52.3	52.1	48.4	49.7	52.4	47.2	49.2
0.010	52.3	52.2	48.4	49.8	52.4	47.3	49.2
0.020	52.4	52.3	48.5	49.9	52.6	47.4	49.3
0.030	52.6	52.5	48.7	50.1	52.8	47.6	49.5
0.050	53.3	53.2	49.2	50.6	53.3	48.2	50.1
0.100	56.0	54.9	51.0	52.4	54.8	50.4	52.0
0.200	61.1	55.5	54.4	54.7	54.6	54.3	54.3
0.300	62.3	55.0	55.7	55.4	53.6	55.4	54.6
0.500	60.2	53.5	54.3	54.0	51.8	53.6	52.9

Table 2. The temperatures (in K) of spherical and spheroidal ($a/b = 4$) astronomical silicate grains; $T_\star = 2500$ K and $R = 10000 R_\star$

r_V, μm	Sphere	Prolate spheroid			Oblate spheroid		
		2D, $\Omega = 0°$	2D, $\Omega = 90°$	3D	2D, $\Omega = 0°$	2D, $\Omega = 90°$	3D
0.005	34.9	31.9	30.6	31.2	32.6	30.5	31.3
0.010	34.9	31.9	30.6	31.1	32.7	30.5	31.3
0.020	34.9	31.9	30.7	31.1	32.7	30.6	31.4
0.030	35.0	32.0	30.7	31.2	32.8	30.6	31.4
0.050	35.2	32.2	30.9	31.4	32.9	30.8	31.6
0.100	36.0	32.8	31.5	32.0	33.5	31.5	32.2
0.200	38.2	33.5	33.0	33.1	33.8	33.3	33.4
0.300	39.6	33.7	34.4	34.0	33.6	34.7	34.2
0.500	40.5	34.1	35.4	34.9	33.4	35.9	34.8

perature difference between spheres and spheroids is largest for the 2D orientation and $\Omega = 90°$. Note also that, since T_d for spheres and spheroids vary with r_V similarly, the temperature ratio is almost independent of r_V.

4.4. Dependence on the Grain Shape and Chemical Composition

The effects of the chemical composition and shape of dust grains on their temperature are most significant compared to the variations of other model parameters. These effects are illustrated in Figs. 5 and 6, which show the temperature ratios of spheroids and spheres for particles with metallic and dielectric properties, respectively. The variations of $T_d(\text{spheroid})/T_d(\text{sphere})$ have the following general tendency: this ratio decreases with increasing a/b and absorptive material properties, with the effect increasing. Besides, the following inequality holds for particles of the same volume:

$$T_d(\text{sphere}) > T_d^{2D}(\Omega = 0°) > T_d^{3D} > T_d^{2D}(\Omega = 90°).$$
(25)

The difference between prolate and oblate particles, which is noticeable in Figs. 5 and 6, is determined by different optical properties of the particles [see Voshchinnikov and Farafonov (1993) for more detail]. If we restrict ourselves to $a/b \lesssim 4$, then it is easy to see that the dielectric and metallic spheroids are, respectively, 10% and 20% colder than the corresponding spheres. The temperatures of prolate and oblate particles can differ by 30–40% from the temperature of spheres (Fig. 5). If we further increase the aspect ratio a/b, then the temperature gradually ceases to drop. For example, for prolate cel1000 particles, $T_d^{3D}/T_d(\text{sphere}) = 0.61, 0.53, 0.50,$ and 0.50 for $a/b = 10, 20, 50,$ and 100, respectively.

The temperature behavior for iron particles is peculiar: for $a/b \lesssim 8$, the spheroids are 10–20% hotter than the spheres. The reason for this is seen from the behavior of the particle emissivity shown in Fig. 3.

4.5. Dependence of the Stellar Temperature

Nonspherical particles may be present in the shells of stars of various spectral types and in the interplanetary medium. The effects of variations in the stellar temperature are shown in Fig. 7 for amorphous carbon particles with $r_V = 0.01$ μm. Low effective temperatures (up to 500 K) correspond to possible conditions in the outer parts of optically thick circumstellar shells. It fol-
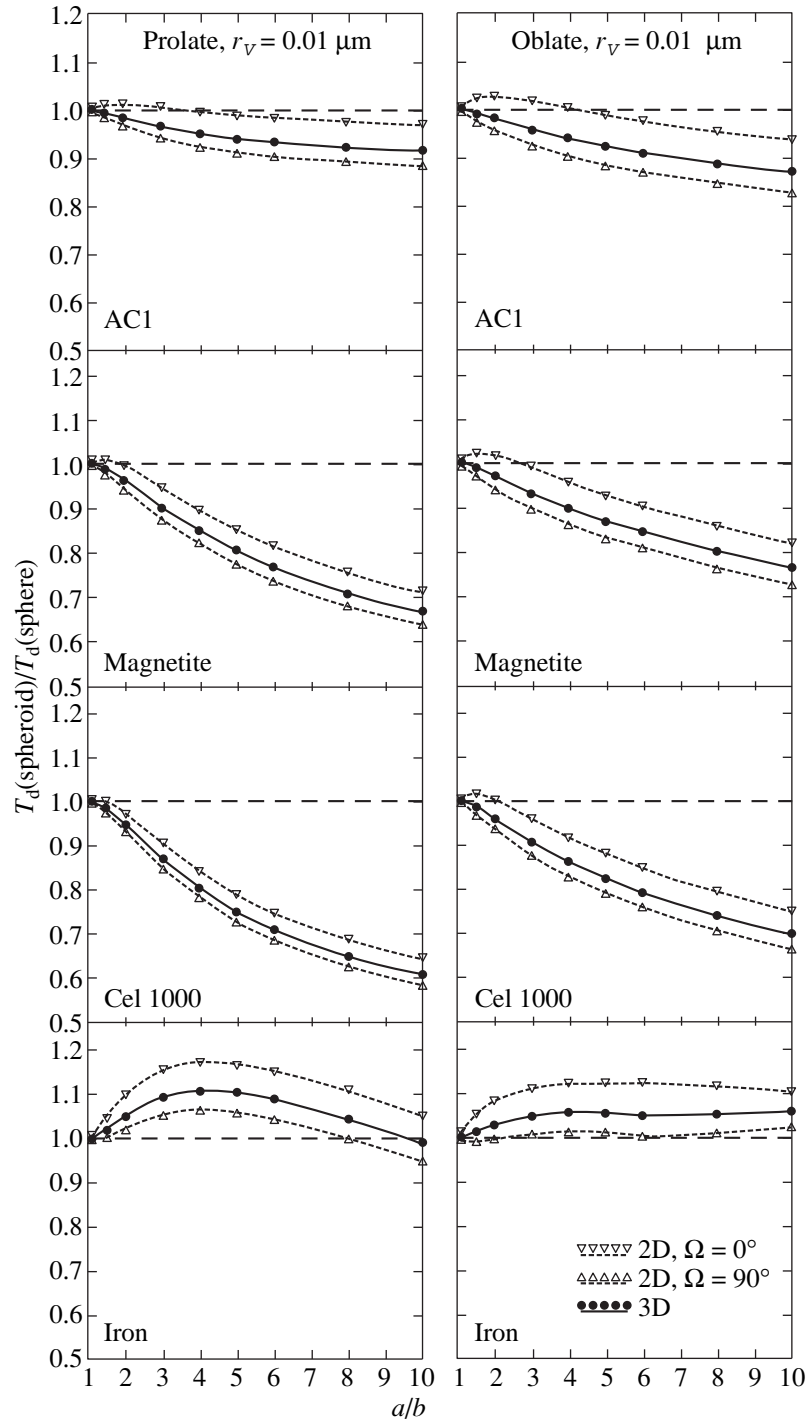
Fig. 5. The temperature ratio of prolate and oblate spheroidal and spherical grains composed of various materials with metallic properties; $T_\star = 2500$ K, $r_V = 0.01$ μm, and $R = 10^4 R_\star$. The sphere temperature is $T_d(\text{sphere}) = 52.3$, 63.0, 59.2, and 120.0 K for particles of amorphous carbon, magnetite, cellulose, and iron, respectively.

lows from Fig. 7 that there is no effect for $T_d(\text{spheroid})/T_d(\text{sphere})$, although the absolute temperature varies over a fairly wide range: from $T_d(\text{sphere}) = 10.6$ K at $T_\star = 500$ K to $T_d(\text{sphere}) = 226.4$ K at $T_\star = 10\,000$ K.

4.6. Porous Dust Grains and Polarized Incident Radiation

An increase in the fraction f of vacuum in porous particles causes a decrease in the effective refractive index, i.e., a reduction in particle absorptivity. In this
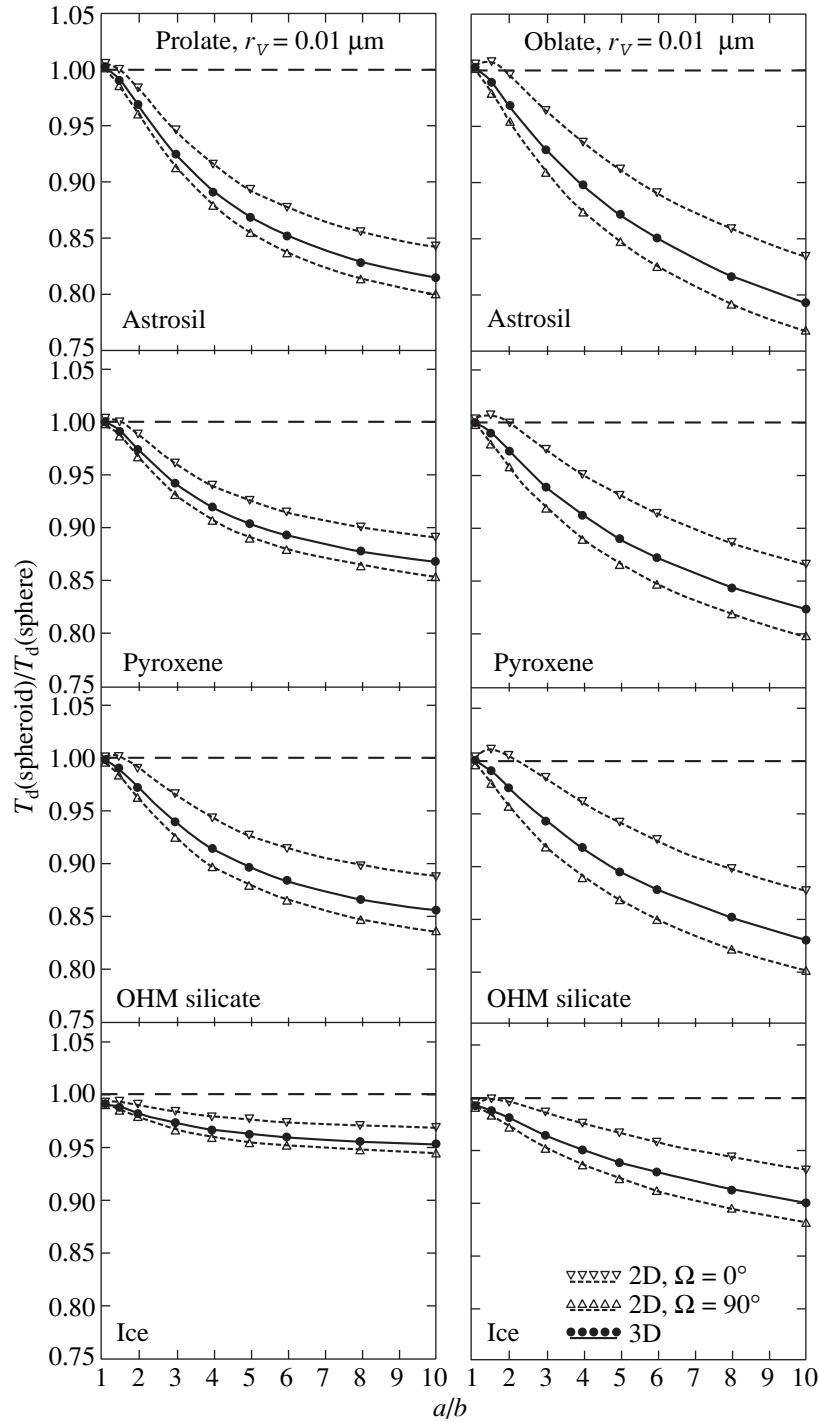
Fig. 6. The same as Fig. 5 for particles with dielectric properties. The sphere temperature is $T_d(\text{sphere}) = 34.9, 24.0, 42.4,$ and 33.7 K for particles of astrosil, pyroxene, OHM silicate, and dirty ice, respectively.

case, the shape effects gradually disappear, and the temperature of spheroidal particles approaches the temperature of spheres. This effect is illustrated in Table 3, which shows that $T_d(\text{spheroid})/T_d(\text{sphere})$ increases considerably for cellulose particles at $f \gtrsim 0.5$.

The aligned nonspherical particles in the inner parts of circumstellar dust shells can polarize the stellar radi-

ation. In principle, the local linear polarization of scattered radiation can be significant. The absorption efficiency factors for the TM and TE modes must then enter into the absorption cross sections [relations (5), (8), and (9)] with different weights, depending on the polarization P of the incident radiation. This causes an increase in the temperature of prolate spheroids if the
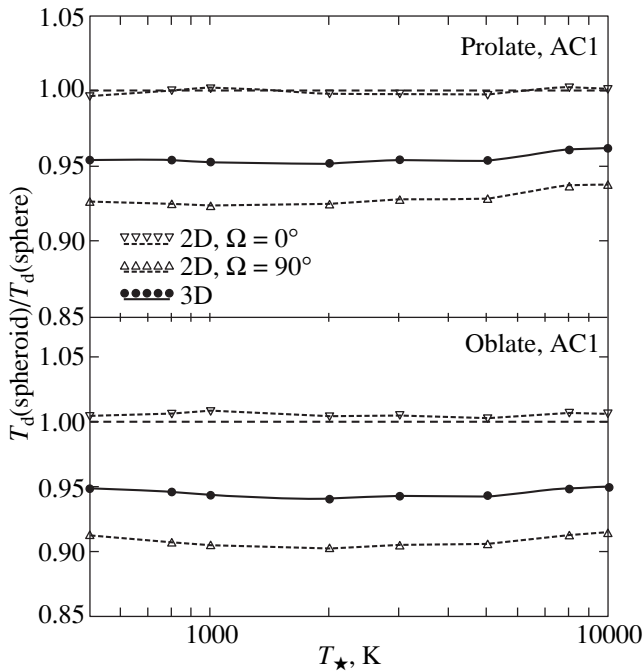
Fig. 7. The temperature ratio of prolate and oblate spheroidal ($a/b = 4$) and spherical amorphous carbon (AC1) grains with $r_V = 0.01$ μm at $R = 10^4 R_\star$ from the star. The sphere temperature is $T_d(\text{sphere}) = 10.5, 20.4, 63.1, 106.4,$ and 226.4 K for $T_\star = 500, 1000, 3000, 5000,$ and $10\,000$ K, respectively.

electric vector of the incident radiation is parallel to the particle major axis (in this case, $Q_{\text{abs}}^{\text{TM}} > Q_{\text{abs}}^{\text{TE}}$) and a decrease in their temperature otherwise ($Q_{\text{abs}}^{\text{TM}} < Q_{\text{abs}}^{\text{TE}}$). The reverse is true for oblate spheroids. However, the effect is not too large: even at $P = 50\%$, the temperature of prolate spheroidal ($a/b = 10$) cellulose particles varies between 33.2 and 38.3 K ($T_d^{3D} = 36.0$ K at $P = 0\%$).

The following fairly general conclusion can be drawn from what was considered above: the temperatures of spherical and nonspherical dust grains are pro-

Table 3. The temperatures (in K) of porous spherical and prolate spheroidal ($a/b = 10$) cellulose (cel1000) grains; $r_V = 0.01$ μm, $T_\star = 2500$ K, and $R = 10000 R_\star$

$1-f$	$T_d(\text{spheroid})/T_d(\text{sphere})$			$T_d(\text{sphere})$
	2D, $\Omega = 0°$	2D, $\Omega = 90°$	3D	
1.0	0.65	0.59	0.61	59.2
0.9	0.65	0.59	0.61	57.7
0.7	0.68	0.63	0.65	53.5
0.5	0.77	0.73	0.74	47.3
0.3	0.94	0.91	0.92	45.0
0.2	0.98	0.96	0.96	49.4
0.1	0.98	0.97	0.97	54.8

portional, with the proportionality coefficient being approximately the same for particles of different sizes at different distances in the envelopes of stars of different spectral types. This coefficient is determined only by the particle shape and by absorptive properties of the material of which they are composed.

5. ASTROPHYSICAL IMPLICATIONS

The dust temperature is an important parameter that determines the infrared spectra of various objects. The efficiency of grain growth and destruction, formation of molecules on the grain surfaces, and the alignment of nonspherical particles depend on T_d (Voshchinnikov 1986). Besides, T_d determines the polarized submillimeter emission of nonspherical particles (Onaka 2000) and the gas cooling rate in very dense interstellar clouds (Whitworth *et al.* 1998).

The infrared flux at wavelength λ emerging from an optically thin medium is proportional to the total number N of dust grains in the medium, the Planck function, which depends on the particle temperature T_d, and the emission cross section $\overline{C}_{\text{em}}(\lambda)$:

$$F_{\text{IR}}(\lambda) = N \frac{\overline{C}_{\text{em}}(\lambda)}{D^2} B_\lambda(T_d), \qquad (26)$$

where D is the distance to the object. The quantities T_d and $\overline{C}_{\text{em}}(\lambda)$ in Eq. (26) depend on the particle shape.

If we assume the chemical composition and sizes of all particles in the medium to be the same and if we change only the grain shape, then, when spheres are replaced by nonspherical particles, the position of the maximum in the spectrum of thermal radiation is shifted longward, because the temperature of the latter is higher (Fig. 8).

The flux ratio is specified as follows:

$$\frac{F_{\text{IR}}^{\text{spheroid}}(\lambda)}{F_{\text{IR}}^{\text{sphere}}(\lambda)} = \frac{\overline{C}_{\text{em}}^{\text{spheroid}}(\lambda)}{C_{\text{em}}^{\text{sphere}}(\lambda)} \frac{B_\lambda[T_d(\text{spheroid})]}{B_\lambda[T_d(\text{sphere})]}. \qquad (27)$$

It is shown in Fig. 9, where the ratios of the cross sections and the Planck functions in relation (27) are also displayed. Despite the different particle temperatures, the Planck functions differ insignificantly. The main differences in the fluxes result from different emission cross sections $\overline{C}_{\text{em}}(\lambda)$: they are considerably larger for nonspherical particles at $\lambda > \lambda_{\text{max}}$ (Fig. 9). This effect was previously noted by Ossenkopf and Henning (1994).

If the dust mass in an object is determined from the observed millimeter flux, then the Rayleigh–Jeans approximation can be used for the Planck function. For the same flux $F_{\text{IR}}(\lambda)$, the dust mass depends on the par-
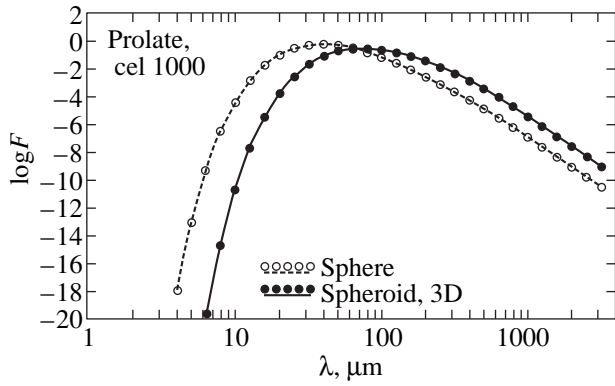
Fig. 8. The normalized fluxes emerging from a medium containing the same (by mass) amount of spherical and prolate spheroidal ($a/b = 10$, 3D orientation) cellulose (cel1000) particles; $r_V = 0.01\ \mu m$, $T_\star = 2500$ K, and $R = 10^4\ R_\star$. The particle temperatures are $T_d(\text{sphere}) = 59.2$ and $T_d^{3D} = 36.0$ K.
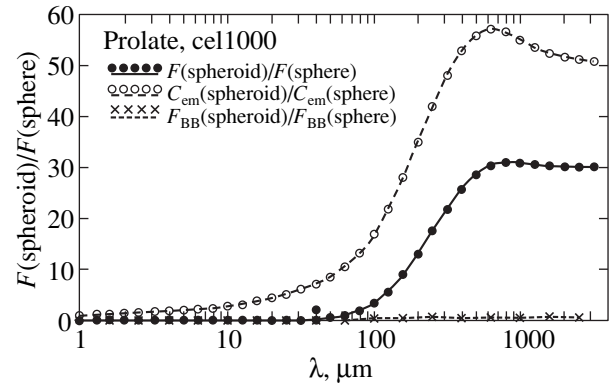
Fig. 9. The same as Fig. 8 for the flux ratio. The ratios of the emission cross sections and fluxes for a blackbody are also shown. The latter are determined by the particle temperature alone.

ticle emission cross sections and temperatures, while the ratio

$$\frac{M_d^{\text{sphere}}}{M_d^{\text{spheroid}}} = \frac{\overline{C}_{\text{em}}^{\text{spheroid}}(\lambda)}{C_{\text{em}}^{\text{sphere}}(\lambda)} \frac{T_d(\text{spheroid})}{T_d(\text{sphere})} \qquad (28)$$

shows the extent to which the values of M_d differ when changing the grain shape.

The dust mass in galaxies and molecular clouds is commonly estimated from 1.3-mm observations (Siebenmorgen *et al.* 1999). At this wavelength, the ratio of the cross sections for cellulose particles with $a/b = 10$ (see Figs. 8 and 9) is ~50, and the temperature ratio is $36.0/59.2 = 0.61$, which gives approximately a factor of 30 larger dust mass if the particles are assumed to be spheres rather than spheroids. In other (not so extreme) cases, the dust-mass overestimate is much smaller. For example, for prolate amorphous carbon particles, $M_d^{\text{sphere}}/M_d^{\text{spheroid}} \approx 1.2$, 2.3, and 6.4 for $a/b = 2$, 4, and 10, respectively.

The degree of alignment of interstellar and circumstellar dust particles for rotational (Davies–Greenstein) orientation depends on the dust-to-gas temperature ratio: the smaller is this ratio, the more effective is the alignment of nonspherical particles (Greenberg 1970; Voshchinnikov 1986). In this case, as follows from Tables 1 and 2 and from the discussion in subsection 4.4, the nonspherical particles have a minimum temperature when the magnetic field is perpendicular to the line of sight ($\Omega = 90°$), i.e., when the polarization of the forward transmitted radiation is at a maximum. However, this remark more likely refers to protostellar envelopes than to interstellar particles, where the dust grains are heated by isotropic radiation.

Yet another important astrophysical process is the formation of molecules on the grain surfaces. Since the

efficiency of this process strongly depends on the grain temperature, a lower temperature of nonspherical particles can significantly facilitate the formation of molecules on their surfaces [see Voshchinnikov *et al.* (1999) for a discussion].

Finally, it should be mentioned that the sublimation (along with nucleation) of spherical and nonspherical particles must take place at different distances from the star. If we consider the evaporation of ice cometary grains in the interplanetary medium, then, despite the weak shape effect for ice (see Fig. 6), the differences for spheres and spheroids prove to be noticeable enough. Ice spheres reach the sublimation temperature [$T_d(\text{sphere}) = T_{\text{subl}} = 100$ K] and begin to evaporate at a distance $R \approx 20$ AU from the Sun. For prolate and oblate spheroids ($a/b = 10$, 3D orientation), this takes place closer to the Sun: at $R \approx 18$ and 16 AU, respectively.

6. CONCLUSION

Nonspherical interstellar and circumstellar dust grains must be slightly colder than spheres of the same volume composed of the same material. An analysis of the shape effects for spheroidal particles shows that the temperature differences do not exceed 10% for a spheroid aspect ratio $a/b \approx 2$. If $a/b \geq 4$, then the temperature differences reach 30–40%. Only iron spheroids can be slightly hotter than spheres. All shape effects are mainly associated with different emissivities of spherical and nonspherical particles at low temperatures. Grain porosity causes a reduction in the shape effects, whereas polarization of the incident radiation can either reduce or enhance them.

The calculated fluxes at $\lambda \gtrsim 100\ \mu m$ turn out to be higher if the grains are assumed to be nonspherical, resulting in an overestimation of the dust mass inferred from millimeter observations.

Finkbeiner and Schlegel (1999) point out that the Galactic-dust thermal emission at long wavelengths gives a major contribution to the observed background infrared radiation and must be subtracted in the search for fluctuations of the cosmic microwave background radiation in its Wien wing. In this case, very small (in magnitude) effects compared to which the effect of grain shape is significant and must be taken into account in modeling are sought.

ACKNOWLEDGMENTS

REFERENCES

1. S. Bagnulo, J. G. Doyle, and I. P. Griffin, Astron. Astrophys. **301**, 501 (1995).
2. Y. Baron, M. de Muizon, R. Papoular, and B. Pégourié, Astron. Astrophys. **186**, 271 (1987).
3. C. F. Bohren and D. R. Huffman, *Absorption and Scattering of Light by Small Particles* (Wiley, New York, 1983; Mir, Moscow, 1986).
4. B. J. Cadwell, H. Wang, E. D. Feigelson, and M. Frenklach, Astrophys. J. **429**, 285 (1994).
5. A. Z. Dolginov, Yu. N. Gnedin, and N. A. Silant'ev, *Propagation and Polarization of Radiation in Cosmic Medium* (Nauka, Moscow, 1979).
6. V. A. Dombrovskiĭ, Dokl. Akad. Nauk Armyan. SSR **10**, 199 (1949).
7. B. T. Draine, in *Physical Processes in Red Giants,* Ed. by I. Iben and A. Renzini (Reidel, Dordrecht, 1981), p. 317.
8. H. M. Dyck and M. C. Jennings, Astron. J. **76**, 431 (1971).
9. Yu. A. Fadeyev, in *Circumstellar Matter: IAU Symp. No. 122*, Ed. by I. Appenzeller and C. Jordan (Reidel, Dordrecht, 1987), p. 515.
10. D. P. Finkbeiner and D. J. Schlegel, astro-ph/9907307.
11. A. J. Fleischer, A. Gauger, and E. Sedlmayr, Astron. Astrophys. **266**, 321 (1992).
12. M. E. Fogel and C. M. Leung, Astrophys. J. **501**, 175 (1998).
13. H.-P. Gail and E. Sedlmayr, Astron. Astrophys. **132**, 163 (1984).
14. H.-P. Gail and E. Sedlmayr, Astron. Astrophys. **148**, 183 (1985).
15. J. H. Goebel and H. Moseley, Astrophys. J. Lett. **290**, L35 (1985).
16. J. M. Greenberg, *Interstellar Grains* in *Stars and Stellar Systems*, vol. VII, Ed. by B.M. Middlehurst and L.H. Aller (Univ. Chicago, 1968; Mir, Moscow, 1970).
17. J. M. Greenberg, Astron. Astrophys. **12**, 240 (1971).
18. J. M. Greenberg and G. A. Shah, Astron. Astrophys. **12**, 250 (1971).
19. Th. Henning, V. B. Il'in, N. A. Krivova, *et al.*, Astron. Astrophys., Suppl. Ser. **136**, 405 (1999).
20. R. H. Hildebrand, Quart. J. R. A. S. **24**, 267 (1983).
21. W. A. Hiltner, Science **109**, 165 (1949).
22. T. S. Hall, Science **109**, 166 (1949).
23. V. B. Il'in and N. V. Voshchinnikov, Astron. Astrophys., Suppl. Ser. **128**, 187 (1998).
24. C. Jäger, H. Mutschke, and Th. Henning, Astron. Astrophys. **332**, 291 (1998).
25. C. Jäger, H. Mutshcke, B. Begemann, *et al.*, Astron. Astrophys. **292**, 641 (1994).
26. M. Jura, Astrophys. J. **434**, 713 (1994).
27. M. Jura, Astrophys. J. **472**, 806 (1996).
28. J.-P. J. Lafon and N. Berruyer, Astron. Astrophys. Rev. **2**, 249 (1991).
29. P. L. Lamy and J.-M. Perrin, Astron. Astrophys. **327**, 1147 (1997).
30. I. Little-Marenin, Astrophys. J. Lett. **307**, L15 (1986).
31. S. Lorenz-Martins and J. Lefevre, Astron. Astrophys. **291**, 831 (1994).
32. J. S. Mathis, P. G. Mezger, and N. Panagia, Astron. Astrophys. **128**, 212 (1983).
33. T. Onaka, Astrophys. J. **533**, 298 (2000).
34. V. Ossenkopf and Th. Henning, Astron. Astrophys. **291**, 943 (1994).
35. V. Ossenkopf, Th. Henning, and J. S. Mathis, Astron. Astrophys. **261**, 567 (1992).
36. B. Pégourié, Astrophys. Space Sci. **136**, 133 (1987).
37. S. J. Shawl, Astron. J. **80**, 602 (1975).
38. R. Siebenmorgen, E. Krügel, and R. Chini, Astron. Astrophys. **351**, 495 (1999).
39. L. Spitzer, Jr., *Physical Processes in Interstellar Medium* (Wiley, New York, 1978; Mir, Moscow, 1981).
40. H. C. van de Hulst, Rech. Astron. Obs. Utrecht **11**, Part 2 (1949).
41. N. V. Voshchinnikov, Itogi Nauki Tekh., Ser. Issled. Kosm. Prostranstva **25**, 98 (1986).
42. N. V. Voshchinnikov and V. G. Farafonov, Astrophys. Space Sci. **204**, 19 (1993).
43. N. V. Voshchinnikov, D. A. Semenov, and Th. Henning, Astron. Astrophys. **349**, L25 (1999).
44. N. V. Voshchinnikov, V. B. Il'in, Th. Henning, *et al.*, J. Quant. Spectrosc. Radiat. Transf. **65**, 877 (2000).
45. L. B. F. M. Waters, F. J. Molster, and C. Waelkens, in *Solid Interstellar Matter: the ISO Revolution*, Ed. by L. d'Hendecourt *et al.* (Springer-Verlag, Berlin, 1999), p. 219.
46. D. C. B. Whittet, in *Dust in the Galactic Environments* (Institute of Physics Publ., New York, 1992).
47. A. P. Whitworth, H. M. J. Boffin, and N. Francis, Mon. Not. R. Astron. Soc. **299**, 554 (1998).
48. P. Woitke, C. Dominik, and E. Sedlmayr, Astron. Astrophys. **274**, 451 (1993).

Translated by V. Astakhov